REPUBLIQUE ALGERIENNE DEMOCRATIQUE ET POPULAIRE

MINISTÈRE DE L'ENSEIGNEMENT SUPÉRIEUR ET DE LA RECHERCHE SCIENTIFIQUE

UNIVERSITE KASDI MERBAH OUARGLA
Faculté des Sciences Appliquées
Département de Génie Mécanique

THÈSE

Soumis pour l'obtention du diplôme Doctorat en Génie Mécanique

Spécialité : Fabrication Mécanique et Productique

Par

AMIRA Mohammed Toufik

Intitulé

Contribution à l'étude de l'intégrité de surface de l'acier au carbone AISI 1060 après fraisage

Soutenue publiquement le 14 Mars 2024 devant le jury composé de :

BELAKROUM Rassim	Prof	Université Kasdi Merbah - Ouargla	Président
BELLOUFI Abderrahim	Prof	Université Kasdi Merbah - Ouargla	Rapporteur
ABDELKRIM Mourad	MCA	Université Kasdi Merbah - Ouargla	Co-Rapporteur
BENNOUNA Mohammed Salah	MCA	Université Kasdi Merbah - Ouargla	Examinateur
AMEUR Toufik	MCA	Université Kasdi Merbah - Ouargla	Examinateur
BOUREBBOU Amor	MCA	Université Frères Mentouri - Constantine 1	Examinateur
CHIRIȚĂ Bogdan Alexandru	Prof	Université Vasile Alecsandri - Bacău, Roumanie	Invité

Année Universitaires : 2023/2024

PEOPLE'S DEMOCRATIC REPUBLIC OF ALGERIA

MINISTRY OF HIGHER EDUCATION AND SCIENTIFIC RESEARCH

UNIVERSITY KASDI MERBAH OF OUARGLA
Faculty of Applied Sciences
Department of Mechanical Engineering

THESIS

Submitted for obtaining the Doctorate degree in Mechanical Engineering

Specialty: Mechanical and Productive Manufacturing

By

AMIRA Mohammed Toufik

Entitled

Contribution To the Study of Surface Integrity in AISI 1060 Carbon Steel after Milling

Publicly defended on 14th March 2024 in front of the jury composed of:

BELAKROUM Rassim	Prof	University Kasdi Merbah - Ouargla	President
BELLOUFI Abderrahim	Prof	University Kasdi Merbah - Ouargla	Supervisor
ABDELKRIM Mourad	MCA	University Kasdi Merbah - Ouargla	Co-Supervisor
BENNOUNA Mohammed Salah	MCA	University Kasdi Merbah - Ouargla	Examiner
AMEUR Toufik	MCA	University Kasdi Merbah - Ouargla	Examiner
BOUREBBOU Amor	MCA	University Frères Mentouri - Constantine 1	Examiner
CHIRIȚĂ Bogdan Alexandru	Prof	University Vasile Alecsandri - Bacău, Romania	Guest

Academic Year: 2023/2024

Acknowledgments

Above all, I foremost thank Allah the Almighty for giving me a mother so strong who has provided me with infinite love and support since the very first day of my life. Without you, my mother "*Noura Benseddik*", it would have been impossible for me to reach this point.

And I thank Allah once again for the will, health, and patience He has bestowed upon me throughout these long years, for enlightening me and opening the paths of knowledge, and for granting me the courage throughout this journey.

I sincerely enjoyed the entire duration of this modest work. I was fortunate to have quality scientific supervision. I thus extend my warmest thanks to my supervisor **Prof. Abderrahim Belloufi**, first for the inspiration he gave me to continue the doctoral studies. I also want to take a moment to express my sincere gratitude as the completion of this thesis would not have been possible without your valuable guidance and wise advice. Your expertise in the field, your passion for research, and your commitment to the advancement of knowledge have been a constant source of inspiration for me. Your attentive supervision and encouragement have played a decisive role in my academic success.

I also offer my special thanks to my co-supervisor **Pr. Mourad Abdelkrim** for assisting me during my doctoral cycle, for his valuable advice and encouragement, and especially for his assistance with the experimental work.

I would like to express my deepest gratitude to **Pr. Rassim Belakroum** for his kind interest in this work and for the honor of presiding over the jury.

I would like to dedicate this modest work to:

To my mother

To my sister

To my brothers

To my family

To my relatives

To all my teachers

To all my loved ones and friends

To everyone who ever gave me help in my life

In memory of my father and all my dear deceased ones, Allah bless them.

Mohammed Toufik Amira

Table of Contents

Chapter I

Bibliographic Synthesis

Chapter II

Experimental Procedure

Chapter III

Modelization and Optimization

Chapter IV
Simulation of Surface Defects after Milling

List of Figures

Chapter III

Modelization and Optimization

Chapter IV

Simulation of Surface Defects after Milling

List of Tables

Nomenclature

Symbol	Unit	Designation
A	%	Accuracy
a_e	mm	Width of cut
a_p	mm	Depth of cut
$a_{p_{max}}$	mm	The maximum depth of cut
$a_{p_{min}}$	mm	The minimum depth of cut
C	-	Machining index
C_c	$Euro$	The total cost per unit product
C_F	-	Constant for the cutting force equation
C_h	$Euro$	Cost of part handling time
C_m	$Euro$	Cost of machining time
C_{th}	$Euro$	Cost of tool change time
C_{tc}	$Euro$	Tooling cost
C_0	$Euro/min$	The cost rate
C_t	$Euro$	The cost per cutting edge
D	mm	The cutter diameter
e_i	%	Error rate
f	mm/rev	Feed per revolution
f_z	$mm/tooth$	Feed per tooth
$f_{z_{max}}$	$mm/tooth$	The maximum feed per tooth
$f_{z_{min}}$	$mm/tooth$	The minimum feed per tooth
F_u	N	The maximum cutting force
F_c	N	Cutting force
H	H_v	Microhardness

H_s	H_v	Specified value of microhardness
k_F	-	Constant for the cutting force equation
L	mm	Workpiece length
S	RPM	Spindle speed
n	-	Tool life index
n_e	-	Number of cutting edges per insert
n_p	-	Number of pieces cut in one tool life
n_s	-	Constant for the cutting force equation
MMR	mm^3/min	Material removal rate
P_c	W	Cutting power
p_F	-	Exponent for the cutting force equation
P_m	W	Net power
P_t	$Euro$	Price of the insert
P_u	W	The nominal power of the machine
Q_c	$°C$	Cutting temperature
q_F	-	Exponent for the cutting force equation
R_a	μm	Surface roughness
R_{as}	μm	Specified value of surface roughness
T	min	Tool life
T_c	min	Production cycle time per piece
t_F	-	Exponent for the cutting force equation
T_h	min	Part handling time
T_m	min	Machining time
T_t	min	Tool change time
T_{max}	min	The maximum tool life
T_{min}	min	The minimum tool life
u	-	Step between the tooth
V_c	m/min	Cutting speed

$V_{c_{max}}$	*m/min*	The minimum cutting speed
$V_{c_{min}}$	*m/min*	The minimum cutting speed
V_{exp}	-	The experimental value
V_f	*mm/min*	Feed rate
V_{pred}	-	The predicted value.
w_F	-	Exponent for the cutting force equation
x_F	-	Exponent for the cutting force equation
y_F	-	Exponent for the cutting force equation
Z	-	The number of teeth
η	-	Machine efficiency

General Introduction

In the realm of mechanical manufacturing and materials engineering, the interplay between milling processes, surface integrity, and fatigue life of materials constitutes a critical area of study, given its profound implications for the performance and longevity of engineered components. Milling, a fundamental machining process, involves the removal of material from a workpiece to shape it into a desired form through the concerted action of a rotating tool and its cutting edges. This process is not only pivotal for achieving the desired geometry but also influences the surface characteristics of the material, which are collectively referred to as surface integrity. Surface integrity encompasses a range of surface and subsurface features including, but not limited to, surface roughness, microstructural alterations, microhardness, residual stresses, and the presence of surface defects such as micro-cracks and inclusions.

The concept of surface integrity is intrinsically linked to the material's fatigue life, which denotes the duration or number of cycles a material can withstand under repeated loading before failure occurs. The fatigue life of a material is significantly impacted by its surface condition; for instance, enhanced surface roughness or the induction of tensile residual stresses during milling can serve as nucleation sites for cracks, thereby reducing the fatigue life. Conversely, certain milling parameters and techniques can be optimized to impart compressive residual stresses and refine the microstructure at the surface, potentially enhancing the material's resistance to fatigue.

The intricate relationship between milling parameters (such as cutting speed, feed rate, depth of cut), the resulting surface integrity, and the subsequent impact on fatigue life necessitates a comprehensive understanding to optimize manufacturing processes for enhanced component performance and durability. This triad of factors forms the cornerstone of ongoing research endeavors aimed at elucidating the mechanisms at play and leveraging this knowledge to advance the field of material science and engineering.

the optimization of milling operations must also consider the imperatives of cost and time efficiency. The cost associated with milling encompasses tool wear, energy consumption, material utilization, and labor, making it essential to adopt strategies that minimize these expenses without compromising quality. Time efficiency, on the other hand, is pivotal for maintaining competitive lead times and maximizing throughput in manufacturing environments. Advanced techniques such

Genetic Algorithms (GA), Artificial Neural Network (ANN) and Particle Swarm Optimization (PSO) emerge as key enablers in this regard, offering pathways to reduce machining time while ensuring superior surface integrity and component longevity.

This multifactorial optimization challenge underscores the need for an integrated approach in manufacturing research and practice. By holistically addressing the dynamics between milling processes, surface integrity, cost and time efficiency, and fatigue life, manufacturing engineers can devise strategies that not only push the boundaries of material capabilities and component performance but also align with economic and sustainability goals, marking a significant stride in the advancement of manufacturing science.

Based on literature review, numerous studies have focused on using empirical models documented in the handbooks to optimize the machining responses in milling process. However, to author best knowledge, there is no research published optimizes the cost and production time in milling process by using GA while considering the R_a and H based-RSM models as constraints in defining the optimization problem.

This work has three objectives: first, to empirically investigate the influence of cutting parameters (V_c, f_z and a_p) on key milling responses-namely, cutting temperature (Q_c), surface roughness (R_a), and microhardness (H). Second, it aims to introduce a novel optimization strategy by utilizing Genetic Algorithms (GA) to concurrently minimize production time and cost in the milling process, a departure from previous studies primarily focused on the generalized empirical models commonly documented in the handbooks.

What sets this research apart is the pioneering integration of Genetic Algorithms with specific Response Surface Methodology (RSM) models, specifically R_a and H based models, as defining constraints in the optimization problem. This innovative approach offers a more nuanced and precise means of optimizing the milling process by considering both surface quality measures (R_a, H) alongside conventional machining constraints, filling a significant gap in the existing literature.

Finally, the third objective is to examine the influence of surface integrity on fatigue life.

This thesis is organized as follows:

- The first chapter gathers the elements of bibliography necessary for this study.
- The second chapter describes the experimental procedures for the milling experiment that was done, including the measurement procedures for cutting

temperature, surface roughness and microhardness. Finally, the experimental results will be presented.

- The third chapter focuses on the development of models for the cutting temperature, surface roughness and microhardness through Response Surface Methodology (RSM) and the application of multi-objective optimization using the Genetic Algorithms (GA) to minimize both production time and cost per unit.

- The fourth chapter focuses on conducting a comparison using ANSYS to evaluate the performance of a presumed milled workpiece both without and with a crack present on its surface. This analysis aims to elucidate the influence of surface integrity on the fatigue life of mechanical components.

CHAPTER I

Bibliographic Synthesis

I.1. Introduction

In this chapter, a comprehensive elucidation of the milling process will be provided, including a succinct definition followed by a delineation of the principal types of milling operations. Furthermore, a description of the cutting parameters will be presented. The chapter will proceed to examine the implications of machining with and without lubrication, elucidating the various damage mechanisms of cutting tools as well as discussing the cutting temperature in the material removal processes. Considerable attention will be devoted to the surface integrity of a machined part, emphasizing the paramount importance of two critical aspects: surface roughness and microhardness especially in the literature review.

I.2. Milling

I.2.1. Definition

Milling is one of the most commonly used manufacturing processes in the industry. It involves the machining of different parts with different shapes and sizes by gradually removing material in the form of chips using a cutting tool. Unlike turning, the rotational movement is given to the cutting tool, while the translational movement can be given to either the workpiece or the cutting tool. The axis of rotation of the cutting tool in the milling operation is perpendicular to the feed direction. This orientation between the tool axis and the feed direction is one of the characteristics that distinguishes milling from drilling where the feed of the cutting tool is in a direction parallel to its axis of rotation. The cutting tool used in the milling operation, known as a milling cutter, is composed of multiple teeth (multiple cutting edges) and has a circular shape in various sizes, tailored to specific machining needs. In rare cases, a single-edged tool called a fly cutter is used.

Milling can be performed on various types of machine tools called milling machines, which can be manual, semi-automatic, or fully automated. The milling process allows the production of complex parts with high dimensional accuracy and a high-quality of surface finish.

I.2.2. Types of milling operations

There are two types of milling depending on the type of machine, the type of tool, the desired surface finish, the position of the surfaces on the machine, the dimensions of the surfaces to be milled, and the geometries of the cutters.

a) Face milling

In the face milling, the position of the axis of rotation of the cutter is perpendicular to the milled surface.
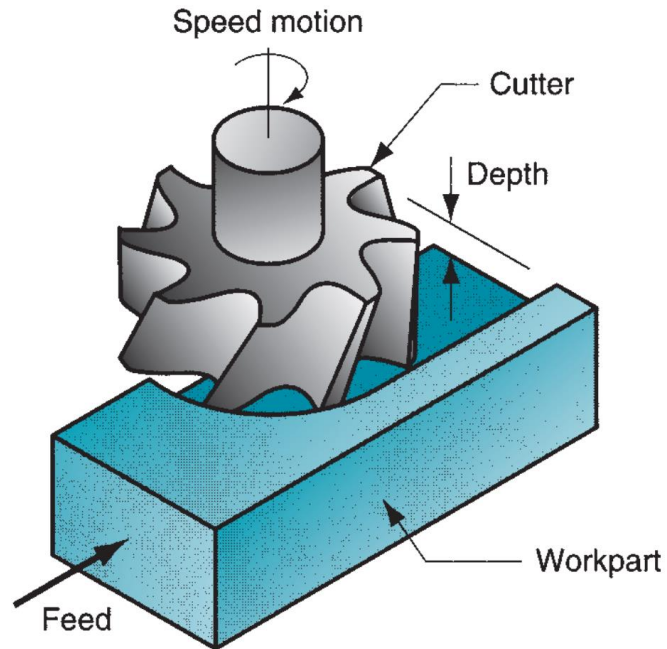
Figure I.1 *Face milling [1].*

b) Peripheral milling

In the peripheral milling (also called plain milling or slab milling) the position of the axis of rotation of the cutter is parallel to the milled surface.
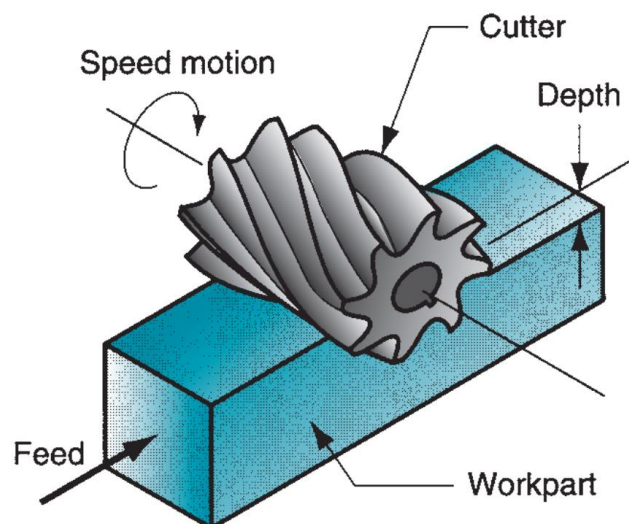
Figure I.2 *Peripheral milling [1].*

I.2.3. Up milling versus down milling

One of the subtle aspects of milling concerns the direction of rotation of the cutter with respect to the movement of the workpiece. Surfaces can be generated by two distinctly different methods, up milling or down milling. Each has distinct characteristics and applications based on the relative motion of the workpiece and the cutting tool [2].

a) Up milling

In up milling also called conventional milling, the cutter rotates against the direction of the feed of the workpiece. As the cutting occurs, the thickness of the chip gradually increases from zero at the point of entry to a maximum at the point of exit.
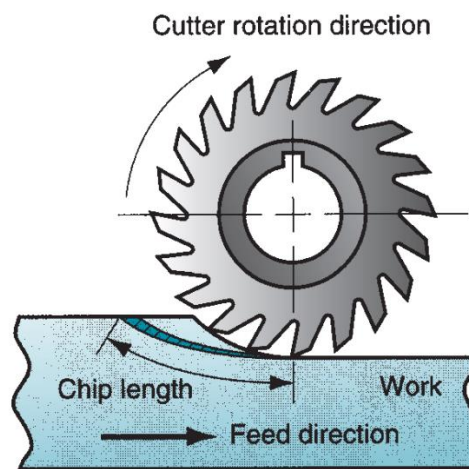
Figure I.3 *Up (conventional) milling [1].*

b) Down milling

Conversely, in down milling also called climb milling, the cutter rotates in the same direction as the feed of the workpiece. The chip thickness starts at maximum and decreases to zero by the end of the cut.
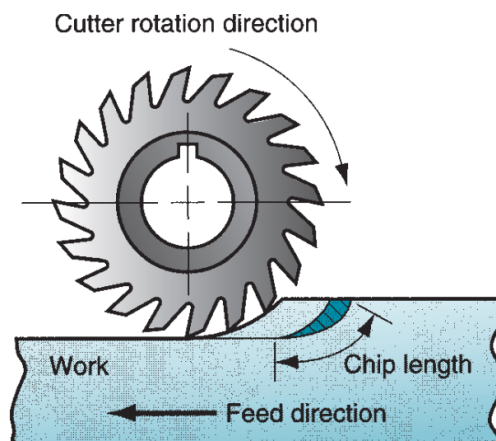
Figure I.4 *Down (climb) milling [1].*

I.3. Cutting parameters

To adjust the parameters of the milling operation, it is first necessary to establish some definitions applied to the dynamic characteristics of the milling tool.

I.3.1. Spindle speed

Spindle speed (S in *rev/min*) is the number of revolutions that the milling tool installed on the machine tool spindle makes per minute.
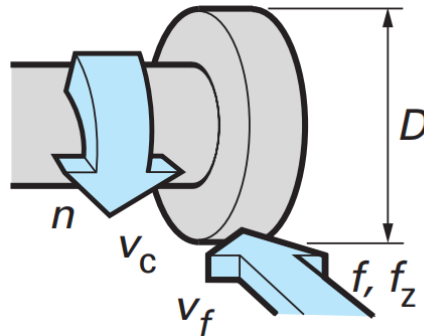
Figure I.5 *Spindle speed* [3].

$$S = \frac{V_c \times 1000}{\pi D} \quad\quad\quad (I.1)$$

D : Milling tool diameter (*mm*).

S : Spindle speed (*rev/min*).

V_c : Cutting speed (*m/min*).

I.3.2. Cutting speed

The cutting speed (V_c in *m/min*) indicates the speed at which the cutting edge works in the surface of the workpiece. Spindle speed, tool diameter and cutting speed are naturally related by the following formulas:

$$V_c = \frac{\pi D S}{1000} \quad\quad\quad (I.2)$$
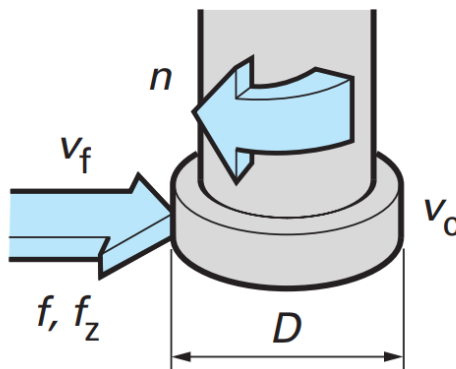
Figure I.6 *Cutting speed* [3].

I.3.3. Feed rate

The feed rate or feed per minute V_f (*mm/min*) is the movement of the tool towards the workpiece, expressed in units of distance per unit of time, it is also possible to use the feed per tooth which indicates the linear distance traveled by the tool while a certain tooth is engaged. The feed per tooth also represents the distance covered between the penetration of two successive teeth into the workpiece. It can therefore be expressed as a function of the number of teeth of the tool (*Z*) and the feed per minute, or in the form of feed per revolution as shown in the following formulas:
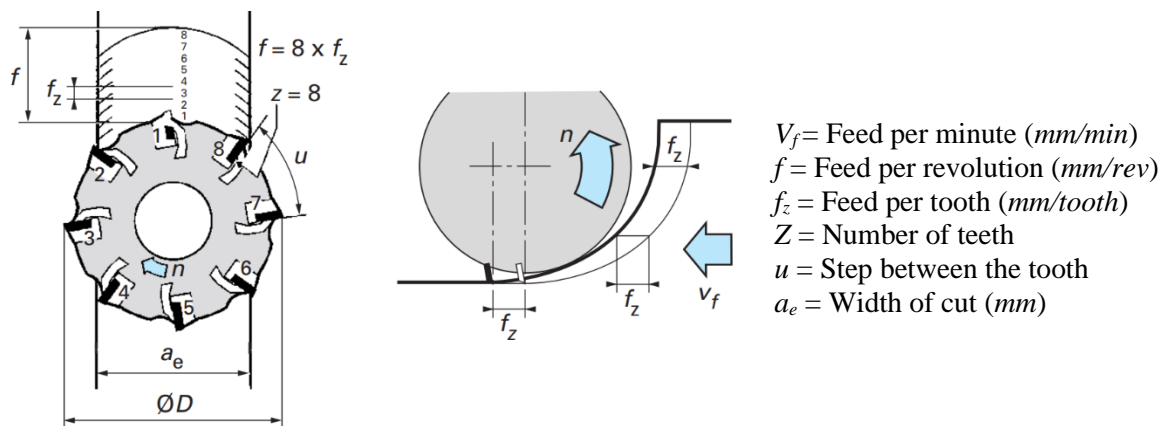
Figure I.7 *The feed rate and feed per tooth* [3].

$$f_z = \frac{V_f}{S \times Z}$$

(I.3)

f_z : Feed per tooth (*mm/tooth*)

V_f : Feed rate (*mm/min*)

Z : Number of teeth

I.3.4. Depth of cut

The depth of cut, which can be axial (a_p) for face milling or radial (a_e) called also width of cut for shoulder milling, corresponds to the thickness of material removed by the tool. This is the distance at which the tool is set below the initial surface of the workpiece.

a_e = Width of cut (*mm*)
a_p = Depth of cut (*mm*)
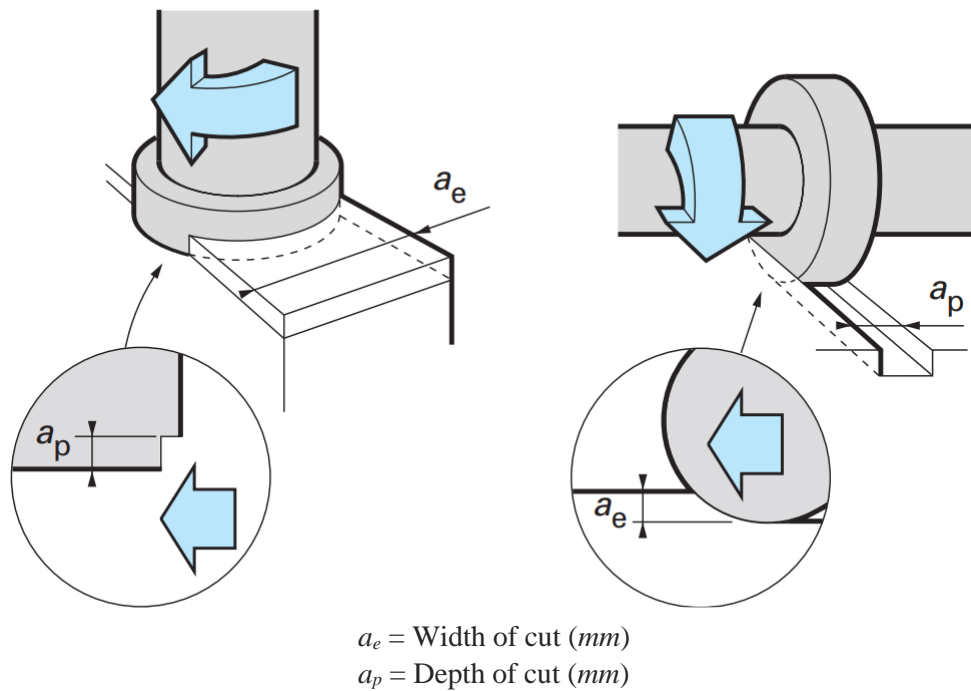
Figure I.8 *Width and depth of cut* [3].

I.4. Machining with and without lubrication

Machining, a process where material is removed from a workpiece to achieve desired dimensions and surface finish, can be done with or without lubrication. Due to the tribology of the tool-chip and tool-workpiece interfaces where the contact stresses and conditions are significant and very severe and the generated temperatures due to the friction are very high in the machining [4], The choice depends on the workpiece material, machining process, tool material, desired surface finish, and other factors.

I.4.1. Machining with lubrication (Use of Cutting Fluids or Coolants)

When machining at high speeds, heat is generated due to the friction between the cutting tool and the workpiece, leading to energy dissipation in the form of heat. If either the workpiece or the cutting tool becomes excessively hot, it can result in thermal deformation, potentially impacting the machining process or causing damage to the equipment. To mitigate this issue, lubrication plays a crucial role by reducing friction and consequently lowering the temperature, helping to prevent overheating of the components.

a) Functions and advantages of lubrication in machining

- Friction Reduction: Lubrication creates a thin film between the cutting tool and workpiece, reducing friction and minimizing wear on the tool.

- Heat Dissipation: As the cutting tool engages with the workpiece, it generates heat due to friction. Lubricants help dissipate this heat, preventing the tool from overheating and the workpiece from thermal damage.

- Chip Evacuation: Lubricants aid in chip evacuation by lubricating the chip-tool interface, making it easier for chips to flow away from the cutting zone.

- Corrosion Prevention: Many cutting fluids contain additives that protect the workpiece and cutting tool from corrosion, especially in cases where the workpiece material is susceptible to oxidation.

- Extended Tool Life: Reduced friction and heat lead to less tool wear, resulting in longer tool life and reduced tool replacement costs.

- Improved Surface Finish: Lubrication can result in smoother and higher-quality surface finishes on machined parts.

- Enhanced Machining Speeds and Feeds: The use of cutting fluids can often enable higher cutting speeds and feeds, increasing productivity.

- Dimensional Accuracy: Lubrication helps maintain dimensional accuracy of machined parts by minimizing workpiece distortion due to heat.

- Prevention of Workpiece Welding: In some cases, especially with materials like aluminum, the workpiece material can weld onto the tool. Cutting fluids can help prevent this from occurring.

- Reduced Power Consumption: The frictional resistance is decreased with the application of cutting fluids, resulting in reduced power consumption.

b) Disadvantages of lubrication in machining:

- Cost: Continuous use of cutting fluids adds to operational costs.

- Maintenance: Machines using cutting fluids require regular maintenance to prevent contamination, fluid degradation, and bacterial growth.

- Environmental Concerns: Many cutting fluids, especially oil-based ones, pose environmental risks. They need proper disposal to prevent pollution.

- Safety Considerations: While lubrication offers many benefits, it's essential to handle cutting fluids safely. Some cutting fluids can pose health and environmental risks, so proper storage, handling, and disposal are critical to ensuring a safe machining environment.

I.4.2. Machining Without Lubrication (Dry Machining)

a) Advantages of Dry Machining:

- **Cost Savings:** No costs associated with purchasing, maintaining, or disposing of cutting fluids.

- **Environmental Benefits:** Dry machining avoids the environmental concerns associated with cutting fluid disposal.

- **Safety:** Reduced risk of fire, skin irritation, and respiratory issues.

- **Simpler Cleanup:** Without cutting fluids, the post-machining cleanup process can be more straightforward.

- **Suitable for Certain Materials:** Some materials, like cast iron, naturally provide a certain level of lubrication due to graphite content.

b) Disadvantages of Dry Machining:

- **Shorter Tool Life:** The absence of lubrication can lead to shorter tool life and more frequent tool changes this is due to increased friction and heat.

- **Poor Surface Finish:** In some cases, dry machining may result in a rougher surface finish on the workpiece.

- **Higher Power Consumption:** Increased friction can lead to higher power consumption.

- **Increased Heat:** Dry machining generates more heat, which can lead to tool wear and workpiece deformation.

The choice between machining with or without lubrication depends on various factors, including the material being machined, the machining process, the desired surface finish, tool life requirements, and cost considerations. Machining with proper lubrication is generally preferred for precision metalworking operations, while dry machining may be suitable for less demanding applications or when specific advantages, such as cost savings or environmental concerns, take precedence. It's essential to consider the specific requirements of each machining job and the characteristics of the materials involved when making this decision.

I.5. Damage mechanisms of cutting tools

Cutting tools are essential in various manufacturing and engineering processes, but they can fail due to various damage mechanisms. Understanding these mechanisms is crucial, especially in fields like mechanical engineering and materials science. Here are some common damage mechanisms for cutting tools:

a) Wear-Related Failure:

- **Abrasive Wear:** Occurs due to hard particles or asperities on the workpiece material that mechanically remove material from the tool.

- **Adhesive Wear:** Occurs when material from the workpiece or environment adheres to the tool, leading to material transfer or loss.

- **Diffusive Wear:** Happens at high temperatures when atoms from the tool material diffuse into the workpiece or vice versa.

- **Oxidative Wear:** Involves the formation of oxides on the tool surface, leading to material loss.

b) Thermal Failure:

- **Thermal Cracking:** Due to the cyclic heating and cooling during the machining process, thermal stresses can cause cracks in the tool.

- **Softening:** Excessive heat can lead to the softening of the tool material, reducing its hardness and wear resistance.

c) Mechanical Failure:

- **Chipping and Fracturing**: Can occur due to excessive loads, impact, or vibrations, leading to the removal of small chips or cracks in the tool, which can propagate and cause failure.

- **Plastic Deformation**: Under high stress or temperature, the tool material may undergo plastic deformation, leading to a loss of cutting-edge sharpness and accuracy.

d) Chemical Degradation:

- Involves chemical reactions between the tool material and the workpiece or environment, leading to corrosion or other chemical wear mechanisms.

e) Built-Up Edge (BUE) Formation:

- This happens when material from the workpiece adheres to the cutting edge of the tool. It can alter the geometry of the cutting edge, impacting the cutting performance and surface finish.

f) Catastrophic Failure:

- Sudden failure of the tool due to excessive stress, overload, or a large flaw in the tool material.

g) Tool Life and Failure Criteria:

- Tools are often considered to have failed when they reach a certain wear limit, or when the surface finish or dimensional accuracy of the workpiece is no longer acceptable.

I.6. Cutting temperature

In the context of machining processes, cutting temperature is a crucial factor that significantly affects both the tool's performance and the quality of the workpiece. Understanding and managing cutting temperatures is essential for optimizing machining operations and ensuring the longevity of the cutting tools. Here are some key aspects related to cutting temperature in machining:

- **Sources of Heat**: Cutting temperature is primarily generated due to two factors: plastic deformation of the workpiece material and friction between the cutting tool and the workpiece. As the tool penetrates the material, it deforms the workpiece at the cutting edge, generating heat.

- **Impact on Tool Wear**: High cutting temperatures can accelerate tool wear, reducing the tool's lifespan [5]. Tool materials like high-speed steel, carbide, ceramics, and polycrystalline diamond have different heat tolerances, influencing their performance and wear rate.

- **Effects on Material Properties**: Excessive heat can affect the properties of the workpiece material, such as hardness and microstructure. It can also lead to thermal expansion, affecting dimensional accuracy.

- **Cooling and Lubrication**: Coolants and lubricants are used to dissipate heat, reduce friction, and remove chips from the cutting zone. The choice of coolant and its application method can significantly influence the cutting temperature.

- **Cutting Parameters**: Variables such as cutting speed, feed rate, depth of cut, and tool geometry can impact the cutting temperature. Higher cutting speeds, for instance, typically lead to higher temperatures.

- **Measurement Techniques**: Cutting temperatures can be measured using direct methods like embedded thermocouples, infrared sensors or camera, and indirect methods like tool-work thermocouple technique.

- **Thermal Deformation**: In precision machining, even small changes in temperature can lead to thermal expansion or contraction, affecting the accuracy of the machined part.
- **Optimization**: Understanding the relationship between cutting parameters and temperature allows for optimization of the machining process, balancing productivity, tool life, and workpiece quality.
- **Advanced Techniques**: Modern machining processes might employ advanced strategies like cryogenic machining or minimum quantity lubrication (MQL) to manage cutting temperatures effectively.

I.7. Surface integrity

Surface integrity refers to the condition of the surface of a material after it has undergone a manufacturing process, particularly machining or other surface-modifying operations. It's a critical concept in mechanical engineering and material science because the surface condition of a component can significantly influence its performance, durability, and overall functionality. Here are some key aspects of surface integrity:

- **Surface Roughness:** This describes the texture of the surface, including the presence of peaks and valleys. Surface roughness is often quantified using parameters like Ra (average roughness) and Rz (maximum height of the roughness profile).
- **Surface Topography:** Beyond roughness, this involves the 3D geometric characteristics of the surface, including lay, waviness, and other features.
- **Microstructural Alterations:** Machining and surface treatments can alter the microstructure of the material near the surface. This includes changes in grain size, phase transformations, and the creation of residual stresses.
- **Residual Stresses:** These are stresses retained in the material after the manufacturing process is complete. Compressive residual stresses are often desirable as they can improve fatigue resistance [6], while tensile residual stresses can lead to cracking and early failure.
- **Surface Defects:** Any cracks, voids, or inclusions that can act as sites for fatigue crack initiation or corrosion.

- **Chemical and Phase Changes:** Some manufacturing processes can alter the chemical composition or phase of the material at the surface, which can affect properties like corrosion resistance, wear resistance, and hardness.

- **Hardness and Wear Resistance:** The surface hardness, which can be different from the bulk material's hardness, is crucial in determining the wear resistance of the component (more details are presented in I.8).

I.8. Hardness and microhardness

I.8.1. Hardness

Hardness is a fundamental property of materials, particularly relevant in fields like mechanical engineering, materials science, and metallurgy. It's a measure of a material's resistance to deformation (the resistance that a surface of the sample opposes to the penetration of a punch), particularly permanent deformation, indentation, or scratching [1]. hardness helps in understanding and predicting the behavior of materials under various mechanical stresses. It's particularly important in the context of material selection, design considerations, and failure analysis in engineering applications.

Types of Hardness Tests [1]:

- **Brinell Hardness Test**: Uses a hard steel or carbide ball as an indenter with a fixed load. The diameter of the indentation is measured to calculate hardness.

- **Vickers Hardness Test**: Involves a diamond pyramid-shaped indenter. Suitable for a wide range of materials, the test measures the diagonal of the square indentation.

- **Rockwell Hardness Test**: This is a fast and simple method using either a diamond cone or a hard steel ball indenter. The depth of indentation determines the hardness.

- **Knoop Hardness Test**: Similar to Vickers but uses an elongated diamond indenter. Ideal for brittle materials or thin sections.

- **Shore (Durometer) Hardness Test**: Commonly used for polymers and elastomers. It measures the depth of an indentation by a standard-sized indenter under a standard load.

- **Scleroscope:** It works on the principle of measuring the rebound of a diamond-tipped hammer dropped from a fixed height onto the material being tested. The hardness of the material is indicated by the height of the rebound of the hammer.

I.8.2. Microhardness

Micro-hardness refers to the hardness of a material as measured on a microscopic scale. It's a key property in materials science, especially for understanding the behavior of metals, ceramics, and some polymers under various conditions. Here are some important aspects of micro-hardness:

a) Definition and Measurement:

- Micro-hardness is measured using a micro-indentation test, where a small indenter, typically made of diamond, is pressed into the surface of a material under a specific load. The size of the indentation left is then measured, and the hardness is calculated based on the indentation size and the applied force.

b) Scales and Indenters:

- Common scales for micro-hardness testing include the Vickers (using a diamond pyramid indenter) and Knoop (using a diamond rhombic-based pyramid indenter) hardness tests. These methods are preferred for small or thin specimens and for materials with a fine microstructure.

c) Applications:

- Micro-hardness testing is crucial in materials engineering for evaluating the mechanical properties of thin films, surface coatings, heat-treated materials, and microstructures within a composite material.
- It's also used in failure analysis to understand wear, deformation, and fracture processes at a micro-scale.

d) Factors Affecting Micro-hardness:

- Material Composition: The elemental makeup and microstructure of a material greatly influence its hardness.
- Heat Treatment: Processes like annealing, quenching, and tempering can alter the microstructure and hence the hardness of a material.
- Manufacturing Processes: Techniques like forging, casting, and welding can affect the hardness due to changes in microstructure.

e) Micro-hardness in Research and Industry:

- Micro-hardness testing is widely used in research for developing new materials and understanding the behavior of existing ones under different conditions.

- In industry, it's used for quality control and to ensure that materials meet required specifications, particularly in critical applications like aerospace, automotive, and medical devices.

Understanding micro-hardness can provide valuable insights into the material properties that are critical for the performance and durability of a wide range of engineering materials, including those used in concrete structures.

I.9. Literature review "Milling"

In the last few years, many researchers have been done to investigate the milling process, and here is a bibliographic search for some scientific works that have studied this process:

Vikas Marakini et al. [7] did an experimental investigations to evaluate the performance of face milling operations on the surface integrity of AZ91 magnesium alloy using uncoated carbide inserts and PVD coated carbide inserts, from the microstructural analysis they found that PVD coated insert conditions produce surface with no defects, when compared to the crack observed in the surface when they used uncoated carbide inserts. And also, due to the significant improvement in hardness and roughness when they used PVD coated carbide inserts they recommend the use of that type of inserts in face milling operation.

Emre Altas et al. [8] investigated the surface integrity of nickel-titanium (NiTi) shape memory alloys (SMAs) after face milling under dry and MQL conditions at different cutting parameters using different type of cutting tools (cryogenic heat treated/untreated PVD and CVD coated/uncoated cemented carbide) , they recommended the use of carbide cutting tools treated under deep cryogenic heat and the milling process should carried out under the conditions of EG + %5BX cutting fluid.

Wei Zhao et al.[9] investigated the use of liquid nitrogen (LN2) as a cooling mode in cryogenic milling of Ti-6Al-4V alloy, they found that the cryogenic milling using liquid nitrogen (LN2) significantly improve the surface integrity of the Ti-6Al-4V alloy compared with the dry milling.

Farhad Molaiekiya et al.[10] investigated the surface integrity in high speed dry milling of Inconel 718 using SiAlON ceramic tools and they compared the results with the results of surfaces machined with conventional coated carbide tool, they found that there is imperfections within a thin sublayer of the workpiece when they used the ceramic tools compared to the carbide tool, so they suggest the use of ceramic tools for roughing processes provided further finishing operations performed to remove the damaged layer.

Guangming Zheng et al. [11] studied the surface integrity of AISI 4340 steel in high-speed dry milling using TiCN-NbC composite coated tool. they reported that fz is the most influential factor in surface roughness also the tool wear is considered, and the minimum variation of surface roughness Ra with tool wear is obtained at $Vc = 350$ *m/min*. They reported also that stress state and work hardening degree generated by the milling process will improve the corrosion resistance, wear resistance and fatigue resistance of the workpiece.

Adam Race et al.[12] studied the effects of dry, flood and MQL condition on surface integrity of milled SA516 under the context of Environmentally Sustainable Manufacturing (ESM). The Tool wear was significantly lower under dry and MQL machining compared to the use of flood coolant. They reported that the surface roughness, energy consumption, time, cost savings and environmental advantages was much better when MQL is used compared to the use flood coolant.

Jonas Holmberg et al.[13] investigated the surface integrity of Alloy 718 machined by slot milling using ceramic and cemented carbide inserts in order to select the milling strategy, they reported that the cutting edge geometry has a significant impact on the topography. While milling with a worn ceramic insert results in significantly increased surface roughness due to the larger cutting-edge radius, milling with cemented carbide produces topography that is similar because the cutting-edge geometry is intact. They found also that there is a difference between the up, center and down milling in the degree of deformation after milling, and based on their results they suggest the use of up milling for a new insert and down milling for the worn insert. According to EBSD and hardness testing, milling, particularly ceramic milling, severely deformed the surfaces and caused the grain to be refined to a nanocrystalline level. This is most likely the cause of the high tensile stresses' prevalence without distortion or failure.

Muhammad Qaiser Saleem et Salman Mumtaza [14] used wiper inserts of the face milling of Inconel 625 and they investigated the tool life and the surface integrity of workpiece, they found that the axial depth of cut is identified to be the most significant factor for tool life, When machining was done using a values of feed of 0.08 *mm/tooth* and axial depth of cut of 0.25 *mm* with a value of cutting speed of 45 *m/min*, a maximum tool life of 42.8 *min* was reached and the minimum tool life of 3.12 *min* was reached for a values of feed of 0.8 *mm/tooth* and axial depth of cut of 0.5 *mm* with a value of cutting speed of 45 m/min. They found also that Feed per tooth is the statistically the major significant factor (PCR 46.25%) on the surface roughness. They reported that the efficiency of the wiper inserts used in their work appears to be supported by an indirect comparison with other works in literature of face milling of Inconel

625 where other tool types are used and the physical phenomenon in their work provides an adequate explanation for the results and supports them.

Le Gong et al. [15] developed a cryogenic machining system with adjustable jet temperature and they investigated the surface integrity of the milled 35CrMnSiA high-strength steel, they found that the jet temperature have a significant impact on cutting force and surface integrity.

Davis and Singh (2020) [16] examined surface integrity in the end milling of Mg Alloy AZ31B under various conditions (cryogenic, wet, and hybrid) using both cryogenically treated and untreated coated carbide end mills. They discovered that the untreated end mill tool achieved superior surface finish (in terms of roughness and micro-hardness) under cryogenic conditions, at high spindle speeds and low cutting depths and feed rates.

Hassanpour et al. [17] assessed the effect of cutting conditions on surface integrity during the hard milling of 4340 alloy steel using Minimum Quantity Lubrication (MQL). Utilizing Response Surface Methodology (RSM), their statistical analysis highlighted the significant impact of feed rate (49.2%), cutting speed (23.1%), radial cutting depth (14.1%), and axial cutting depth (4%) on surface roughness, revealing a consistent pattern in how axial and radial depths influence roughness.

Yi et al. [18] employed RSM to predict surface roughness in micro milling of aluminum alloy, finding that the model accurately estimated roughness based on cutting conditions. Their results demonstrated increased roughness at higher feed rates and lower spindle speeds.

Santhakumar and Mohammed Iqbal [19] analyzed machined steel surface roughness using RSM, achieving estimates closely matching experimental outcomes with a 6.10% error rate. ANOVA results emphasized feed rate as a predominant factor affecting roughness.

Karkalos et al. [20] compared Artificial Neural Network (ANN) and RSM for estimating and optimizing surface roughness in milling, finding ANN superior for estimation and RSM better for optimization and analysis of influential machining parameters, particularly highlighting feed rate's significant impact.

Kasim et al.[21] explored surface roughness in end ball milling of Inconel 718, noting the influence of flank wear on roughness and the negligible effect of cutting-edge notch wear on machined surface quality.

Bhopale et al. [22] observed smoother surfaces in dry conditions compared to cooled air and increased roughness in double pass cutting versus single pass, emphasizing the cutter path's substantial impact on surface roughness.

Akhtar et al. [23] reported on the performance of SiC whisker-reinforced coated ceramic and PVD-TiAlN coated cemented carbide inserts, noting similar roughness levels at medium cutting speeds and cutting depth and lowest feed even though the two kinds of inserts have distinct cutting parameter ranges, but different inserts performance beyond a 50 mm cutting length.

Najiha and Rahman [24] studied the machining performance of AA6061-T6 using TiAlN + TiN-coated and uncoated tungsten carbide inserts with MQL and TiO2 nanofluid, finding the coated insert superior in producing good surface quality.

Mantle and Aspinwall [25] explored the surface integrity of high-speed milled gamma titanium aluminide, revealing a subsurface hardened layer extending to 300 μm.

Bouzid Saı et al. [26] examined the effects of finishing milling on the surface characteristics of carbon steel (CS) and duplex stainless steel (DSS). They observed an increase in microhardness for carbon steel, correlating with feed rate due to increased chip thickness and tool-chip contact length, they suggested also that higher cutting speeds enhance wear and fatigue resistance.

Xiaoh Wang [27] undertook an intelligent prediction of surface micro-hardness post-milling using smooth support vector regression.

Ginting and Nouari [28] investigated the surface integrity of dry machined titanium alloys, finding microhardness alterations up to 350 μm beneath the surface.

Du Jin and Liu [29] studied surface and subsurface damage in orthogonal milling of FGH95 superalloy, noting that a higher cutting speeds lead to an elevated surface microhardness.

Wang et al. [30] focused on the impact of cutting conditions on microhardness and microstructure in high-speed milling of H13 tool steel, identifying mechanical load-induced severe plastic deformation as the main factor affecting machined surface hardness, which decreases with higher cutting speed and feed per tooth due to thermal softening.

Muñoz-Escalona et al. [31] evaluated the cutting environments' influence on surface integrity of austenitic stainless steel, discovering higher subsurface hardness in specimens milled in cryogenic conditions compared to those in dry conditions.

Yang Houchuan et al. [32] assessed the cutting speed and tool wear's effect on surface integrity of the milled titanium alloy Ti-1023, observing that when the cutting speed increases, the hardening depth decreases. And they reported also, that the tool wear has a major impact on the hardening.

Mathoho et al. [33]   investigated milling parameters' impact on microhardness and microstructure during dry and flood milling of Ti-6Al-4V, noting that flood milling produced higher microhardness values.

I.10. Conclusion

This chapter has covered the topic of milling process, cutting parameters, and the implications of machining with and without lubrication, as well as the cutting temperature generated during the machining, with a focus on aspects of machined surface integrity. Particular attention has been given to the two most important aspects: surface roughness and microhardness in the literature review. This is because controlling surface integrity is a vital consideration in machining. These factors will be explored in depth to highlight their influence on the functional performance and longevity of machined components. Through this discussion, the chapter aims to provide a holistic understanding of the multifaceted nature of milling and its impact on material characteristics and component quality.

CHAPTER II

Experimental Procedure

II.1. Introduction

In this chapter, every step of the experimental procedure for the milling process that will be used in this investigation will be broken down and explained. This starts with a description of the workpiece material, the milling machine that is being used, as well as the specified cutter and inserts. Subsequently, the measurement procedures for cutting temperature, surface roughness, and microhardness will be described in detail. This will be followed by a comprehensive description of the experimental setup. Finally, the experimental results will be presented.

II.2. Description of the workpiece material

In this work, AISI 1060 carbon steel was used as the workpiece material. It is a high-carbon steel, a type of steel with a carbon content ranging from 0.55 % to approximately 0.66 %. This steel is known for its characteristics and properties, making it suitable for a variety of mechanical and engineering applications. In other standards, AISI 1060 may be equivalent or closely related to materials such as C60 in the European standard or S58C in the Japanese standard, depending on the specific composition and properties required. It is used in various applications that require high strength and hardness. Common uses include shearing blades, cutlery, automotive components, and other high-strength parts. It is also utilized in engineering applications where a high strength-to-weight ratio is essential.

The chemical composition of AISI 1060 carbon steel is outlined in the Table II.1.

Table II.1 The AISI 1060 carbon steel chemical composition [34].

Element	Content %
Iron, **Fe**	98.35-98.85
Carbon, **C**	0.55-0.66
Manganese, **Mn**	0.60-0.90
Sulfur, **S**	≤ 0.050
Phosphorus, **P**	≤ 0.040

The physical, mechanical and thermal properties of AISI 1060 carbon steel are outlined in the Table II.2.

Table II.2 The properties of AISI 1060 carbon steel [34].

Properties	Value
Density	7.85 g/cm^3
Ultimate strength	620 MPa
Yield strength	485 MPa
Modulus of elasticity	190-210 GPa
Bulk modulus	140 GPa

Table II.2 Continued.

Properties	Value
Shear modulus	80 *GPa*
Poisson's ratio	0.27-0.30
Brinell Hardness	183
Melting point	1510 *ºC*
Thermal expansion coefficient	11 *µm/m°C*
Thermal conductivity	49.8 *W/mK*

The Figure II.1 show the microstructure of the AISI 1060 carbon steel obtained by the optical microscope Leica DMI5000.
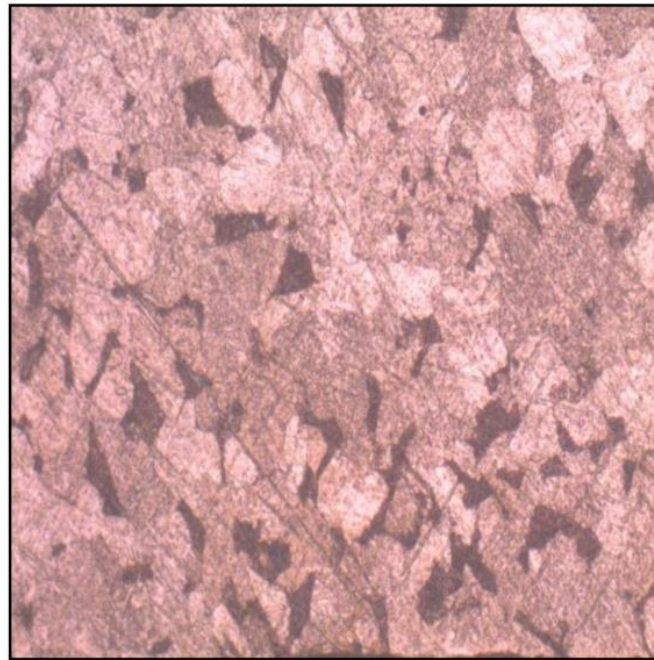
Figure II.1 *The used AISI 1060 carbon steel microstructure obtained by the optical microscope Leica DMI5000.*

II.3. The milling machine

The experimental study utilized a sophisticated milling machine, the Knuth CNC mill Rapimill 700, to conduct the milling tests, as shown in Figure II.2. This machine was selected for its advanced capabilities and its aptness for precision milling operations. The Knuth CNC mill Rapimill 700 is distinguished by its robust construction and advanced control features, which facilitate precise adjustments of milling parameters, critical for the success of machining experiments. One of the pivotal characteristics of this milling machine is its spindle speed, which is capable of achieving an impressive maximum of 10 000 revolutions per minute, while its feed rate can achieve a maximum of 157 mm/min.

Figure II.2 The milling machine Knuth CNC MILL Rapimill 700.

II.4. The cutting tool

The cutter diameter was 50 *mm* (490-050Q22-08M-1040 manufactured by SANDVIK) equipped with five coated carbide inserts (490R-08T308E-ML manufactured by SANDVIK). The cutter and the inserts dimensions are illustrated in Table II.3.

Table II.3 Dimensions of the cutter and the insert [35].

Cutter	Insert
DC = 50 *mm* **LF** = 40 *mm* **APMX** = 5.5 *mm* **KAPR** = 90 *deg* **DCON** = 22 *mm*	**S** = 3.3 *mm* **RE** = 0.8 *mm* **BS** = 1.2 *mm* **LE** = 5.6 *mm* **IC** = 8.5 *mm*

II.5. Measurement procedure

II.5.1. Cutting temperature measurement

In order to assess the temperature distribution on the surface of the workpiece and the cutting tool, a Flir A325 infrared thermal camera was employed, as shown in Figure II.3. The camera is equipped with an InSb Detector and features a resolution of 320×240 pixels, along

with a microscope lens that provides a spatial resolution of 10 microns and a temperature resolution of $+/-2$ degrees Celsius within the specified range. The infrared camera was set up in the same way of the high-speed camera. The recordings were captured at 100 frames per second for a duration of seven seconds. And to ensure an emissivity higher than 0.95, the side of the workpiece facing the camera was painted with matte black color. Then the painted zone temperature was measured by adjusting the emissivity to 0.95. Finally, the nearby surface temperature is measured by setting the emissivity until an equivalent temperature is achieved. The infrared camera FLIR A325 was positioned in orthogonal position to the chips flow direction to determine the temperature on one side of the tool's face.

Figure II.3 *Flir A325 infrared thermal camera.*

II.5.2. Roughness measurement

The roughness meter Mitutoyo Surftest SJ-201 was employed to measure the arithmetical mean roughness value of the machined workpieces as shown in Figure II.4. And here are some of its features and specifications:

The maximum measuring speed 0.5 *mm/s* and the speed of returning is 0.8 *mm/s*, the measuring range is 350 *µm* (– 200 *µm* to + 150 *µm*), stylus diamond cone, skip radius 40 *mm*, tip radius 2 *µm*, measuring force 0.75 *mN*, the cut-off chosen is 0.8 *mm* and the evaluation length is 2.5 *mm*. The Mitutoyo surftest SJ-201 roughness meter has been calibrated to the international standard ISO 5436. Each sample was measured in three different locations to reduce the error range, and the average surface roughness of those three locations was used as final result. The roughness measurement was carried out directly on the machine and without dismantling the workpiece.

Figure II.4 Mitutoyo Surftest SJ-201 roughness meter.

II.5.3. Microhardness measurement

Ultrasonic Portable Hardness Tester Ultramatic 2 HV400 was used to measure the surface microhardness as shown in Figure II.5. The microhardness is measured by the Vickers method with a load of 300 grams with a dwell time of 15 seconds at three locations for each sample to minimize variability and the final microhardness value is determined by choosing the average value of those three results.

Figure II.5 Hardness Tester Ultramatic 2 HV400.

II.6. Experimental setup

The milling operation described in this study involved executing an orthogonal cut, a precise and methodical process, aimed at surfacing prismatic components made of the AISI 1060 carbon steel. This technique is a fundamental aspect of machining and involves a straight cutting movement perpendicular to the direction of the tool's feed, enabling a clean and uniform removal of material from the workpiece surface.

This particular milling operation was conducted under dry conditions, meaning no cutting fluid or coolant was used in the process. Dry milling is often employed for certain materials and applications due to considerations such as cost reduction, environmental impact,

and the avoidance of fluid-related complications. However, it requires careful control of parameters to minimize the adverse effects of heat and friction typically mitigated by coolants.

The components being surfaced had specific dimensions, tailored to the needs of the application or the study's objectives. They measured 250 *mm* in length, 110 *mm* in width, and 50 *mm* in thickness, as illustrated in Figure II.6. These dimensions reflect a sizable piece, indicating a substantial machining operation. The uniformity and precision required in milling such components are crucial, especially given the hardness and strength of AISI 1060 steel, which demands precise tooling and machining parameters to achieve the desired surface finish and dimensional accuracy.
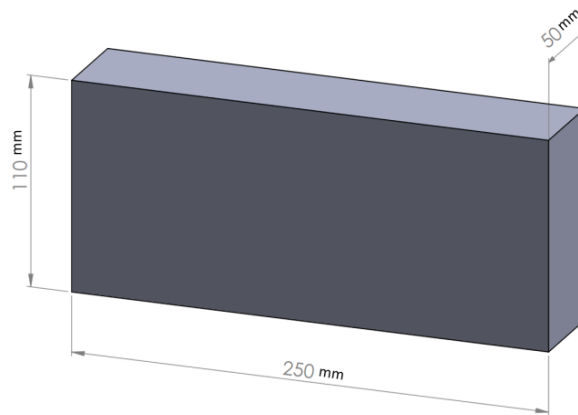
Figure II.6 *Dimensions of the workpiece.*

Figure II.7 shows how the face milling operation was carried out, and Figure III.8 shows the entire experimental setup.
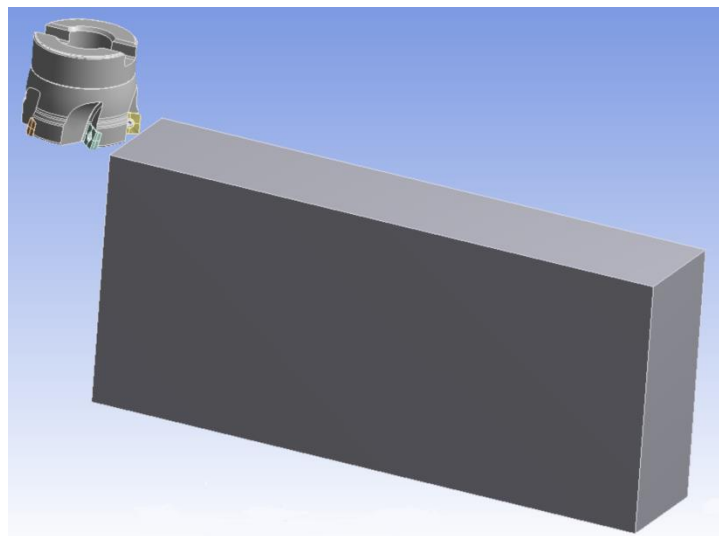
Figure II.7 *The face milling operation of the AISI 1060 carbon steel.*
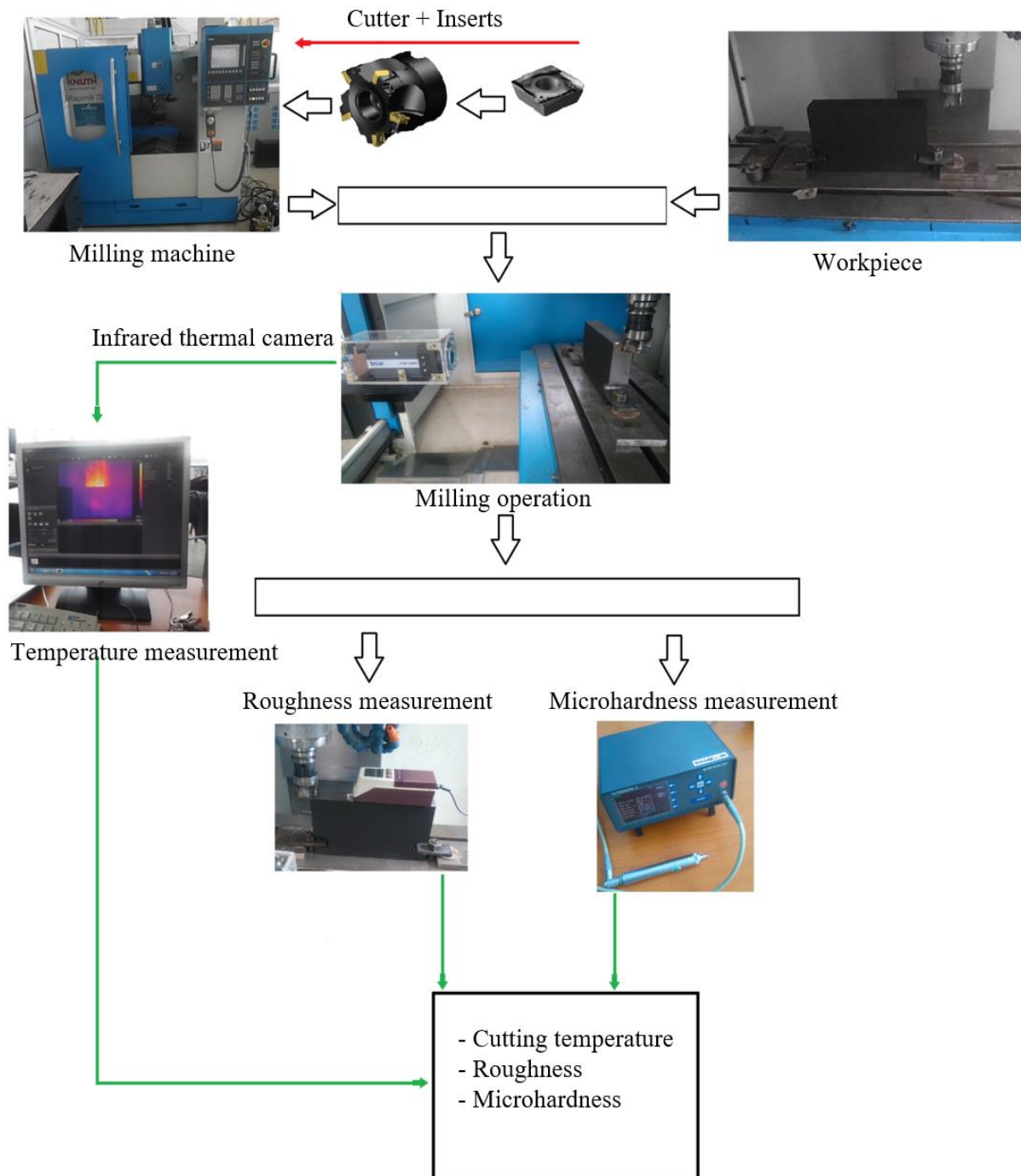
Figure II.8 *Experimental setup.*

In this study, the experimental approach to understand and optimize the milling process of AISI 1060 carbon steel involved a structured method using three distinct input parameters: cutting speed, feed per tooth, and depth of cut, also referred to as factors. These parameters are critical in defining the conditions and outcomes of the milling operation. Each parameter was varied across three different levels, introducing a range of conditions to systematically explore

the effects on the milling process. This variation is key to understanding how changes in one or more parameters can affect the efficiency, quality, and overall success of the milling operation.

The twenty-seven milling tests conducted represent a comprehensive exploration of the parameter space. The choice of three parameters, each with three levels of variation, constitutes a 3×3×3 experimental design, often referred to as a full factorial design. This approach ensures that all possible combinations of parameter levels are tested, providing a thorough understanding of each parameter's impact as well as any interactions between them. Such a methodical approach is common in experimental research to ensure that the findings are comprehensive and the conclusions drawn are robust.

By systematically varying each of these parameters at three distinct levels, the researchers conducted a comprehensive exploration of their combined effects on the milling process of AISI 1060 carbon steel. This variation allows for an in-depth understanding of the optimal settings for each parameter and how they interact with each other, which is crucial for optimizing the milling process and achieving desired outcomes in terms of precision, efficiency, and material characteristics.

Table II.4 presents the different levels of these cutting parameters.

Table II.4 Cutting parameters and their levels.

Factors	Symbol	Units	Level
Cutting speed	V_c	*m/min*	100, 200, 300
Feed per tooth	f_z	*mm/tooth*	0.09, 0.15, 0.18
Depth of cut	a_p	*mm*	0.25, 0.5, 0.75

And for the validation of the RSM model developed in this study, an additional series of eighteen extra tests was done using different cutting parameters. Their results will be used later to accomplish this purpose.

II.7. Presentation of the experimental results

The table III.5 presents the experimental values of the variation of cutting temperature Q_c in °C, surface roughness R_a in *µm* and microhardness H in H_v as a function of the cutting parameters (cutting speed V_c in *m/min*, feed per tooth f_z in *mm/tooth* and depth of cut a_p in *mm*), obtained by the face milling of the AISI 1060 carbon steel.

Table II.5 Experimental data.

Tests	Cutting parameters			Experimental results		
	V_c	f_z	a_p	Q_c	R_a	H
1	300.00	0.09	0.50	156.23	0.53	128.60
2	100.00	0.09	0.25	115.58	0.87	125.60
3	200.00	0.15	0.25	124.67	1.03	116.80
4	300.00	0.18	0.25	119.98	0.77	137.20
5	100.00	0.09	0.50	158.30	1.07	117.40
6	300.00	0.18	0.50	129.00	0.61	135.40
7	100.00	0.15	0.25	109.83	0.95	131.60
8	200.00	0.18	0.50	120.36	0.66	136.40
9	300.00	0.15	0.25	119.66	1.06	126.20
10	300.00	0.15	0.50	136.99	0.66	127.60
11	100.00	0.15	0.50	131.02	1.21	130.20
12	200.00	0.09	0.25	130.00	1.11	126.40
13	200.00	0.09	0.50	149.14	0.66	142.40
14	100.00	0.18	0.50	123.31	1.20	140.80
15	200.00	0.15	0.50	132.37	0.77	130.40
16	300.00	0.09	0.25	119.04	0.60	122.00
17	200.00	0.18	0.25	123.01	1.02	131.40
18	100.00	0.18	0.25	105.98	0.95	125.00
19	100.00	0.09	0.75	128.17	0.80	129.60
20	100.00	0.15	0.75	137.04	1.02	130.20
21	100.00	0.18	0.75	137.63	0.89	138.40
22	200.00	0.09	0.75	150.24	0.85	130.00
23	200.00	0.15	0.75	141.89	0.72	131.60
24	200.00	0.18	0.75	145.97	0.80	124.40
25	300.00	0.09	0.75	174.40	0.71	125.40
26	300.00	0.15	0.75	150.40	0.94	127.60
27	300.00	0.18	0.75	147.14	0.70	122.00

II.8. Conclusion

In this chapter, the equipment and materials that were used in this milling investigation, along with the entire experimental setup have been presented. Subsequently, the results of the experiments that were conducted to demonstrate the variations in cutting temperature, surface roughness, and microhardness as a function of the cutting parameters have been provided.

CHAPTER III
Modelization and Optimization

III.1. Introduction

In this chapter, the Response Surface Methodology (RSM) will be employed to investigate and predict the influence of cutting parameters on cutting temperature, surface roughness, and microhardness by developing three RSM-based mathematical models. Then a multi-objective optimization using Genetic Algorithm (GA) will be conducted to determine the optimal settings for cutting parameters, aiming to minimize both production time and cost per unit. To accomplish this purpose, the developed Ra and H-based RSM mathematical models will be used as constraints in defining the optimization problem instead of using the general empirical models documented in the handbooks to get a better precision and control of the specific Ra and H while satisfying other machining constraints such as tool life, cutting force, and cutting power.

III.2. Literature review "Background of the Study"

Numerous studies have been conducted to examine the impact of cutting conditions on surface integrity and cutting temperature during the milling process. Presented below is a bibliographic search that has explored the impact of cutting conditions on cutting temperature and some aspect of the surface integrity of milled surfaces. For instance, Zahoor et al. [36] evaluated the R_a and H during milling of AISI 316L and they have found that the factors that have the highest significance on R_a are V_f, cutting environment and the axial cutting depth with contribution rates (PCR) of 37.84 %, 27.82%, and 14.56 %, respectively. While cutting environment and axial cutting depth are the major factors impacting the H with PCR of 28.80 % and 29.51 %, respectively. Wang et al. [37] analyzed the influence of cutting speeds and feed rates on R_a in the face milling of Inconel 718, they found that V_c has a negligible impact on the surface roughness compared to f_z, and they reported that the surface hardness increase as V_c and f_z increase, finally they concluded that f_z was the most influencing parameter on fatigue life while V_c has no effect on fatigue life. According to Lu et al. [38] the surface microhardness is more influenced by V_c then the other parameters in the micro-milling of Inconel 718. Abbas et al. [39] reported that V_c stand out as the most influential parameter on cutting temperature. And according to their study when V_c increase the cutting temperature also start to increase progressively. In their work, Ping et al. [40] investigated the surface integrity of 7050-T7451 aluminum alloy milled under dry condition and they studied the mechanism of tool wear. They found that the depth of cut does not affect surface roughness so much compared to the cutting speed and feed rates, also V_c and f_z affect residual stress considerably. Wang and Liu [41] in their work the impacts of cutting conditions on the surface integrity of gamma titanium

aluminide (γ-TiAl alloys) machined by milling they found that f_z had the greatest influence on the surface topography and surface roughness. Saleem and Mumtaza [14] used wiper inserts in the face milling of Inconel 625. they investigated the tool life and the surface integrity of machined part, they found that a_p is the most significant factor on tool life, When the milling was conducted under f_z of 0.08 *mm/tooth* and a_p of 0.25 *mm* with an V_c value of 45 *m/min*, a maximum tool life of 42.8 minutes was reached while a minimum tool life of 3.12 minutes was reached for an f_z of 0.8 *mm/tooth* and a_p of 0.5 *mm* with an V_c value of 45 *m/min*. They found also that Feed per tooth is statistically the major significant factor on the surface roughness with a PCR of 46.25%. Bembenek et al. [42] established that the f_z is the most influential parameter on surface roughness in the face milling of AISI 304 steel. They also reported an interesting observation, a significant increase in surface roughness was noticed in samples machined with an a_p of 0.75 *mm* compared to 0.5 *mm* and 1 *mm*. This increase can possibly be attributed to the cutting depth closely approximating the corner radius of the insert. According to them, there is no similar information in the milling literature.

The realm of milling operations has undergone substantial research focusing on various aspects such as cutting speed, depth of cut and feed per tooth. A noteworthy section of this research corpus aims to optimize these factors using an array of computational and experimental approaches. Optimization not only contributes to better product quality, but also holds the key to reducing costs and production time, two pivotal elements in any manufacturing setting. From employing traditional Response Surface Methodology (RSM) to modern algorithms like and Genetic Algorithms (GA) and Particle Swarm Optimization (PSO), the landscape is vast and multi-disciplinary. However, despite the extensive literature, a comprehensive approach that considers the optimization of both cost and production time in milling processes remains a relatively unexplored territory. The following review highlights the seminal works in this area, pinpointing the various methodologies and outcomes that have shaped our current understanding of milling optimization:

For instance, Kumar [43] used GA to optimize the surface roughness and machining time. The results of their study showed that the GA-based optimization model was capable to reduce both surface roughness and machining time effectively. Yang [44] focused on the optimization of machining parameters for multi-pass face milling using a chaotic imperialist competitive algorithm (CICA) with an efficient constraint-handling mechanism. The study demonstrated the effectiveness of using the CICA-based optimization model with an efficient constraint-handling mechanism for multi-objective optimization. In their research, Fang et al.

[45] optimized the milling process using PSO combined with Simulated Annealing (SA) algorithms to minimize the processing time (*PT*), carbon emissions (*CE*) and production cost (*PC*). The authors found that the best cutting regime was achieved to be 285.1 *m/min* of V_c, 1.36 *mm/tooth* of f_z and 0.3 *mm* of a_p, resulting in minimum *PT* of 96.65 (*s*), *CE* of 39.36 (10^{-3}. *kgCO*2) and *PC* of 48.34 ($). Li et al. [46] aimed to optimize the cutting conditions to improve the processing rate, surface roughness and cutting force in high speed milling. RSM and improved Teaching-Learning-Based Optimization algorithm were employed for modeling and optimizing the results. Su et al. [47] interested in improving cutting quality, energy consumption and production rate during the machining operation. Grey relational analysis has been applied to transform the complex multi-objective optimization problem to a simple one. Rana et al. [48] used multi-criteria decision making through grey relational analysis to optimize both of surface microhardness and roughness in the face milling of AISI 52,100 alloy steel. Zhao et al. [49] focused on the multi-objective optimization of cutting parameters and tool geometry angles in the context of NC milling process to simultaneously minimize both machining time and energy consumption using NSGA-II. The results of the optimization model were validated by comparing them with the experimental result. Pham and Thuy [50] applied MOORA decision making method to get the optimum cutting conditions in face milling. The researchers recommended to use 300 *m/min* of V_c, 0.1 *mm/tooth* of f_z and 0.9 *mm* of a_p for maximum *MRR* and minimum R_a and F_c. Zhou et al. [51] focused on minimizing of both machining time (*MT*) and energy consumption per unit of removed material (*UEC*) in the end milling process through GA. Tool life and surface roughness and other conditions were taken as constraints during the construction of the optimization problem. The study results show the suitability of using GA model to obtain appropriate milling parameters leading to minimum *MT* and *UEC*. In subsequent work reported by Rajeswari et al [52], established RSM based models R_a, F_c and *MRR* in end milling process. Then GA was utilized to optimize the milling responses. The pareto solutions were achieved to be in ranges of 1032-1958 *RPM* of spindle speed, 0.02-0.04 *mm/rev* of feed, 1.07-1.87 *mm* of depth of cut, 0.2-1.09 *µm* of R_a, 152-2513 mm^3/min of *MRR* and 11.7-131.2 *N* of F_c. Xu et al. [53] carried out an experimental study to analyze the machinability of AF 1410 steel in milling process. The researchers have used NSGA-II method for the optimization purpose. As a results, a set of optimal alternatives was attained leading to improve the considered machining performance. Cheng et al. [54] investigated the impact of the cutting parameter on the surface roughness and other responses during milling operations. Artificial bee colony (ABC) algorithm and RSM were used for the multi-objective optimization.

By comparing the two methods, it was found that the ABC method provide promising results than the RSM optimization method. Wang et al. [55] did a multi-objective optimization using NSGA-III to optimize the machining performance in the micro-milling process. They reported that NSGA-III has a superior efficacy in solving multi-objective optimization problem and can successfully achieve globally optimal results. Tran et al. [56] used RSM to predict and optimize the roughness and *MRR* in the milling of 7075 Aluminium alloy. The study found that the developed regression models for R_a and *MRR* using the RSM approach have significant R^2 values of 97.67 % and 99.36 %, respectively. Also, the optimal cutting conditions were determined using the RSM multi-objective optimization process. Huang et al. [57] used in their work RSM to study the impact of cutting parameters in the ball-end hard milling process. They found that radial depth of cut has the highest contribution ratio (62.05 %) on the surface roughness. While surface microhardness is most significantly affected by feed per tooth and spindle speed with a percentage contribution ratio of 25.14 % and 24.79 % respectively. Moreover, when a high spindle speed is selected, the impact of the radial depth of cut on the microhardness isn't obviously apparent. Finally, they proposed an optimization scheme based on response surface of desirability function to optimize the cutting condition.

Based on literature review, numerous studies have focused on using empirical models documented in the handbooks to optimize the machining responses in milling process. However, to author best knowledge, there is no research published optimizes the cost and production time in milling process by using GA while considering the R_a and *H* based-RSM models as constraints in defining the optimization problem.

The primary objective of this work is twofold: first, to empirically investigate the influence of cutting parameters (V_c, f_z and a_p) on key milling responses-namely, cutting temperature (Q_c), surface roughness (R_a), and microhardness (*H*). Second, it aims to introduce a novel optimization strategy by utilizing Genetic Algorithms (GA) to concurrently minimize production time and cost in the milling process, a departure from previous studies primarily focused on the generalized empirical models commonly documented in the handbooks.

What sets this research apart is the pioneering integration of Genetic Algorithms with specific Response Surface Methodology (RSM) models, specifically R_a and *H* based models, as defining constraints in the optimization problem. This innovative approach offers a more nuanced and precise means of optimizing the milling process by considering both surface quality measures (R_a, *H*) alongside conventional machining constraints, filling a significant gap in the existing literature.

III.3. Response Surface Methodology

III.3.1. Response Surface Methodology

One of the most powerful and highly effective technique that combines mathematical and statistical methods to study the relation between multiple independent factors and a specified response is Response Surface Methodology. known as RSM is particularly useful in the fine-tuning of complex processes where the interactions between variables can be significant. By using this methodology, researchers can not only anticipate the effects of individual variables but also understand the combined effect of variables on the response. This makes it an invaluable tool for optimizing processes, improving quality and yield, and in exploratory studies of new systems. In practical applications, RSM can be employed in various phases of a process, from the screening stage, where important factors are identified, to the optimization stage, where the levels of factors that maximize or minimize the response are determined. It is widely used in numerous fields such as engineering, product development, manufacturing, agriculture, and others.

III.3.2. Developing Mathematical Relationships and Regression Analysis

To empirically determine the coefficients of the regression models of response surface, version 13.0 of the Design Expert software was utilized. And ANOVA (Analysis of Variance) was employed to ascertain the significance and impact of the specified input parameters on the responses, derived from a series of experimental tests of the milling process using the Design of Experiments methodology. This analysis also facilitates the elucidation of the interactive effects of those parameters.

Figure III.1 shows a schema of the response surface method system.
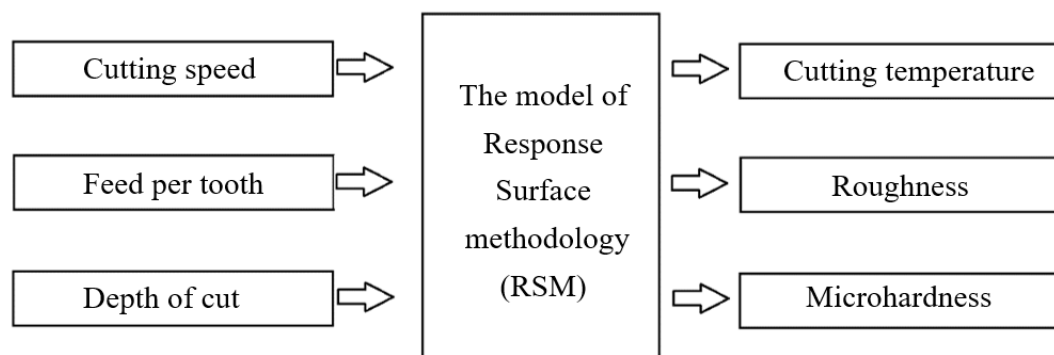
Figure III.1 *Response Surface Method System.*

a) Cutting temperature

Table III.1 shows the results of ANOVA table for response surface reduced quartic model for cutting temperature.

Table III.1 ANOVA for Reduced Quartic model of cutting temperature.

Source	Sum of Squares	df	Mean Square	F-value	p-value	
Model	6754.85	15	450.32	78.32	< 0.0001	significant
A-Vc	11.00	1	11.00	1.91	0.1941	
B-Fz	1406.09	1	1406.09	244.54	< 0.0001	
C-ap	614.14	1	614.14	106.81	< 0.0001	
AB	18.20	1	18.20	3.17	0.1028	
AC	204.47	1	204.47	35.56	< 0.0001	
BC	5.96	1	5.96	1.04	0.3304	
A²	53.82	1	53.82	9.36	0.0109	
B²	9.33	1	9.33	1.62	0.2291	
C²	0.9200	1	0.9200	0.1600	0.6968	
ABC	310.01	1	310.01	53.91	< 0.0001	
A²C	113.35	1	113.35	19.71	0.0010	
AC²	195.66	1	195.66	34.03	0.0001	
BC²	593.38	1	593.38	103.20	< 0.0001	
A²C²	153.98	1	153.98	26.78	0.0003	
ABC²	87.06	1	87.06	15.14	0.0025	
Residual	63.25	11	5.75			
Cor Total	6818.10	26				

Std. Dev.	2.40	**R²**	0.9907	
Mean	133.98	**Adjusted R²**	0.9781	
C.V. %	1.79	**Predicted R²**	0.9303	
		Adeq Precision	35.9391	

Table III.1 shows the results of the ANOVA analysis of cutting temperature, An F-value of 78.32 for the model suggests its significance, with only 0.01 % probability that such a high F-value could result from random variations. Model terms are considered significant when P values are below 0.0500. The predicted R-Squared value of 0.9303 agrees acceptably with the adjusted R-Squared of 0.9781, as their difference is under 0.2. Furthermore, an Adequate Precision ratio of 35.939, which exceeds the benchmark value of 4, indicates a sufficient signal. This ratio confirms the model's adequacy in predicting experimental outcomes.

Based on the ANOVA results, The most crucial process parameters have been identified, the results show that f_z and a_p were the most significant factors on cutting temperature with a

contribution of 20.62 % and 9 % respectively. In addition, the most significant interaction factors are $f_z \times a_p \times a_p$ followed by $V_c \times f_z \times a_p$ with a contribution of 8.7 % and 4.5 % respectively. The final mathematical model that incorporates the relationship between those parameters is presented below:

$$Q_c = \begin{pmatrix} -257.427 + 2.39409 \times V_c + 928.333 \times f_z + 1969.45 \\ \times a_p - 1.80497 \times V_c \times f_z - 10.6515 \times V_c \times a_p \\ -7217.19 \times f_z \times a_p - 0.00484451 \times V_c^2 + 705.345 \\ \times f_z^2 - 2015.41 \times a_p^2 + 14.5157 \times V_c \times f_z \times a_p \\ +0.0193237 \times V_c^2 \times a_p + 10.6999 \times V_c \times a_p^2 \\ +8242.39 \times f_z \times a_p^2 - 0.0171944 \times V_c^2 \times a_p^2 \\ -19.9494 \times V_c \times f_z \times a_p^2 \end{pmatrix} \qquad (III.1)$$
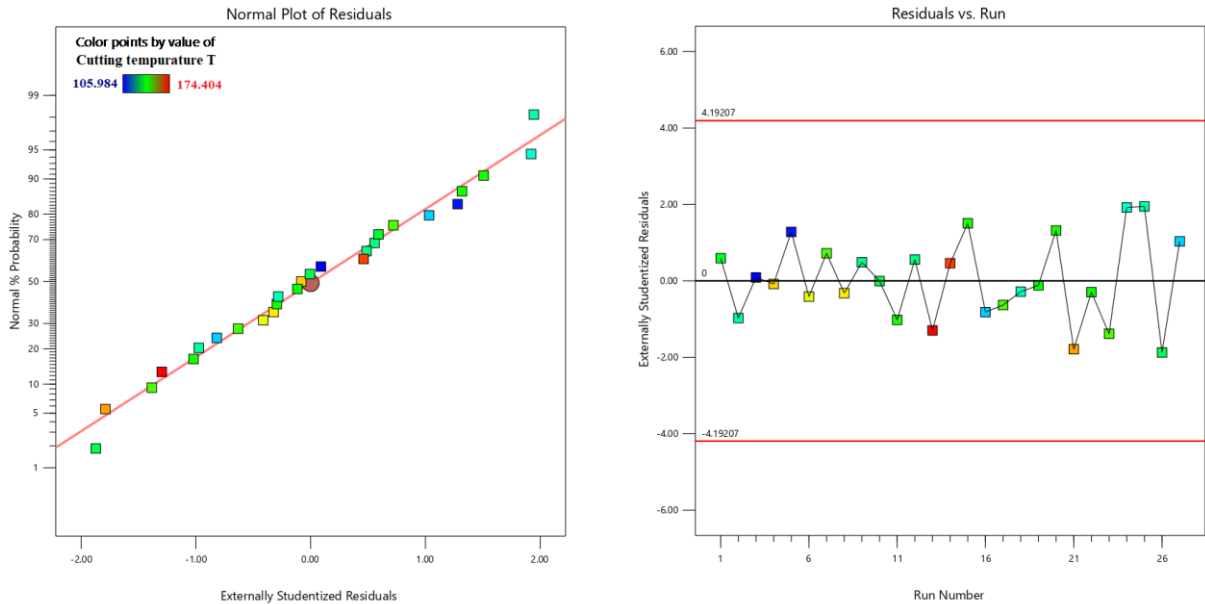
Figure III.2 *The residual graph for cutting temperature model: (a) residual normal plot, (b) residual versus run.*

Figure III.2 presents the residual normal plot and the plot of residuals against the run for cutting temperature. In Figure III.2 (a), the proximity of the points to the straight line is evident, indicating a normal distribution of residuals. Furthermore, Figure III.2 (b) reveals no discernible pattern or unused structure in the plot of residuals versus run number. These observations lead to the conclusion that the proposed model is satisfactory, as these two criteria are crucial for establishing the model's adequacy.

b) Roughness

Table III.2 shows the results of ANOVA table for response surface reduced quartic model for roughness.

<div align="center">Table III.2 ANOVA for Reduced Quartic model of roughness.</div>

Source	Sum of Squares	df	Mean Square	F-value	p-value	
Model	1.95	16	0.1218	13.26	0.0001	significant
A-Vc	0.2810	1	0.2810	30.59	0.0003	
B-Fz	0.0039	1	0.0039	0.4248	0.5292	
C-ap	0.1471	1	0.1471	16.01	0.0025	
AB	0.0061	1	0.0061	0.6655	0.4336	
AC	0.0029	1	0.0029	0.3103	0.5898	
BC	0.0123	1	0.0123	1.34	0.2747	
A^2	0.1026	1	0.1026	11.17	0.0075	
B^2	0.0003	1	0.0003	0.0304	0.8652	
C^2	0.2201	1	0.2201	23.96	0.0006	
ABC	0.0294	1	0.0294	3.20	0.1039	
A^2B	0.0417	1	0.0417	4.54	0.0589	
A^2C	0.0935	1	0.0935	10.18	0.0096	
AB^2	0.0659	1	0.0659	7.18	0.0231	
AC^2	0.3788	1	0.3788	41.24	< 0.0001	
A^2B^2	0.0539	1	0.0539	5.87	0.0359	
A^2C^2	0.0906	1	0.0906	9.86	0.0105	
Residual	0.0919	10	0.0092			
Cor Total	2.04	26				

Std. Dev.	0.0958	**R²**	0.9550
Mean	1.22	**Adjusted R²**	0.8829
C.V. %	7.83	**Predicted R²**	0.7136
		Adeq Precision	14.6105

Table III.2 shows the results of the ANOVA analysis of surface roughness, An F-value of 13.26 for the model suggests its significance, with only 0.01 % probability that such a high F-value could result from random variations. The predicted R-Squared value of 0.7136 agrees acceptably with the adjusted R-Squared of 0.8829, as their difference is under 0.2. Furthermore, an Adequate Precision ratio of 14.610 indicates a sufficient signal. This ratio confirms the model's adequacy in predicting experimental outcomes.

According to the ANOVA analysis, the most crucial process parameters have been identified, the factor that has the highest significance on surface roughness is V_c with a contribution of 13.77 %, the same result was found in literature [39], [58] and [59]. Moreover,

the interaction factor that has the highest significance is $V_c \times a_p \times a_p$ with a contributing of 18.56%. The final mathematical model that incorporates the relationship between those parameters is presented below:

$$R_a = \begin{pmatrix} 11.94131 - 0.127737 \times V_c - 89.07276 \times f_z \\ -21.86460 \times a_p + 1.09198 \times V_c \times f_z + 0.232765 \\ \times V_c \times a_p - 7.79114 \times f_z \times a_p + 0.000341 \times V_c^2 \\ +316.51250 \times f_z^2 + 21.22230 \times a_p^2 + 0.052911 \\ \times V_c \times f_z \times a_p - 0.003299 \times V_c^2 \times f_z - 0.000478 \\ \times V_c^2 \times a_p - 3.82465 \times V_c \times f_z - 0.216064 \times V_c \times a_p^2 \\ +0.011377 \times V_c^2 \times f_z^2 + 0.000417 \times V_c^2 \times a_p^2 \end{pmatrix}^{-1} \qquad (III.2)$$

Figure III.3 *The residual graph for roughness model: (a) residuals normal plot, (b) residual versus run.*

Figure III.3 presents the residual normal plot and the plot of residuals against the run for surface roughness. In Figure III.3 (a), the proximity of the points to the straight line is evident, indicating a normal distribution of residuals. Furthermore, Figure III.3 (b) reveals no discernible pattern or unused structure in the plot of residuals versus run number. These observations lead to the conclusion that the proposed model is satisfactory, as these two criteria are crucial for establishing the model's adequacy.

c) Microhardness

Table III.3 shows the results of ANOVA table for response surface reduced fifth model for microhardness.
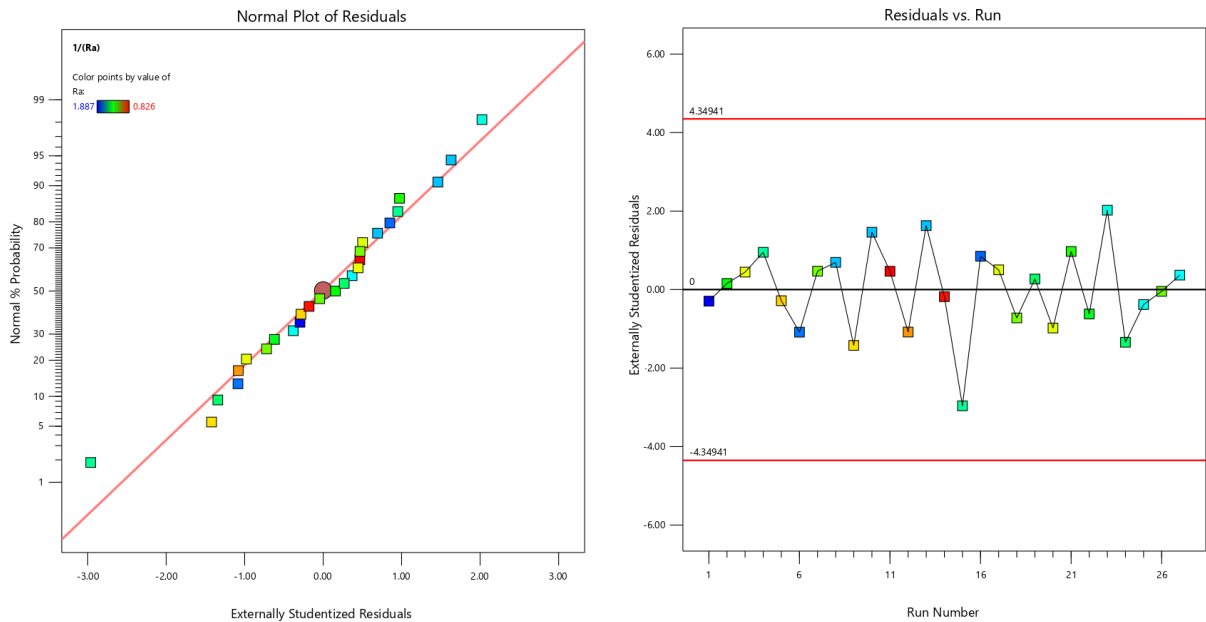
Table III.3 ANOVA for Reduced Fifth model of microhardness.

Source	Sum of Squares	df	Mean Square	F-value	p-value	
Model	1055.25	25	42.21	10853.66	0.0076	significant
A-Vc	0.0114	1	0.0114	2.93	0.3366	
B-Fz	18.36	1	18.36	4720.66	0.0093	
C-ap	132.21	1	132.21	33997.63	0.0035	
AB	68.89	1	68.89	17714.57	0.0048	
AC	19.45	1	19.45	5001.76	0.0090	
BC	28.09	1	28.09	7223.14	0.0075	
A^2	20.93	1	20.93	5381.09	0.0087	
B^2	73.10	1	73.10	18797.21	0.0046	
C^2	44.23	1	44.23	11373.18	0.0060	
ABC	98.00	1	98.00	25200.00	0.0040	
A^2B	152.26	1	152.26	39153.39	0.0032	
A^2C	81.83	1	81.83	21041.95	0.0044	
AB^2	2.40	1	2.40	617.51	0.0256	
AC^2	4.56	1	4.56	1172.58	0.0186	
B^2C	107.25	1	107.25	27578.94	0.0038	
BC^2	11.16	1	11.16	2869.49	0.0119	
A^2B^2	18.13	1	18.13	4663.02	0.0093	
A^2BC	6.00	1	6.00	1542.86	0.0162	
A^2C^2	104.05	1	104.05	26756.26	0.0039	
AB^2C	78.26	1	78.26	20123.45	0.0045	
ABC^2	56.43	1	56.43	14509.71	0.0053	
B^2C^2	21.85	1	21.85	5618.00	0.0085	
A^2B^2C	76.55	1	76.55	19683.00	0.0045	
A^2BC^2	57.71	1	57.71	14840.33	0.0052	
AB^2C^2	0.4402	1	0.4402	113.20	0.0597	
Residual	0.0039	1	0.0039			
Cor Total	1055.22	26				

Std. Dev.	0.0624	**R²**	1.0000	
Mean	129.28	**Adjusted R²**	0.9999	
C.V. %	0.0482	**Predicted R²**	0.9872	
		Adeq Precision	418.4241	

Table III.3 shows the results of the ANOVA analysis of microhardness, An F-value of 10853.66 for the model suggests its significance, with only 0.76 % probability that such a high F-value could result from random variations. The predicted R-Squared value of 0.9872 agrees acceptably with the adjusted R-Squared of 0.9999, as their difference is under 0.2. Furthermore, an Adequate Precision ratio of 418.4241 indicates a sufficient signal. This ratio confirms the model's adequacy in predicting experimental outcomes.

Based on the ANOVA results, The most crucial process parameters have been identified, according to the results the factor that has the highest significance on surface microhardness is a_p with a contribution of 12.43 %. Moreover, the most significant interaction factors are $V_c \times V_c \times f_z$ followed by $f_z \times f_z \times a_p$ with a contribution of 14.42 % and 10.16 % respectively. The final mathematical model that incorporates the relationship between those parameters is presented below:

$$H = \begin{pmatrix} -327.467 + 4.506 \times V_c + 12213.6 \times f_z - 564.4 \times a_p - 124.096 \times V_c \\ \times f_z + 9.76 \times V_c \times a_p - 15845.2 \times f_z \times a_p - 0.01079 \times V_c^2 - 55535 \\ \times f_z^2 + 1920 \times a_p^2 + 105.367 \times V_c \times f_z \times a_p + 0.286296 \times V_c^2 \times f_z \\ -0.0194 \times V_c^2 \times a_p + 556.42 \times V_c \times f_z^2 - 24.608 \times V_c \times a_p^2 + 112123 \\ \times f_z^2 \times a_p - 7054.81 \times f_z \times a_p^2 - 1.25864 \times V_c^2 \times f_z^2 - 0.272333 \times V_c^2 \\ \times f_z \times a_p + 0.05224 \times V_c^2 \times a_p^2 - 898.889 \times V_c \times f_z^2 \times a_p + 146.089 \\ \times V_c \times f_z \times a_p^2 - 23901.2 \times f_z^2 \times a_p^2 + 2.1 \times V_c^2 \times f_z^2 \times a_p - 0.281333 \\ \times V_c^2 \times f_z \times a_p^2 - 63.7037 \times V_c \times f_z^2 \times a_p^2 \end{pmatrix} \qquad \text{(III.3)}$$

Figure III.4 *The residual graph for microhardness model: (a) residuals normal plot, (b) residual versus run.*

Figure III.4 presents the residuals normal plot and the plot of residuals against the run for microhardness, the residual normal plot results in Figure III.4 (a) show that all the points are in straight line and the same thing in the Figure III.4 (b) of the residuals versus run which indicate that there are no errors and the proposed model is almost perfect.

III.4. Results and discussion

III.4.1. Results

For verification, the developed models, constructed using twenty-seven experimental results, will be tested by comparing these experimental outcomes with the predicted results from the regression models.

Figure III.5 illustrates the superposition of the experimental and predicted values by the regression models.
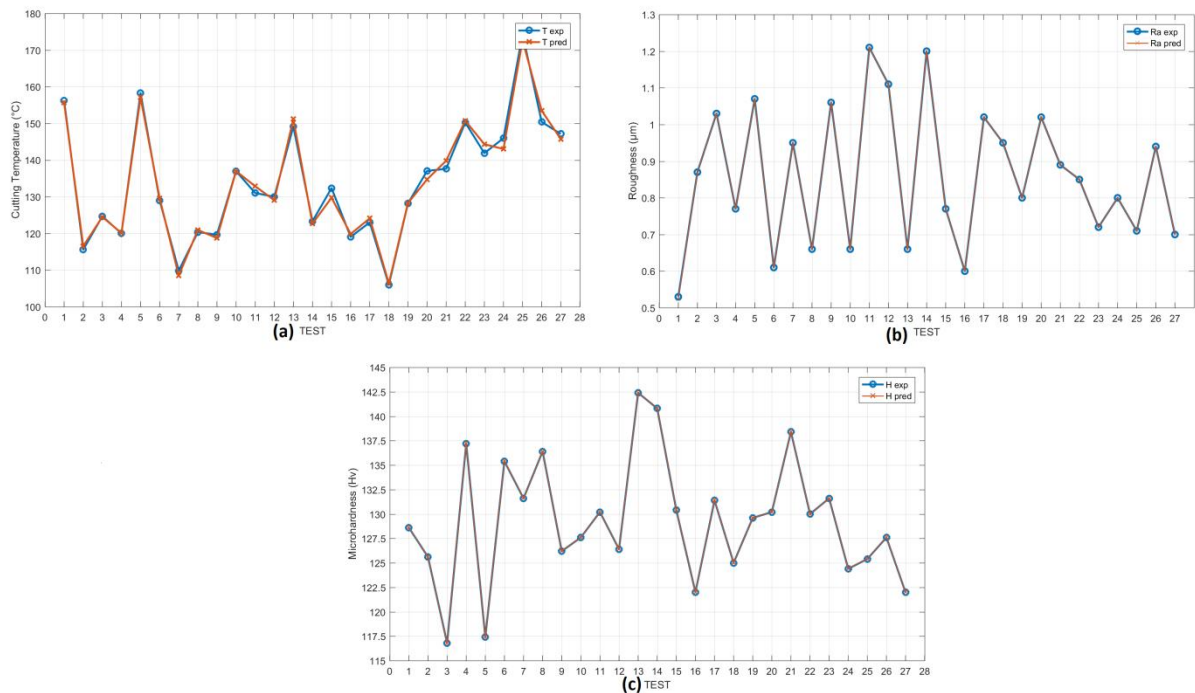
Figure III.5 *Experimental versus predicted result: (a) cutting temperature, (b) roughness, (c) microhardness.*

From the Figure III.5 (a) a similarity is noticed between the experimental values and the predicted values of cutting temperature and from Figure III.5 (b) and (c) it is notice that the experimental values and the predicted values of roughness and microhardness are almost identical, that's confirm that the model works correctly and can be used to analyze the results.

III.4.2. Validation of the developed model

To validate the model, eighteen experimental values, not included in the model's construction, were examined as detailed in Tables III.4, III.5 and III.6. The model's precision and error were investigated using the final equations of the cutting temperature, roughness and microhardness that connects the inputs and outputs parameters with the regression model by comparing their results with the experimental results.

To determine the error's percentage of those 18 tests; Formula 4 is utilized.

$$e_i = \frac{1}{N} \sum_{i=1}^{N} \left[\frac{|V_{exp} - V_{pred}|}{V_{exp}} \right] \times 100 \qquad (III.4)$$

V_{exp}: The experimental value.

V_{pred}: The predicted value.

In this case $N = 18$ tests.

e_i: Error rate

To determine the accuracy percentage of those 18 tests; Formula 5 is utilized.

$$A = \frac{1}{N} \sum_{i=1}^{N} \left[1 - \frac{|V_{exp} - V_{pred}|}{V_{exp}} \right] \times 100 \qquad (III.5)$$

V_{exp}: The experimental value.

V_{pred}: The predicted value.

In this case $N = 18$ tests.

A: Accuracy

The Table III.4 show the results of the experimental versus the predicted values of the cutting temperature.

Table III.4 Experimental versus predicted values of cutting temperature.

Tests	Cutting parameters			Cutting temperature results			
	V_c	f_z	a_p	$Q_{c_{exp}}$	$Q_{c_{pred}}$	Error %	Accuracy %
1	250	0.09	0.25	122.34	127.17	3.95	96.05
2	300	0.12	0.25	121.06	118.65	1.99	98.01
3	250	0.12	0.5	134.64	141.46	5.06	94.94
4	250	0.15	0.5	124.14	132.07	6.39	93.61
5	300	0.12	0.5	143.66	145.68	1.41	98.59
6	150	0.09	0.5	146.25	152.84	4.51	95.49
7	150	0.12	0.5	134.46	140.79	4.71	95.29
8	200	0.12	0.25	125.07	126.14	0.86	99.14

Table III.4 Continued.

Tests	Cutting parameters			Cutting temperature results			
	V_c	f_z	a_p	$Q_{c_{\exp}}$	$Q_{c_{pred}}$	Error %	Accuracy %
9	200	0.12	0.5	133.29	139.83	4.91	95.09
10	100	0.12	0.25	103.05	111.87	8.56	91.44
11	250	0.18	0.5	118.33	123.96	4.75	95.25
12	150	0.15	0.75	142.59	139.58	2.11	97.89
13	150	0.18	0.75	147.99	141.49	4.39	95.61
14	200	0.12	0.75	150.20	146.90	2.20	97.80
15	250	0.09	0.75	162.24	161.79	0.28	99.72
16	250	0.12	0.75	155.22	154.74	0.31	99.69
17	250	0.18	0.75	143.10	144.44	0.94	99.06
18	250	0.15	0.75	148.99	148.96	0.02	99.98
The average						**3.19 %**	**96.81 %**

The table III.5 show the results of the experimental versus the predicted values of the roughness.

Table III.5 Experimental versus predicted values of roughness.

Tests	Cutting parameters			Roughness results			
	V_c	f_z	a_p	$R_{a_{\exp}}$	$R_{a_{pred}}$	Error %	Accuracy %
1	250	0.09	0.25	0.98	0.95	3.16	96.84
2	300	0.12	0.25	0.99	1.00	1.39	98.61
3	250	0.12	0.5	0.62	0.67	7.98	92.02
4	250	0.15	0.5	0.65	0.67	3.70	96.30
5	300	0.12	0.5	0.58	0.63	9.26	90.74
6	150	0.09	0.5	0.82	0.83	1.24	98.76
7	150	0.12	0.5	0.92	0.94	1.74	98.26
8	200	0.12	0.25	1.1	1.06	3.62	96.38
9	200	0.12	0.5	0.75	0.77	2.70	97.30
10	100	0.12	0.25	0.99	0.92	6.72	93.28
11	250	0.18	0.5	0.52	0.57	10.39	89.61
12	150	0.15	0.75	0.75	0.81	7.34	92.66
13	150	0.18	0.75	0.82	0.85	3.20	96.80
14	200	0.12	0.75	0.68	0.74	8.35	91.65
15	250	0.09	0.75	0.72	0.80	11.65	88.35
16	250	0.12	0.75	0.74	0.78	5.76	94.24
17	250	0.18	0.75	0.72	0.75	4.34	95.66
18	250	0.15	0.75	0.79	0.77	3.15	96.85
The average						**5.32 %**	**94.68 %**

The table III.6 show the results of the experimental versus the predicted values of the microhardness.

Table III.6 Experimental versus predicted values of microhardness.

Tests	Cutting parameters			Microhardness results			
	V_c	f_z	a_p	$H_{\exp}$	H_{pred}	Error %	Accuracy %
1	250	0.09	0.25	122.2	124.86	2.18	97.82
2	300	0.12	0.25	123.2	121.16	1.66	98.34
3	250	0.12	0.5	131.4	131.04	0.28	99.72
4	250	0.15	0.5	126.6	129.41	2.22	97.78
5	300	0.12	0.5	122.2	125.33	2.56	97.44
6	150	0.09	0.5	132.8	134.75	1.47	98.53
7	150	0.12	0.5	132.4	129.56	2.14	97.86
8	200	0.12	0.25	117.4	115.12	1.94	98.06
9	200	0.12	0.5	135.2	132.45	2.04	97.96
10	100	0.12	0.25	130.6	131.81	0.93	99.07
11	250	0.18	0.5	133.4	135.48	1.56	98.44
12	150	0.15	0.75	134.4	131.57	2.10	97.90
13	150	0.18	0.75	132.8	129.97	2.13	97.87
14	200	0.12	0.75	130.3	133.46	2.43	97.57
15	250	0.09	0.75	128.6	128.34	0.20	99.80
16	250	0.12	0.75	130.6	132.47	1.43	98.57
17	250	0.18	0.75	123.8	121.78	1.63	98.37
18	250	0.15	0.75	129.6	130.29	0.53	99.47
The average						**1.63 %**	**98.37 %**

Figure III.6 shows the superposition between the experimental values and the predicted values for the 18 validation tests.
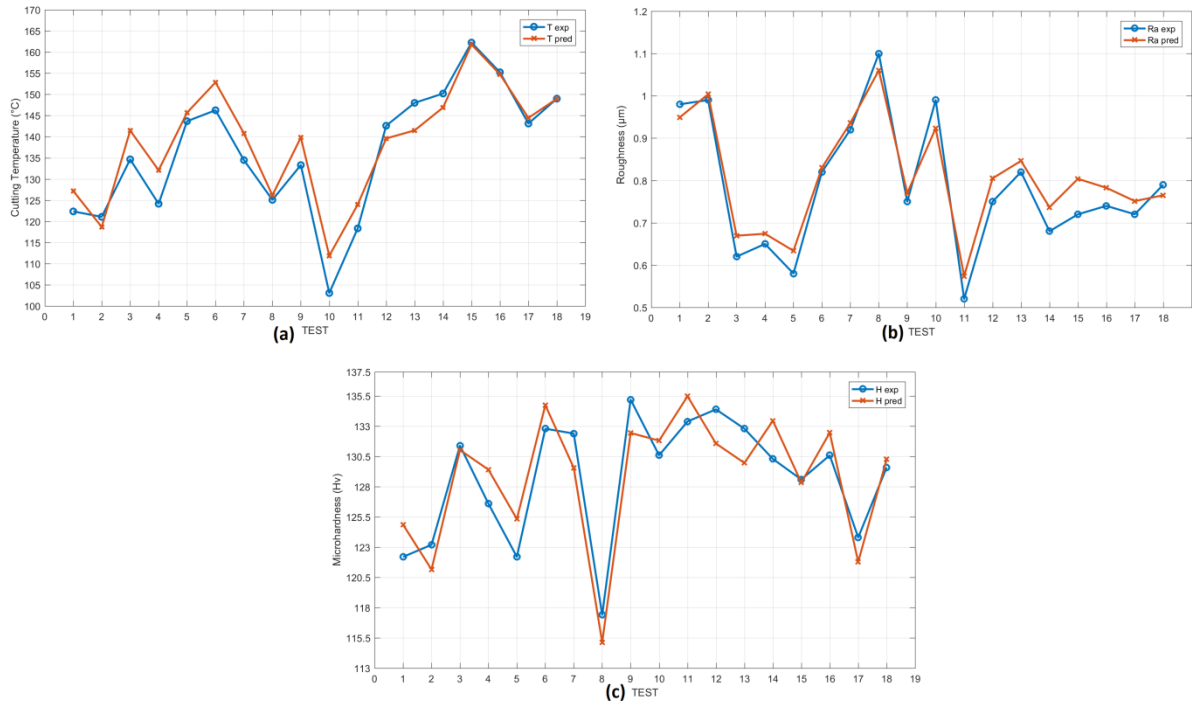
Figure III.6 *Experimental versus predicted result: (a) cutting temperature, (b) roughness, (c) microhardness (validation).*

According to Tables III.4, III.5 and III.6 the average error rates are 3.19 % for the cutting temperature, 5.32 % for roughness and 1.63 % for microhardness, this implies that the prediction models, which utilizes Response Surface Methodology, functions effectively and with high precision.

While these error rates signify a high level of accuracy, it's essential to contextualize these values in comparison to industry standards or similar predictive models to fully appreciate their performance within the milling domain.

The achieved precision implies that these RSM-based models can potentially serve as reliable predictive tools for assessing cutting temperature, surface roughness, and microhardness before initiating the milling process. However, further validation across a diverse range of milling conditions or materials would fortify the claim of their general applicability and reliability in real-world machining scenarios.

Understanding the practical implications of these error rates is crucial, as it elucidates how accurately these models can guide decision-making or machining operations. This precision can significantly impact the optimization of milling processes, but a more comprehensive understanding of their limitations and applicability under varying conditions is essential for broader industry adoption.

III.4.3. Graphical representation of results

a) Cutting temperature

Figure III.7 displays the surfaces generated through the RSM, detailed as follows:

- Surface (a) shows the variation in cutting temperature relative to V_c and f_z, at a constant a_p of 0.5 *mm*.
- Surface (b) shows the variation in cutting temperature relative to V_c and a_p, at a constant f_z of 0.15 *mm/tooth*.
- Surface (c) shows the variation in cutting temperature relative to a_p and f_z, at a constant V_c of 200 *m/min*.
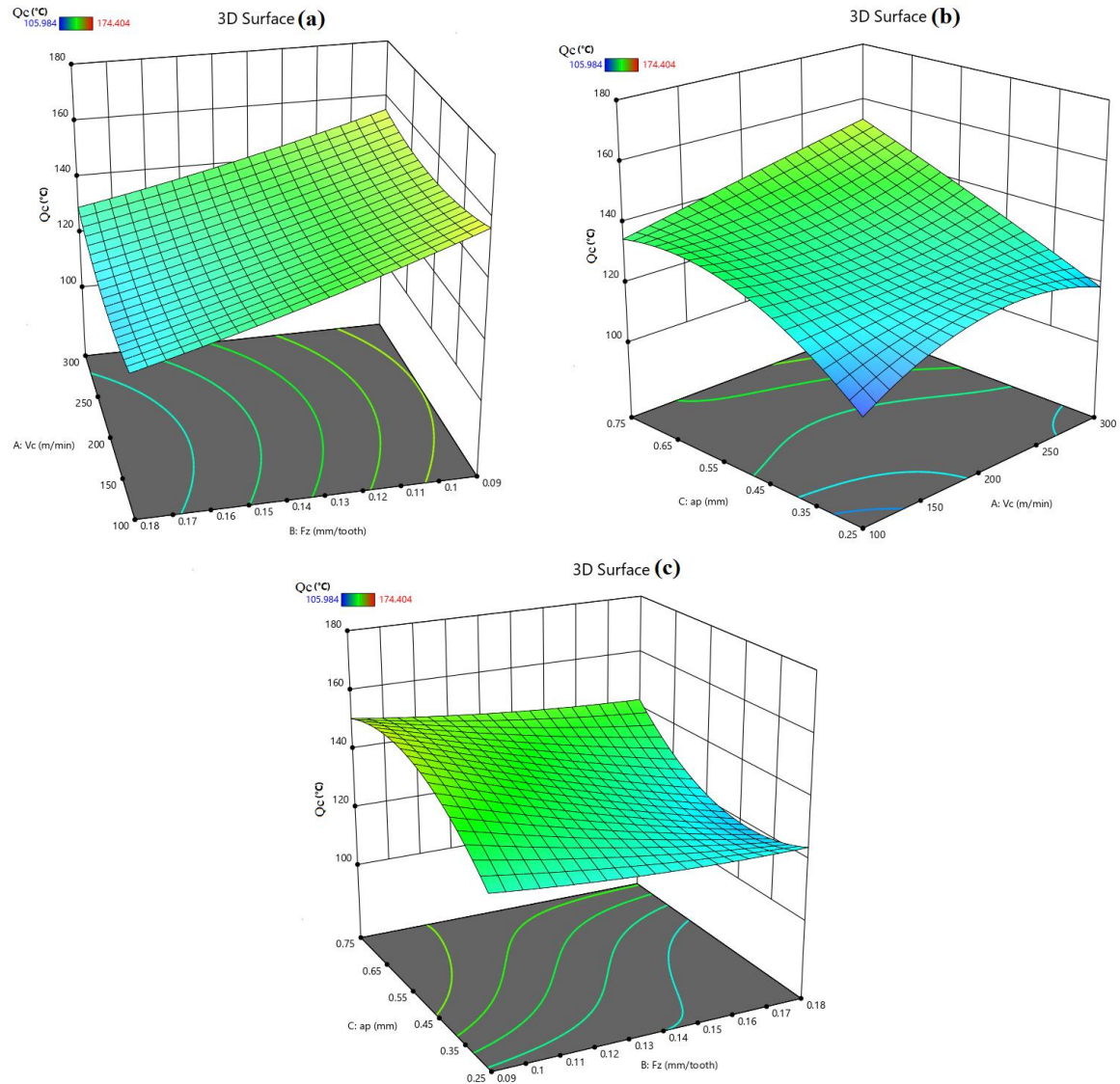
Figure III.7 *Variation of the predicted cutting temperature as a function of the cutting parameters.*

Figure III.7 demonstrates how different cutting parameters impact the cutting temperature in milling processes.

Analysis of Figure III.7 (a) reveals that reducing the feed per tooth results in higher cutting temperatures of 156 °C, and conversely, increasing the feed per tooth leads to lower temperatures 120 °C. This phenomenon might be attributed to the decreased time of contact between the tool and the workpiece when the feed per tooth is increased, thereby spreading the generated heat over a shorter duration and potentially lowering the cutting temperature. This is supported by the three curves shown in Figure III.8 which shows the distribution of heat during the cutting process according to real time for three tests with $V_c = 300$ *m/min* and $a_p = 0.5$ *mm* fixed and variable f_z, the cutting time decreases with the increase in the feed per tooth. Consequently, the heat generated has less chance of accumulating in the cutting area. With

reduced time to concentrate, the heat disperses more, thus avoiding excessive concentration at a single point. This dispersion over a shorter period can help to reduce the temperature measured in the cutting area.

Conversely, cutting speed seems to have no significant effect on the temperature of machined surfaces.

Analysis of Figure III.7 (b) indicate that the cutting temperature reaches its peak (153 $°C$) with the highest values of depth of cut and cutting speed (0.75 mm and 300 m/min respectively), while the lowest cutting temperatures (109 $°C$) correspond to the minimum values of these parameters (0.25 mm and 100 m/min respectively). Additionally, a greater depth of cut is associated with higher cutting temperatures on the machined surfaces.

According to Figure III.7 (c), it is apparent that the cutting temperature is at its highest (153.65 $°C$) with a depth of cut of 0.6 mm and minimum feed per tooth of 0.09 $mm/tooth$, whereas the lowest temperatures (119.4 $°C$) occur with a depth of cut of 0.4 mm and maximum feed per tooth of 0.18 $mm/tooth$.
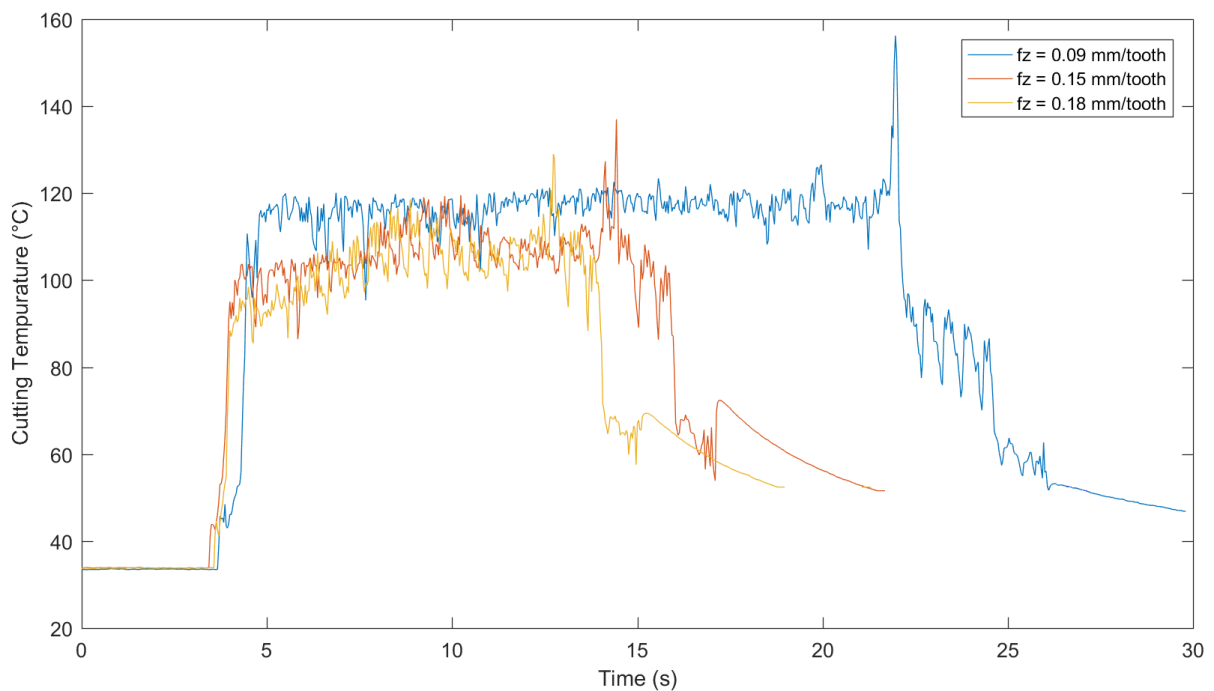
Figure III.8 *The distribution of heat during the cutting process according to real time for three tests with V_c = 300 m/min and a_p = 0.5 mm.*

b) Roughness

Figure III.9 displays the surfaces generated through the RSM, detailed as follows:

- Surface (a) shows the variation in surface roughness relative to V_c and f_z, at a constant a_p of 0.5 mm.

- Surface (b) shows the variation in surface roughness relative to V_c and a_p, at a constant f_z of 0.12 *mm/tooth*.

- Surface (c) shows the variation in surface roughness relative to a_p and f_z, at a constant V_c of 200 *m/min*.
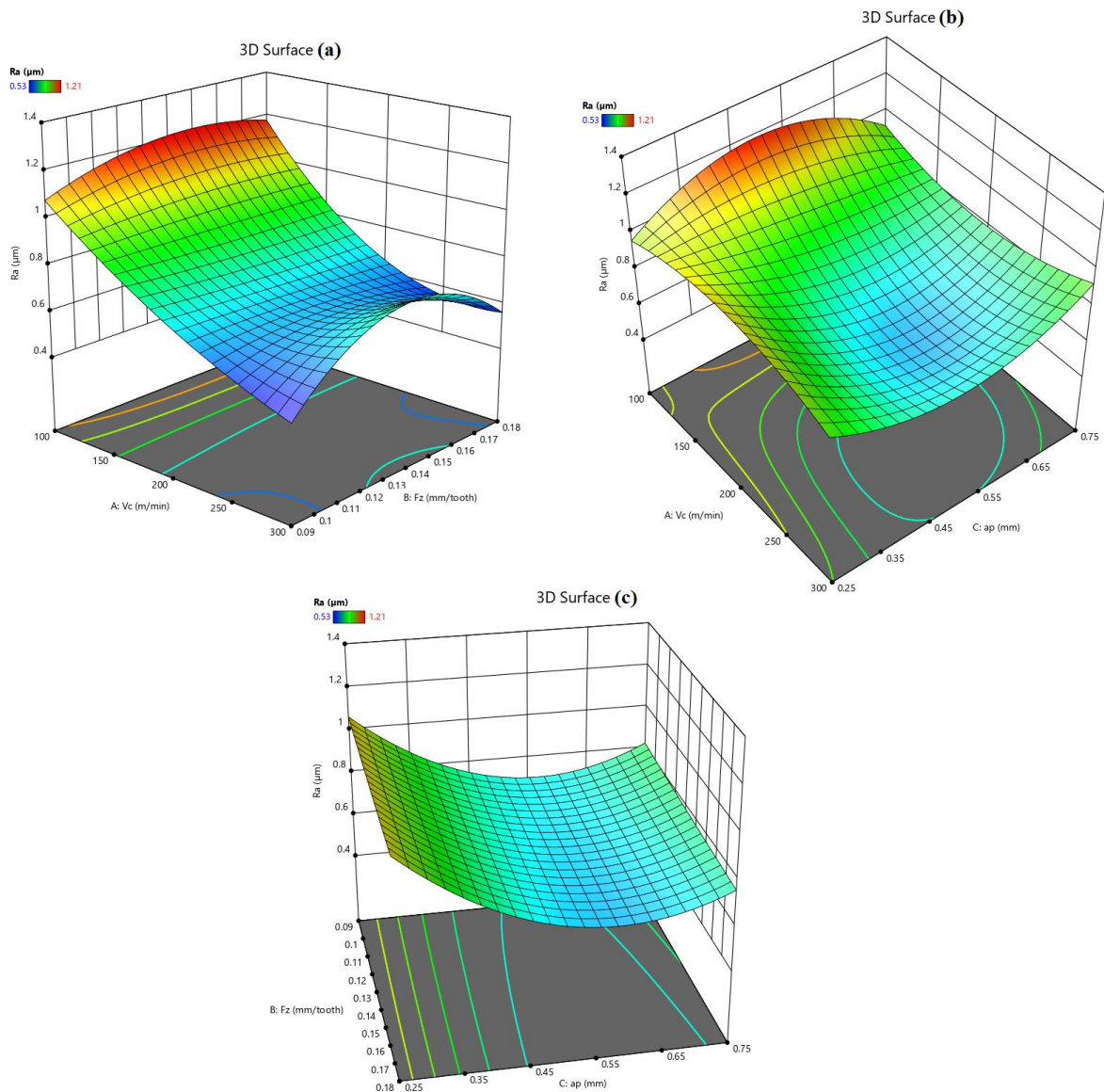
Figure III.9 *Variation of the predicted roughness as a function of the cutting parameters.*

Figure III.9 demonstrates how different cutting parameters impact the surface roughness in milling processes.

As shown in Figure III.9 (a), increased cutting speed correlate with reduced surface roughness, and conversely, slower cutting speeds increase surface roughness. the same Analyze is reported in [60], [61] and [62]. According to Oosthuizen et al. [61] this occurs because a

higher cutting speed results in a smaller plastic deformation cutting zone. Consequently, the surface defect is reduced, leading to a generally lower roughness value. And according to Muhammad et al. [58] The rationale behind this is that higher cutting speeds enhance material removal efficiency and prevent the tool from excessively penetrating the workpiece surface, thus minimizing surface irregularities.

On the other hand, the feed per tooth appears to have a negligible effect on surface roughness.

In Figure III.9 (b), the value of surface roughness peaks (1.21 μm) at low cutting speeds (100 m/min) and moderate depths of cut (0.5 mm), whereas the lowest value of surface roughness (0.65 μm) is achieved at a cutting speed of 250 m/min and a moderate depth of cut (0.5 mm).

The trend observed in Figure III.9 (c) demonstrates a consistent relationship between increasing the depth of cut and the reduction in surface roughness, corroborating findings documented in [60]. This observed phenomenon suggests that as the depth of cut increases, larger chips are formed during the machining process. These larger chips potentially serve as a protective layer or buffer between the tool and the workpiece surface. By acting as a shield, these larger chips can dampen direct tool contact with the workpiece surface, thus minimizing the occurrence of surface irregularities. This mechanism is believed to contribute to the observed trend of reduced surface roughness at higher depths of cut. However, the specific interactions between the tool, workpiece material, and chip formation processes warrant further investigation to validate this hypothesis.

On the other hand, the feed per tooth does not significantly impact the roughness of the machined surfaces.

c) Microhardness

Figure III.10 displays the surfaces generated through the RSM, detailed as follows:

- Surface (a) shows the variation in microhardness relative to V_c and f_z, at a constant a_p of 0.5 mm.
- Surface (b) shows the variation in microhardness relative to V_c and a_p, at a constant f_z of 0.135 $mm/tooth$.
- Surface (c) shows the variation in microhardness relative to a_p and f_z, at a constant V_c of 200 m/min.
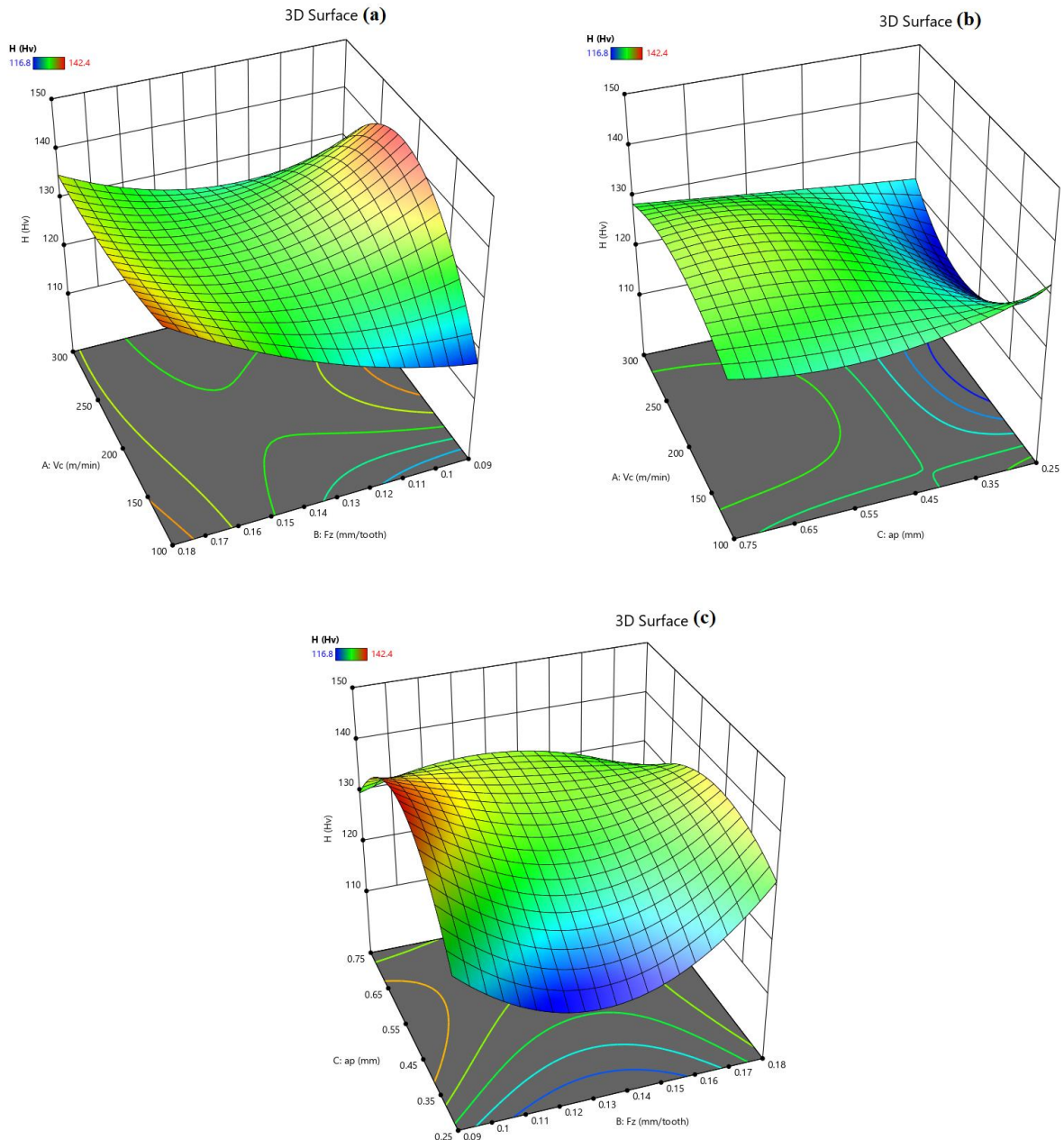
Figure III.10 *Variation of the predicted microhardness as a function of the cutting parameters.*

Figure III.10 demonstrates how different cutting parameters impact the surface microhardness in milling processes.

As depicted in Figure III.10 (a), the highest microhardness values (142 H_v) are achieved at the lowest feed per tooth values (0.09 *mm/tooth*) and moderate cutting speed (200 *m/min*), while the lowest microhardness values (117 H_v) correspond to minimal feed per tooth and cutting speed values (0.09 *mm/tooth* and 100 *m/min* respectively).

Figure III.10 (b) shows that an increase in the depth of cut is associated with higher microhardness values, and the opposite is true as well, the same analyze is reported by Lu et al.

[38], and according to their findings, this phenomenon is attributed to the expanded area of the cutting layer caused by the axial cutting depth, which leads to an increase in cutting force. Consequently, this heightened force results in more significant plastic deformation

The observed trends in Figure III.10 (c) can be elucidated through mechanistic insights into the plowing effect and subsequent work hardening. At lower feed rates, the machining process predominantly experiences the plowing effect, where the cutting tool displaces and pushes the material along the machined surface. This phenomenon induces substantial material extrusion and friction, resulting in localized deformation and increased dislocation density within the material.

Visualizing this effect, imagine the cutting tool's action akin to a plow moving through soil. At slower feed rates, the tool tends to 'plow' through the material, causing significant displacement and deformation along the machined path. This action intensifies the material's work hardening, effectively increasing its microhardness.

Conversely, as the feed speed increases, the plowing force becomes more pronounced, leading to a greater degree of material displacement and subsequent work hardening. This intensified plowing action results in an elevation of microhardness values observed in Figure III.10 (c).

III.5. Multi-objective optimization

III.5.1. Genetic algorithm

The genetic algorithm is a form of optimization method influenced by Darwin's theory of natural selection and evolutionary processes in biology, the survival of the fittest. The goal of a GA is to identify the optimal solution to a particular problem. by repeatedly generating new candidate solutions, testing them, and selecting the best ones for further improvement.

At a high level, genetic algorithm begins by creating an initial population consisting of potential solutions to a given problem. Every solution is presented as a combination of parameters or genes. The algorithm then evaluates each solution by calculating its fitness score, which is a measure of how well it solves the problem.

The algorithm then uses the fitness scores to select the best solutions from the population, and generates new solutions by applying various genetic operators like mutation, crossover, and selection. Mutation includes the random alteration of the values of one gene or more within a solution, whereas crossover includes merging the genes of two solutions to produce a novel

one. Selection involves choosing the best solutions from the population based on their fitness scores.

This process is repeated over a number of generations, with the hope that the population will converge towards the best solution to the problem. Genetic algorithms can be applied to a vast variety of optimization problems including engineering, financial forecasting, and machine learning.

III.5.2. Multi-objective optimization using genetic algorithm

The optimization of one target will result in the degradation of other targets, this why multi-objective optimization using GA will be employed in order to get the optimal cutting parameters for establishing two objectives, the first objective is minimizing the production time per unit (Maximizing production rate) and the second objective is minimizing the production cost per unit, and those two objectives will be achieved respecting some specified machining constraints: tool life, surface roughness, microhardness, cutting force, cutting power, and a specific range of cutting parameters.

a) Objective functions

- **Minimizing the production cycle time per unit**

the production cycle time per piece is given [1]:

$$T_c = T_h + T_m + \frac{T_t}{n_p} \tag{III.6}$$

For face milling machining time is given:

$$T_m = \frac{0.5 \times D + L}{S \times f_z \times Z} \tag{III.7}$$

Tool life equation is given:

$$T = \frac{C^{\frac{1}{n}}}{V_c^{\frac{1}{n}}} \tag{III.8}$$

The number of pieces cut in one tool life is given:

$$n_p = \frac{T}{T_m} \tag{III.9}$$

$$n_p = \frac{C^{\frac{1}{n}} \times 1000 \times Z \times f_z}{\pi \times D \times V^{\frac{1}{n}-1} \times (0.5 \times D + L)} \tag{III.10}$$

So, the final expression for the total production cycle time per unit in the face milling is given as follows:

$$T_c = T_h + \frac{\pi \times D \times (0.5 \times D + L)}{1000 \times Z \times f_z \times V_c} + \frac{T_t \times \pi \times D \times (0.5 \times D + L) \times V_c^{\frac{1}{n}-1}}{1000 \times Z \times f_z \times C^{\frac{1}{n}}}$$

(III.11)

- **Minimizing cost per unit**

the total cost per unit in face milling is given [1]:

$$C_c = C_h + C_m + C_{th} + C_{tc}$$

(III.12)

$$C_c = C_0 \times T_h + C_0 \times T_m + C_0 \times \frac{T_t}{n_p} + \frac{C_t}{n_p}$$

(III.13)

Tool cost is given:

$$C_t = \frac{P_t}{n_e}$$

(III.14)

So, the final expression for the total cost per unit in the face milling is given as follows:

$$C_c = \left(\begin{array}{l} C_0 \times T_h + C_0 \times \dfrac{\pi \times D \times (0.5 \times D + L)}{1000 \times Z \times f_z \times V_c} \\[4mm] + C_0 \times \dfrac{T_t \times \pi \times D \times (0.5 \times D + L) \times V_c^{\frac{1}{n}-1}}{1000 \times Z \times f_z \times C^{\frac{1}{n}}} \\[4mm] + \dfrac{P_t \times \pi \times D \times (0.5 \times D + L) \times V_c^{\frac{1}{n}-1}}{n_e \times 1000 \times Z \times f_z \times C^{\frac{1}{n}}} \end{array} \right)$$

(III.15)

b) Constraints

This study will examine the various limitations that influence the determination of optimal cutting parameters. It is crucial to address these constraints as the utilization of inappropriate milling parameters can result in undesirable outcomes such as poor surface roughness and microhardness, reduced machining efficiency, and increased cutting force.

- **Parameter bounds**

Cutting speed:

$$V_{c_{min}} \leq V_c \leq V_{c_{max}}$$

(III.16)

Feed per tooth:

$$f_{z_{min}} \leq f_z \leq f_{z_{max}}$$

(III.17)

Axial depth of cut:

$$a_{p_{\min}} \le a_p \le a_{p_{\max}} \tag{III.18}$$

- **Tool-life constraint**

$$T_{\min} \le T \le T_{\max} \tag{III.19}$$

- **Cutting force constraint**

In order to avoid undesired shaking and vibration during the machining, the highest cutting force possible must not exceed a specific limit, This constraint in face milling is given [63]:

$$F_c = \frac{C_F \times a_p{}^{x_F} \times f_z{}^{y_F} \times a_e{}^{t_F} \times Z^{p_F} \times k_F}{D^{q_F} \times n_S{}^{w_F}} \le F_u \tag{III.20}$$

- **Power constraint**

For face milling the power constraint is given:

$$P_c = \frac{F_c \times V_c}{60} \tag{III.21}$$

$$P_m = \frac{P_c}{\eta} \tag{III.22}$$

$$P_m = \frac{C_F \times a_p{}^{x_F} \times f_z{}^{y_F} \times a_e{}^{t_F} \times Z^{p_F} \times k_F \times V_c}{D^{q_F} \times n_S{}^{w_F} \times 60 \times \eta} \le P_u \tag{III.23}$$

- **Surface roughness and microhardness constraints**

In the milling processes, the resulting surface roughness and microhardness should not exceed a specified values given by technological criteria, this why Surface roughness and microhardness will be considered as constraints.

Surface roughness constraint:

$$R_a = \begin{pmatrix} 11.94131 - 0.127737 \times V_c - 89.07276 \times f_z \\ - 21.86460 \times a_p + 1.09198 \times V_c \times f_z + 0.232765 \\ \times V_c \times a_p - 7.79114 \times f_z \times a_p + 0.000341 \times V_c^2 \\ + 316.51250 \times f_z^2 + 21.22230 \times a_p^2 + 0.052911 \\ \times V_c \times f_z \times a_p - 0.003299 \times V_c^2 \times f_z - 0.000478 \\ \times V_c^2 \times a_p - 3.82465 \times V_c \times f_z - 0.216064 \times V_c \times a_p^2 \\ + 0.011377 \times V_c^2 \times f_z^2 + 0.000417 \times V_c^2 \times a_p^2 \end{pmatrix}^{-1} \le R_{as} \tag{III.24}$$

Surface microhardness constraint:

$$H = \begin{pmatrix} -327.467 + 4.506 \times V_c + 12213.6 \times f_z - 564.4 \times a_p \\ -124.096 \times V_c \times f_z + 9.76 \times V_c \times a_p - 15845.2 \times f_z \\ \times a_p - 0.01079 \times V_c^2 - 55535 \times f_z^2 + 1920 \times a_p^2 \\ +105.367 \times V_c \times f_z \times a_p + 0.286296 \times V_c^2 \times f_z \\ -0.0194 \times V_c^2 \times a_p + 556.42 \times V_c \times f_z^2 - 24.608 \\ \times V_c \times a_p^2 + 112123 \times f_z^2 \times a_p - 7054.81 \times f_z \times a_p^2 \\ -1.25864 \times V_c^2 \times f_z^2 - 0.272333 \times V_c^2 \times f_z \times a_p \\ +0.05224 \times V_c^2 \times a_p^2 - 898.889 \times V_c \times f_z^2 \times a_p \\ +146.089 \times V_c \times f_z \times a_p^2 - 23901.2 \times f_z^2 \times a_p^2 \\ +2.1 \times V_c^2 \times f_z^2 \times a_p - 0.281333 \times V_c^2 \times f_z \times a_p^2 \\ -63.7037 \times V_c \times f_z^2 \times a_p^2 \end{pmatrix} \leq H_s \qquad (III.25)$$

c) The optimization problem

The optimization problem for this case can be stated as follow:

$$\begin{cases} Min\, T_c \\ Min\, C_c \\ With: \\ V_{c_{min}} \leq V_c \leq V_{c_{max}} \\ f_{z_{min}} \leq f_z \leq f_{z_{max}} \\ a_{p_{min}} \leq a_p \leq a_{p_{max}} \\ T_{min} \leq T \leq T_{max} \\ F_c \leq F_u \\ P_m \leq P_u \\ R_a \leq R_{as} \\ H \leq H_s \end{cases} \qquad (III.26)$$

Table III.7 shows the numerical data considered for this experiment. While Table III.8 shows the constants for the cutting force formula taken from the work of Nefedov and Osipov [63].

Table III.7 The numerical data considered for this experiment.

Parameter	Value	Parameter	Value	Parameter	Value
$V_{c_{min}}$ (m/min)	100	L (mm)	250	C_0 (Euro/min)	0.66
$V_{c_{max}}$ (m/min)	300	Z (tooth)	5	P_t (Euro)	16.80
$f_{z_{min}}$ (mm/tooth)	0.09	C	500	n_e	4
$f_{z_{max}}$ (mm/tooth)	0.18	n	0.25	R_{as} (μm)	0.8
$a_{p_{min}}$ (mm)	0.25	T_{min} (min)	8	F_u (N)	8000
$a_{p_{max}}$ (mm)	0.75	T_{max} (min)	600	P_u (W)	9000
a_e (mm)	50	T_h (min)	1.5	η	0.75
D (mm)	50	T_t (min)	3	H_s (Hv)	130

Table III.8 Constants for the cutting force formula.

Constant	Value	Constant	Value	Constant	Value
C_F	534.6	x_F	0.9	y_F	1.74
t_F	1	k_F	1	q_F	1
p_F	1	w_F	0	n_s	-

d) MoGA setting

The multi-objective genetic algorithm has been run in MATLAB R2016b using the solver gamultiobj in the optimtool toolbox. The initial parameter setting for this algorithm is shown in Table III.9.

Table III.9 Parameters used in the genetic algorithm.

Parameter	Value or type
Population size	50
Selection function	Tournament
Crossover fraction	0.8
Function tolerance	1e-5
Mutation	Constraint dependent
Crossover	Intermediate, Ratio: 1.0
Migration fraction	0.2
Migration interval	20
Number maximal of iterations	1500

e) The results of the multi-objective genetic algorithm

Sometimes there is a lack of agreement between the evaluation criteria's because they often conflict with one another. As a result, multiple optimal solutions are sought rather than just a single solution of combination of input parameters. The Pareto front illustrates the values of functions for all feasible solutions regarding production cycle time and cost per unit, as depicted in Figure III.11.
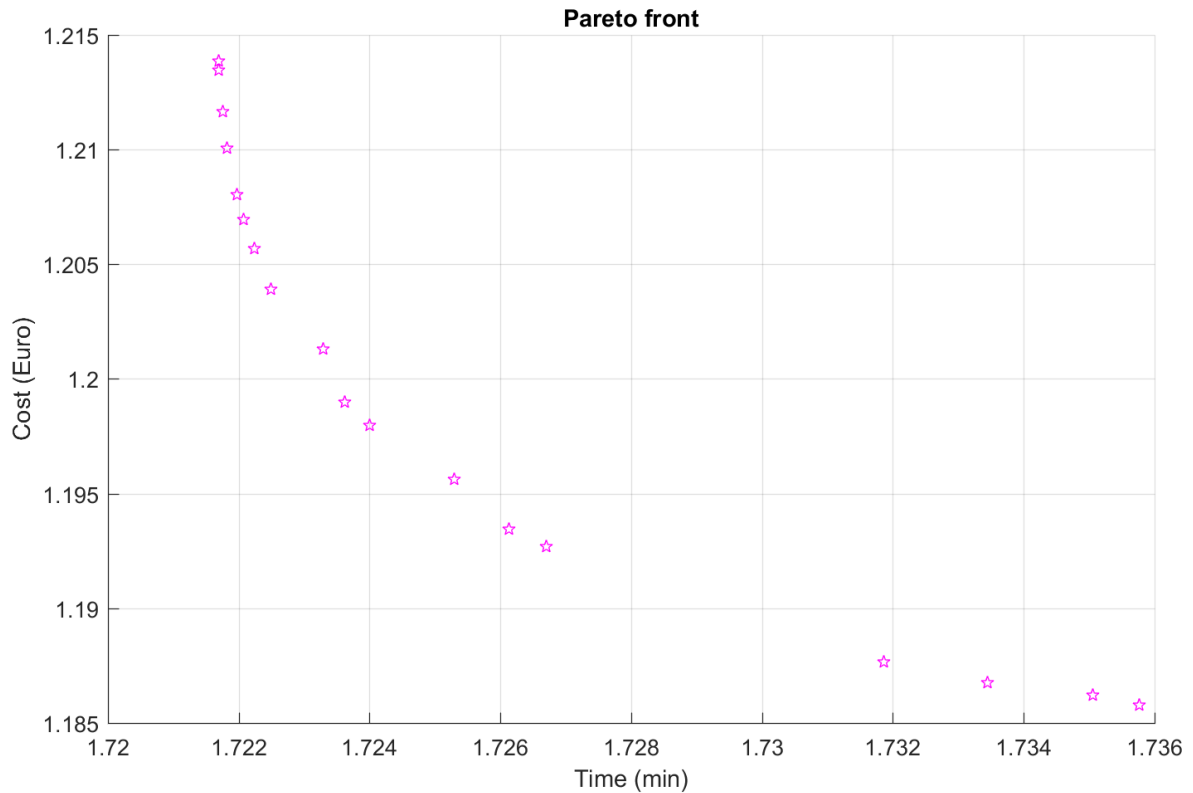
Figure III.11 *Pareto-front.*

Eighteen solutions found by the multi-objective genetic algorithm as shown in Table III.10.

Table III.10 Pareto-optimal solutions.

Index	Time (*min*)	Cost (*Euro*)	V_c (*m/min*)	f_z (*mm/tooth*)	a_p (*mm*)
1	1.7217	1.2139	288.62	0.180	0.702
2	1.7267	1.1927	254.29	0.179	0.709
3	1.7240	1.1980	265.11	0.180	0.708
4	1.7222	1.2057	277.56	0.180	0.702
5	1.7220	1.2080	280.94	0.180	0.701
6	1.7233	1.2013	270.51	0.179	0.701
7	1.7253	1.1956	260.25	0.179	0.706
8	1.7334	1.1867	236.49	0.180	0.712
9	1.7221	1.2070	279.44	0.180	0.702
10	1.7225	1.2039	274.94	0.180	0.703
11	1.7217	1.2135	288.14	0.180	0.702
12	1.7218	1.2117	285.77	0.180	0.702
13	1.7261	1.1934	256.12	0.180	0.712
14	1.7351	1.1862	233.50	0.179	0.714
15	1.7236	1.1990	267.01	0.180	0.714
16	1.7358	1.1858	231.78	0.180	0.714
17	1.7218	1.2101	283.69	0.180	0.706
18	1.7319	1.1876	240.04	0.180	0.711

From Table III.10 it's noticed that the highest value of production cycle time per unit T_c is 1.7358 *min* and the lowest value is 1.7217 *min* the difference is just 0.0141 *min*, and it's noticed also the highest cost per unit C_c is 1.2139 *Euro* and the lowest value is 1.1858 *Euro*, the difference is only 0.0281 *Euro*. It's concluded that all of the 18 solutions are very close. It's noticed also, that the all solutions are generated for high values of V_c, f_z and a_p. To choose among the 18 solutions, it depends on which objective is more important. If minimizing the production cycle time is the priority, then the best solution is number 11 (T_c = 1.7217 *min* and C_c = 1.2135 *Euro* for V_c = 288.14 *m/min*, f_z = 0.18 *mm/tooth* and a_p = 0.702 *mm*). Conversely, if the goal is to minimize the cost per unit, then the best solution is number 16 (T_c = 1.7358 *min* and C_c = 1.1858 *Euro* for V_c = 231.78 *m/min*, f_z = 0.18 *mm/tooth* and a_p = 0.714 *mm*). If there is no specific preference for either objective, the optimal solution would be the one that minimizes the values of both objectives, given equal weighting to each. In this case, solution number 2 (T_c = 1.7267 *min* and C_c = 1.1927 *Euro* for V_c = 254.29 *m/min*, f_z = 0.179 *mm/tooth* and a_p = 0.709 *mm*) would be optimal, as this pair has the lowest combined sum.

III.6. Conclusion

In this chapter, an analysis was performed to explore the impact of cutting parameters on the cutting temperature, surface roughness and microhardness of milled AISI 1060. The RSM was applied to assess and predict the effects of these parameters on cutting temperature, surface roughness and microhardness. Additionally, multi-objective optimization through genetic algorithms was employed to identify the best combination of cutting parameters that would reduce both production time and cost per unit by considering the R_a and H based-RSM models as constraints in defining the optimization problem instead of using the general empirical models documented in the handbooks to get a better precision and control of the specific R_a and H while satisfying other machining constraints (tool life, cutting force, cutting power).

CHAPTER IV

Simulation of Surface Defects

after Milling

IV.1. Introduction

To comprehensively understand the influence of surface integrity on the fatigue life of mechanical components, in this chapter the advanced simulation capabilities of ANSYS will be used to compare a workpiece presumed to have been milled under two distinct cutting conditions. In the first scenario, the workpiece is assumed to exhibit no surface defects, whereas in the second scenario, it is hypothesized to contain a semi-elliptical crack on one of its surfaces, presumably resulting from a technical error during the face milling operation. The semi-elliptical shape of the crack is chosen for its relevance in representing typical surface flaws that can significantly impact the structural integrity and longevity of engineering materials. The comparison involves simulating pressure loading on workpiece.

Through the analysis of total deformation, equivalent elastic strain, and equivalent (von Mises) stress of the workpiece in both scenarios, this study aims to uncover critical factors that influence fatigue life. This investigation will not only enhance the understanding of the role of surface defects in fatigue failure but also contribute to the formulation of more efficacious strategies for refining manufacturing processes and designing components with superior durability.

IV.2. Solid Modelling

The initial phase involves modeling the material properties and solid geometric configuration utilizing the Design Modeler within the Static Structural module of ANSYS Workbench 2020 R1. The dimensions of the prismatic workpiece modeled are as follows: a length of 40 mm, a width of 20 mm, and a thickness of 15 mm. These dimensions are depicted in Figure IV.1.
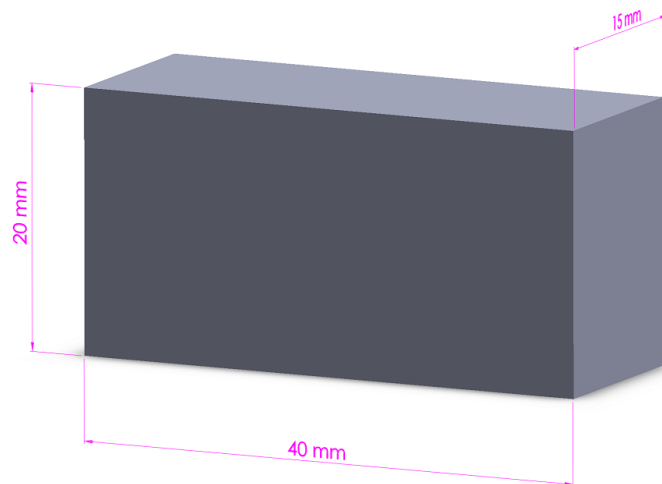
Figure IV.1 Geometry of the workpiece.

The material of the workpiece is AISI 1060 carbon steel, the properties used to define it in ANSYS is described in Table IV.1.

Table IV.1 The properties used to define the AISI 1060 carbon steel in ANSYS.

Properties	Value
Density	7.85 g/cm^3
Ultimate strength	620 MPa
Yield strength	485 MPa
Young's modulus	200 GPa
Bulk modulus	166 GPa
Shear modulus	77 GPa
Poisson's ratio	0.30

IV.3. Meshing

After modeling the workpiece, it is imperative to apply a meshing technique, specifically setting the mesh type to 'Tetrahedrons'. By default, the software selects the Patch Conforming algorithm, and the element order is configured to be quadratic. Figure IV.2 illustrates the initial mesh generated for the workpiece in the first scenario using Ansys Workbench, characterized by an element size of 1 mm. This configuration results in the creation of 143725 nodes and 102063 elements.
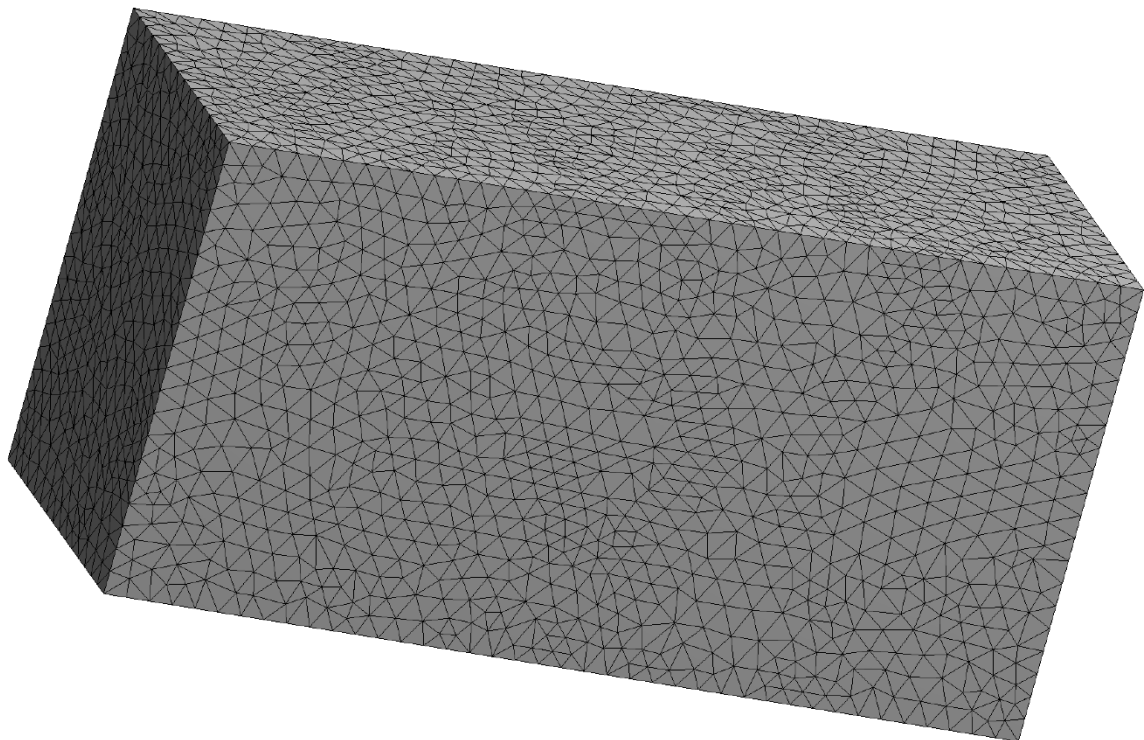
Figure IV.2. The initial meshes of the crack-free workpiece in ANSYS workbench.

IV.4. Semi-Elliptical Crack

The subsequent phase involves defining the initial crack for the second scenario.

IV.4.1. Semi-Elliptical Crack geometry

Figure IV.3 illustrates the primary configuration parameters employed by ANSYS within the fracture module for modeling a semi-elliptical crack.
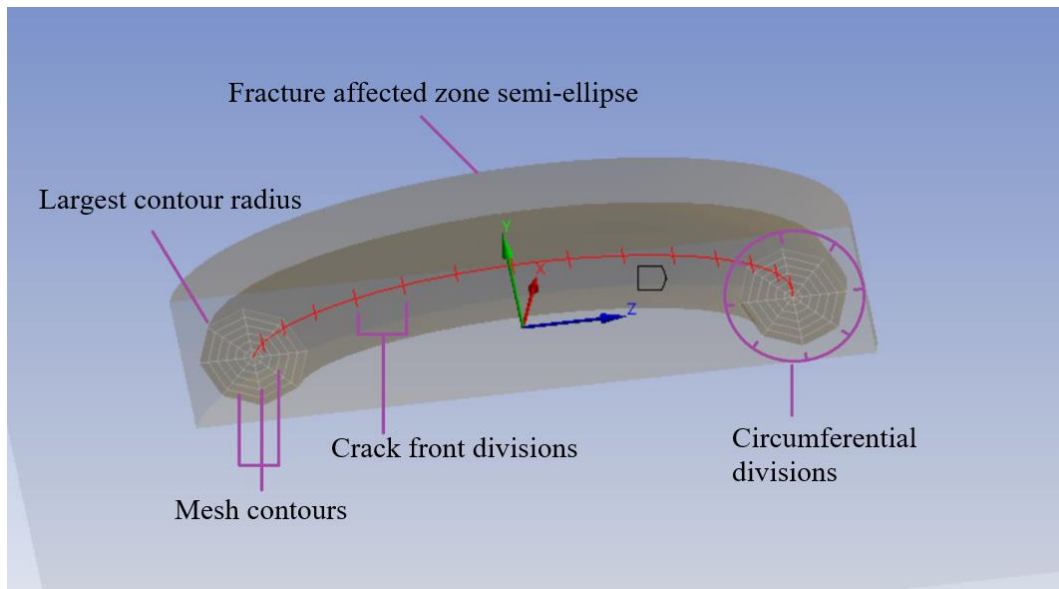
Figure IV.3. *The different configuration parameters of semi-elliptical crack*

- **Major Radius**: This parameter defines the major radius, indicating the extent of the crack's shape along the Z-axis, essentially determining the crack's width (c).
- **Minor Radius:** This parameter defines the minor radius, indicating the extent of the crack's shape along the X-axis, essentially determining the crack's depth (a).
- **Mesh Method**: This parameter allows for the selection of the desired meshing method for applying to the semi-elliptical crack, with available options being Hex Dominant (the default choice) and Tetrahedrons meshes.
- **Largest Contour Radius**: This sets the maximum contour radius of the crack's geometry.
- **Crack Front Divisions:** This denotes the segmentation count along the crack front.
- **Fracture Affected Zone:** This zone encompasses the area affected by the crack. The setting for the zone Influenced by the fracture determines the method for defining the height of the affected zone:

✓ Program Controlled: The software computes the height, making the Zone Influenced by Fracture Height a read-only parameter. This setting is the default.

✓ Manual: The height is manually inputted into the Zone Influenced by Fracture Height parameter.

- **Fracture Affected Zone Height:** This value represents two aspects:

✓ The height of the Zone Affected by the fracture, aligned with the Y-axis of the crack's coordinate system.

✓ the total extension of the Zone Influenced by the fracture in both the positive and negative directions along the Z-axis of the crack's coordinate system, starting from the crack front's edges.

- **Circumferential Divisions:** Indicates the count of divisions around the circumference for the of the crack's shape.

IV.4.2. Semi-Elliptical Crack Modelling

For the second scenario in the prismatic workpiece under consideration, an initial semi-elliptical crack will be inserted using the fracture tool. The position of this crack is located at the center of the surface, which is presumed to have been milled. Table IV.2 presents the properties configuration of the initial semi-elliptical crack. The crack extends in the width direction, possessing a length of 1 mm, as depicted in Figure IV.4.

Table IV.2 The properties configuration for the semi-elliptical crack.

Properties	Configuration
Crack Shape	Semi-elliptical crack
Major Radius	0.5 *mm*
Minor Radius	0.25 *mm*
Mesh Method	Tetrahedrons
Largest Contour Radius	0.2 *mm*
Growth Rate	Default (1.20)
Front Element Size	Default
Mesh Contours	6
Solution Contours	6
Crack Face Nodes	On

After the generation of the crack meshes, the total number of nodes will increase to 201428, and the total number of elements will increase to 143 752 compared to the first scenario. Figure IV.5 illustrates the newly generated mesh for the workpiece following the definition of the semi-elliptical crack.
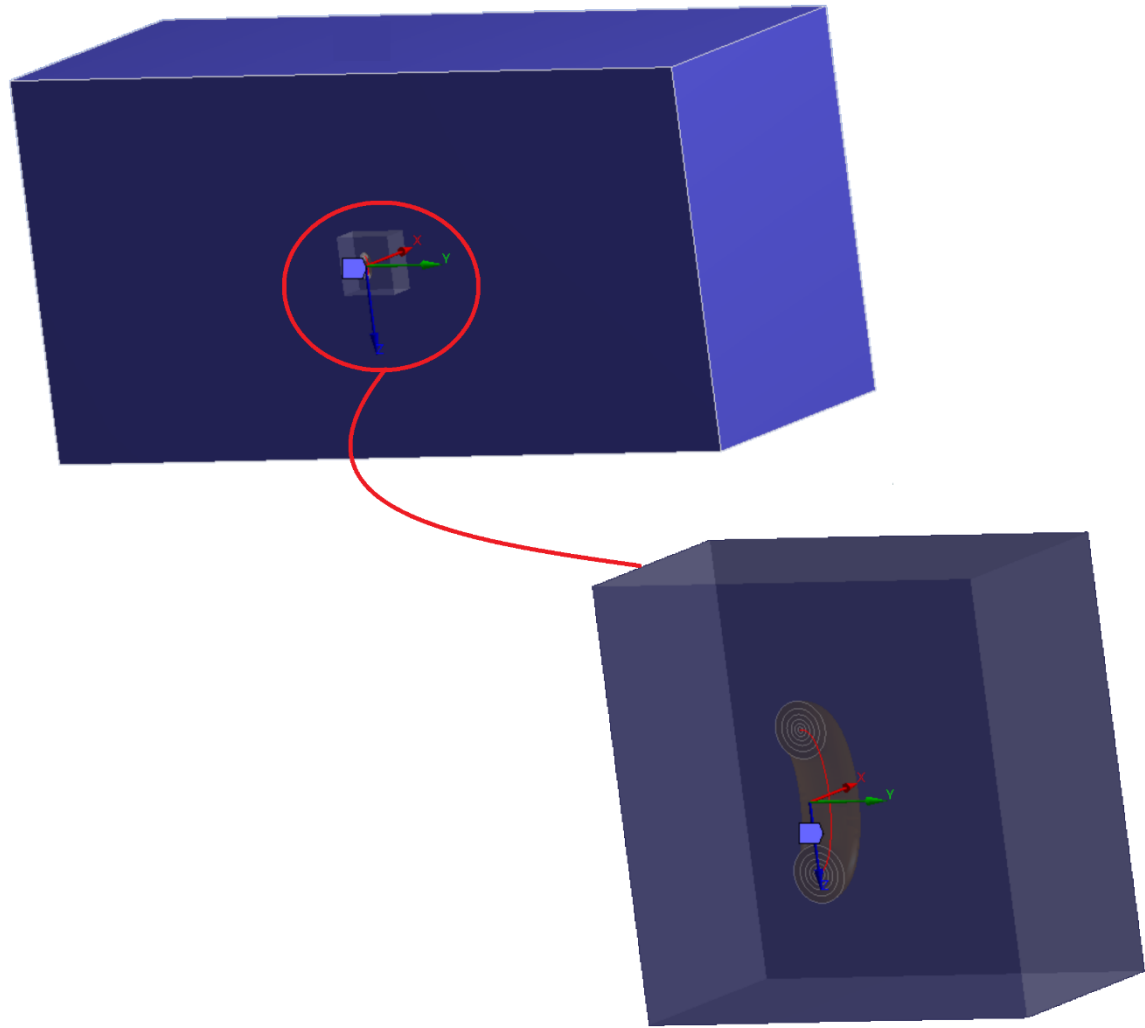
Figure IV.4. *The initial modeled semi-elliptical crack.*

IV.5. Boundary condition and pressure loading

The boundary conditions for the specimen were established by securing the left face of the specimen with a fixed support and subjecting the right face to a pressure load. Specifically, a pressure of -35 MPa was applied, as illustrated in Figure IV.6.

IV.6. Analysis settings

In the context of ANSYS Static Structural, Analysis Settings refer to a collection of parameters and options that define how the simulation is conducted. These settings influence the accuracy, convergence, and computational requirements of the analysis. Table IV.3 show the configuration of the analysis setting for the step controls in ANSYS.
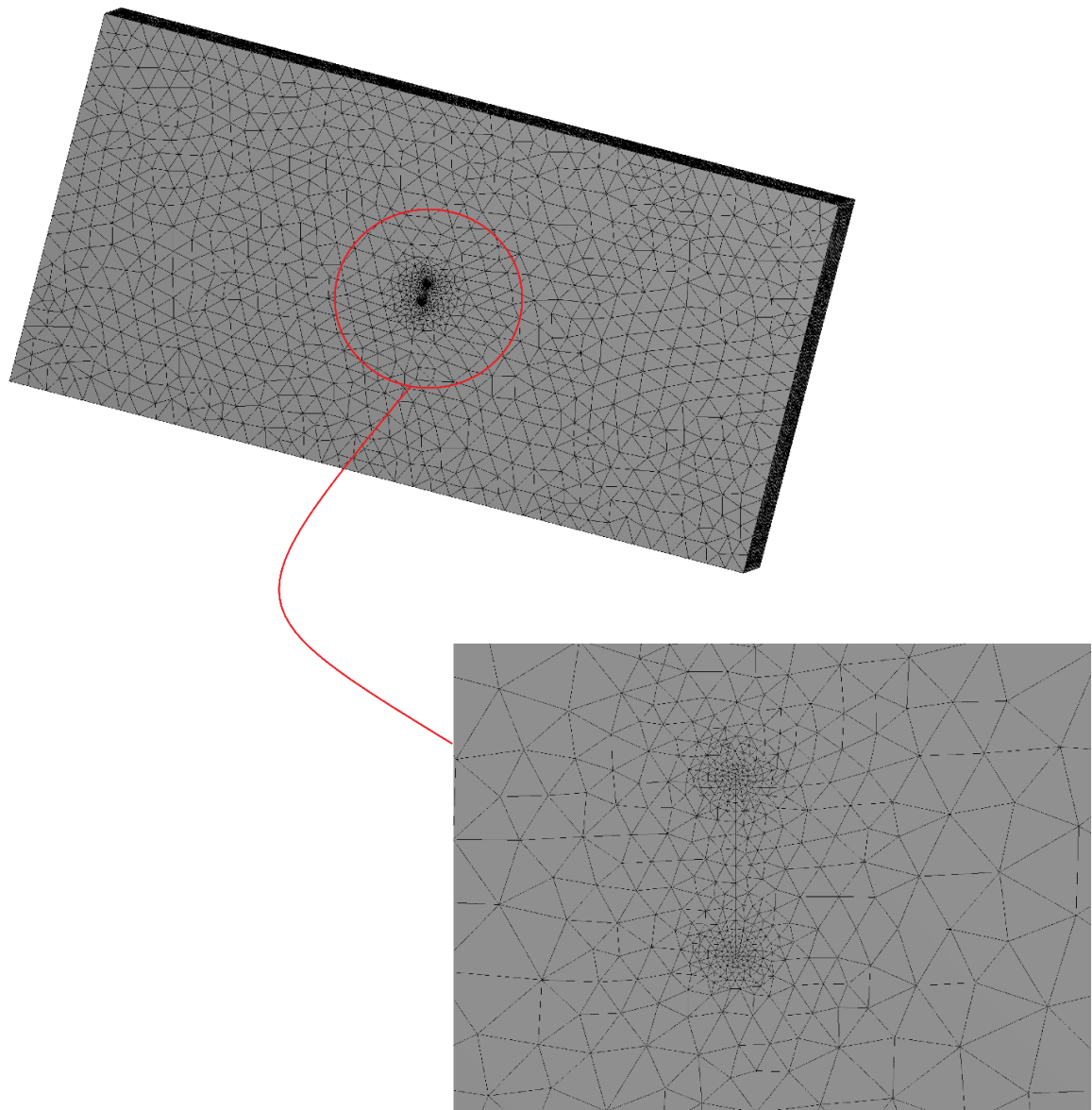
Figure IV.5. *The new generated mesh after the definition of the semi-elliptical crack.*

A Pressure: - 35 MPa
B Fixed Support
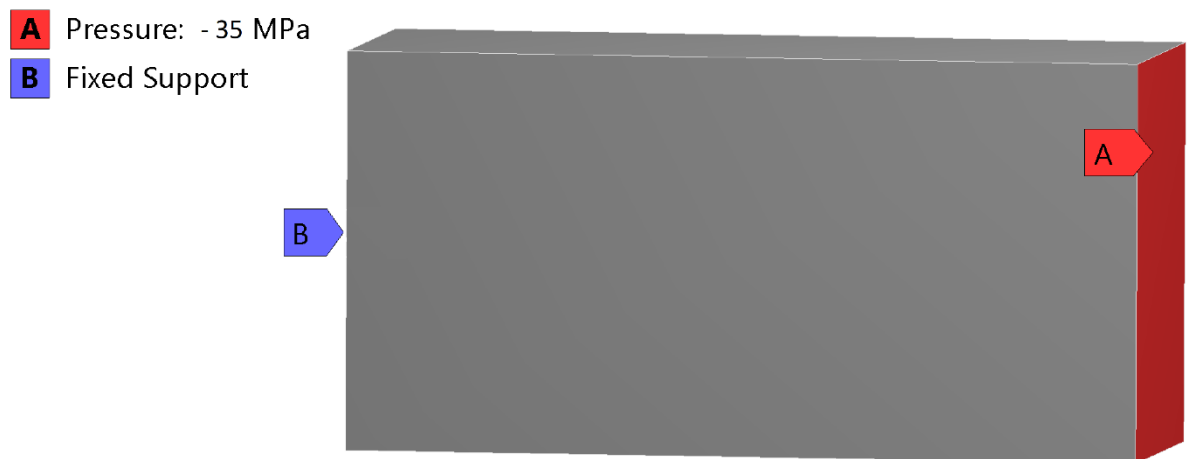
Figure IV.6. *The boundary conditions and pressure loading.*

Table IV.3 The configuration of the analysis setting for the step controls.

Parameters	Configuration
Number of Steps	1
Current Step Number	1
Step End Time	1 s
Auto time Stepping	Off
Define By	Sub-Steps
Number of Sub-Steps	5

IV.7. The results

IV.7.1. The workpiece without the semi elliptical crack

Figure IV.7 show the total deformation for the workpiece without the semi elliptical crack before the pressure loading is applied.
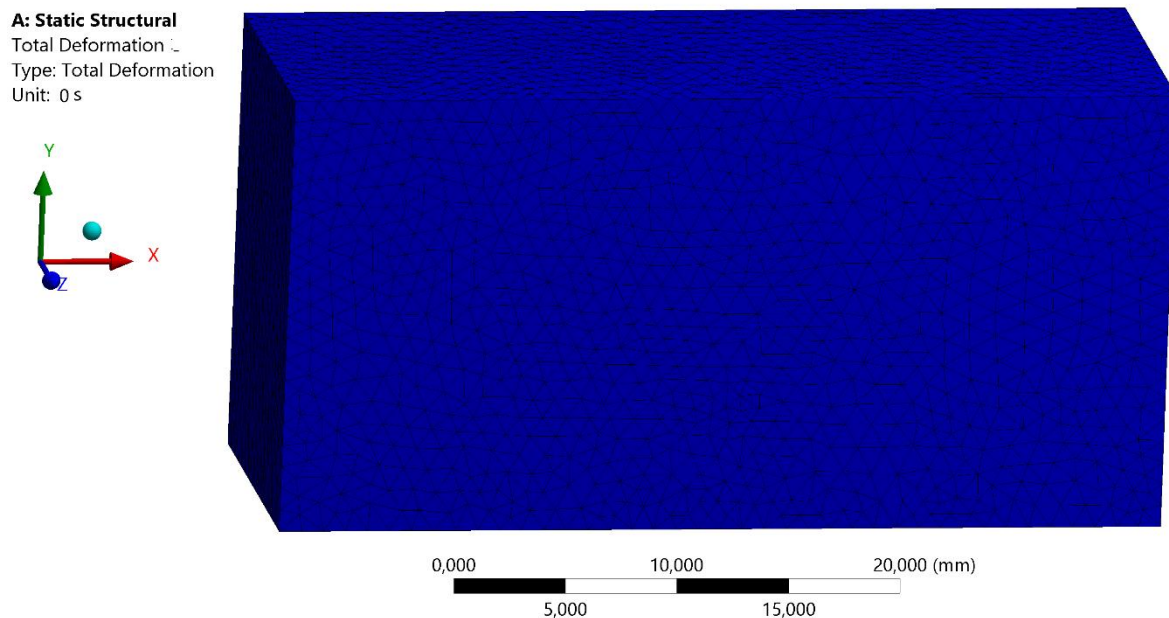
Figure IV.7. *The total deformation for the workpiece without the semi elliptical crack before the pressure loading is applied.*

Figure IV.8 show the total deformation for the workpiece without the semi elliptical crack after the pressure loading is applied.

Figure IV.9 show the equivalent elastic strain for the workpiece without the semi elliptical crack before the pressure loading is applied.

Figure IV.10 show the equivalent elastic strain for the workpiece without the semi elliptical crack after the pressure loading is applied.

A: Static Structural
Total Deformation
Type: Total Deformation
Unit: mm
Time: 1 s

0,0069399 Max
0,0061688
0,0053977
0,0046266
0,0038555
0,0030844
0,0023133
0,0015422
0,0007711
0 Min
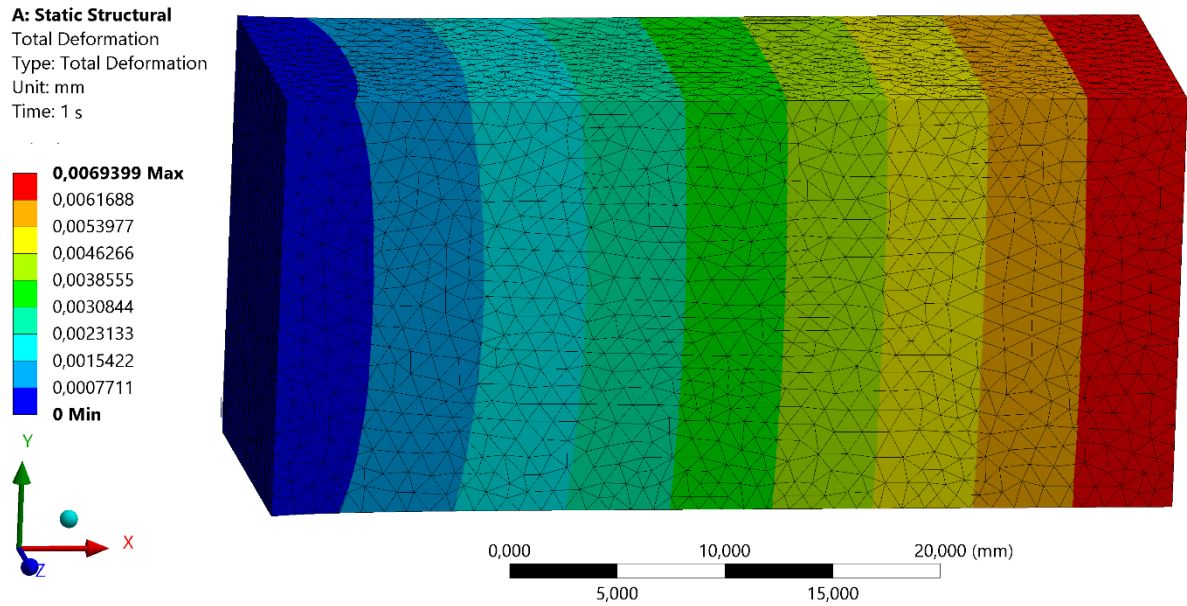
Figure IV.8. *The total deformation for the workpiece without the semi elliptical crack after the pressure loading is applied.*

A: Static Structural
Equivalent Elastic Strain
Type: Equivalent Elastic Strain
Unit: 0 s
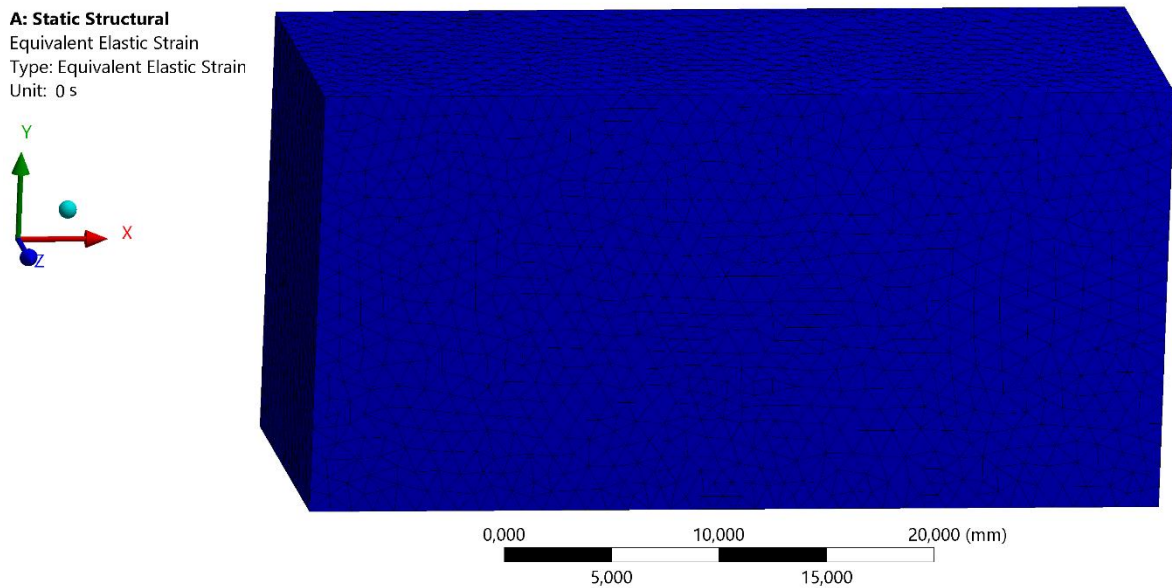
Figure IV.9. *The equivalent elastic strain for the workpiece without the semi elliptical crack before the pressure loading is applied.*

Figure IV.11 show the equivalent (von-Mises) stress for the workpiece without the semi elliptical crack before the pressure loading is applied.

Figure IV.12 show the equivalent (von-Mises) stress for the workpiece without the semi elliptical crack after the pressure loading is applied.

A: Static Structural
Equivalent Elastic Strain
Type: Equivalent Elastic Strain
Unit: mm/mm
Time: 1 s

0,00040112 Max
0,0003662
0,00033128
0,00029636
0,00026144
0,00022652
0,0001916
0,00015668
0,00012176
8,6844e-5 Min
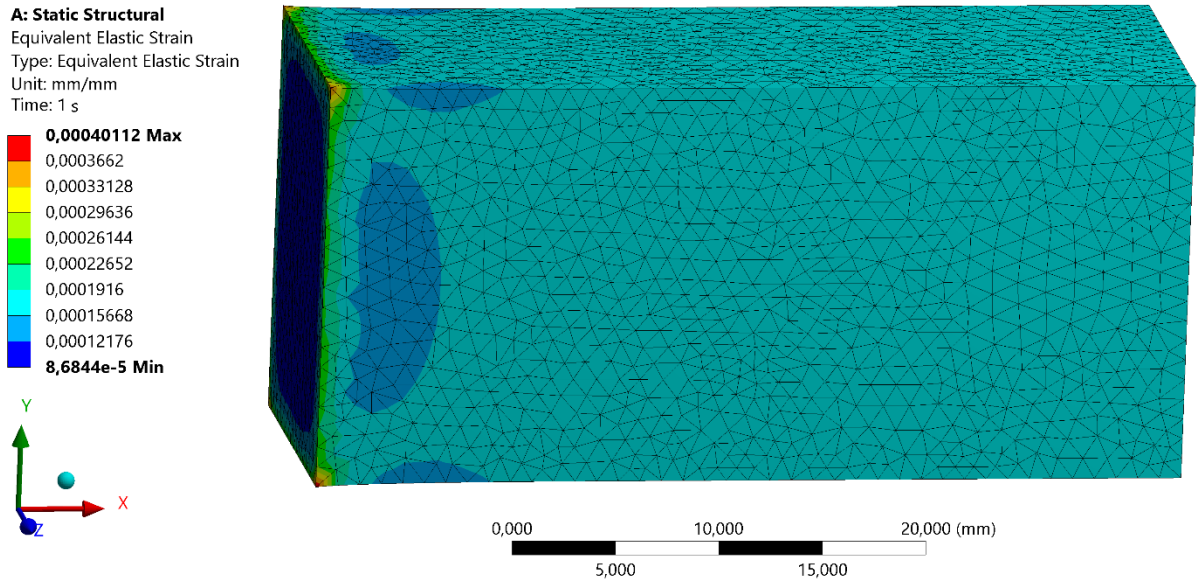
Figure IV.10. *The equivalent elastic strain for the workpiece without the semi elliptical crack after the pressure loading is applied.*

A: Static Structural
Equivalent Stress 2
Type: Equivalent (von-Mises) Stress
Unit: 0 s
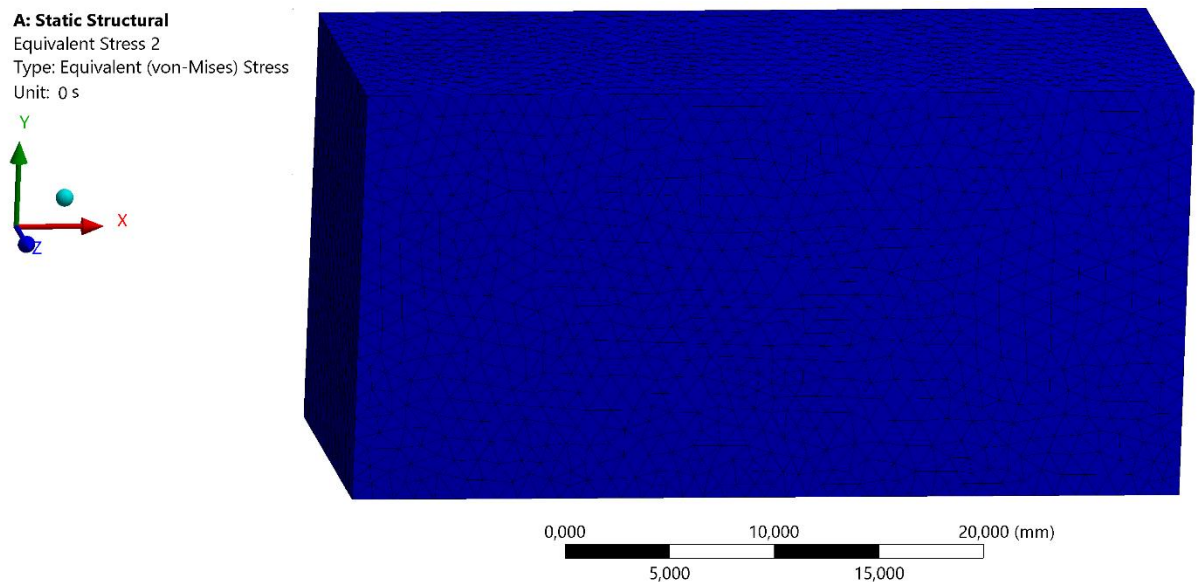
Figure IV.11. *The equivalent (von-Mises) stress for the workpiece without the semi elliptical crack before the pressure loading is applied.*

IV.7.2. The workpiece with the semi elliptical crack

Figure IV.13 show the total deformation for the workpiece with the semi elliptical crack before the pressure loading is applied.

A: Static Structural
Equivalent Stress
Type: Equivalent (von-Mises) Stress
Unit: MPa
Time: 1 s

78,768 Max
71,944
65,121
58,297
51,473
44,649
37,825
31,001
24,178
17,354 Min
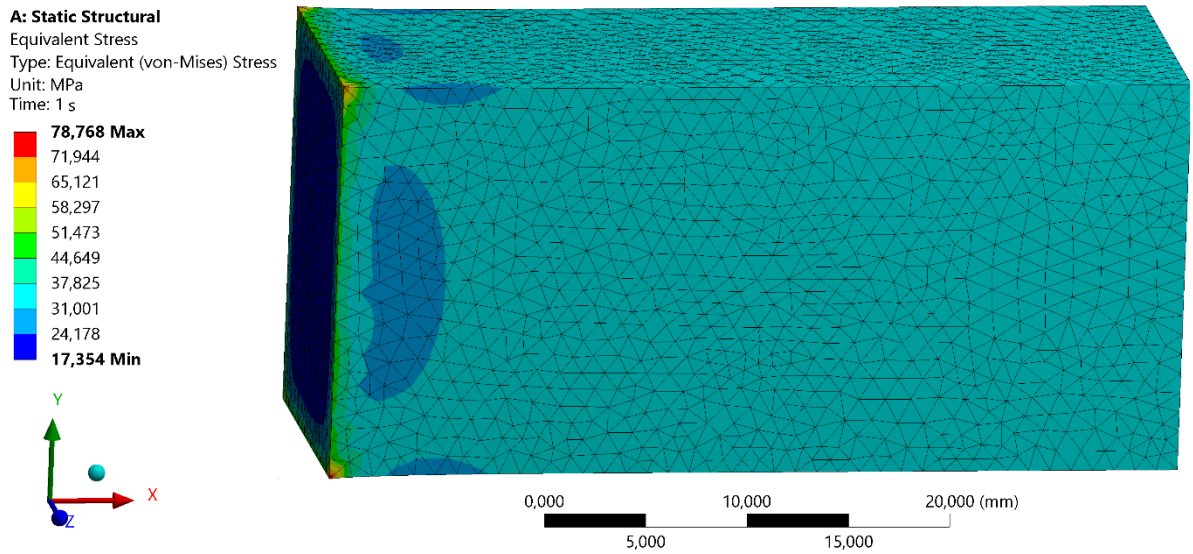
Figure IV.12. *The equivalent (von-Mises) stress for the workpiece without the semi elliptical crack after the pressure loading is applied.*

A: Static Structural
Total Deformation
Type: Total Deformation
Unit: 0 s
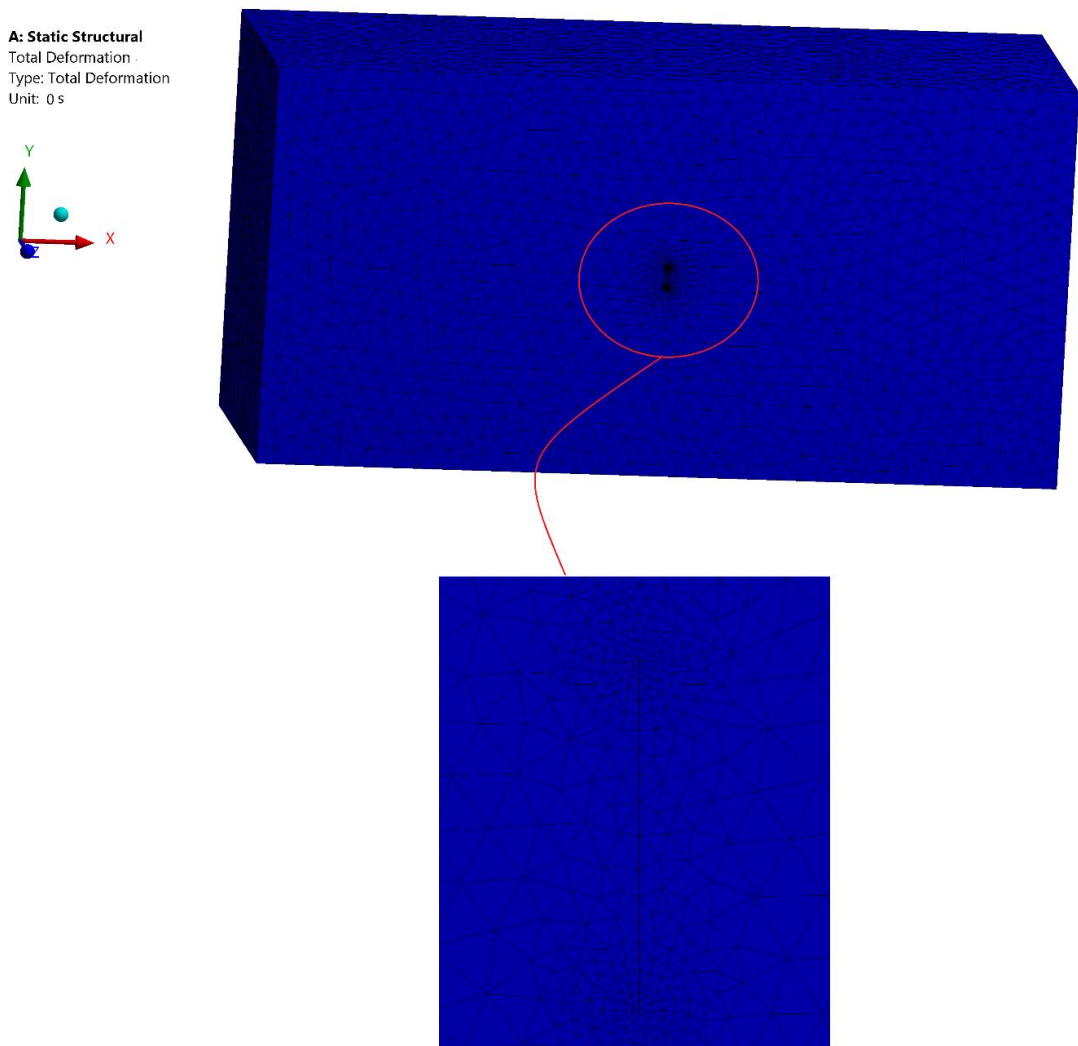
Figure IV.13. *The total deformation for the workpiece with the semi elliptical crack before the pressure loading is applied.*

Figure IV.14 show the total deformation for the workpiece with the semi elliptical crack after the pressure loading is applied.

A: Static Structural
Total Deformation
Type: Total Deformation
Unit: mm
Time: 1 s

0,0069402 Max
0,0061691
0,005398
0,0046268
0,0038557
0,0030845
0,0023134
0,0015423
0,00077114
0 Min
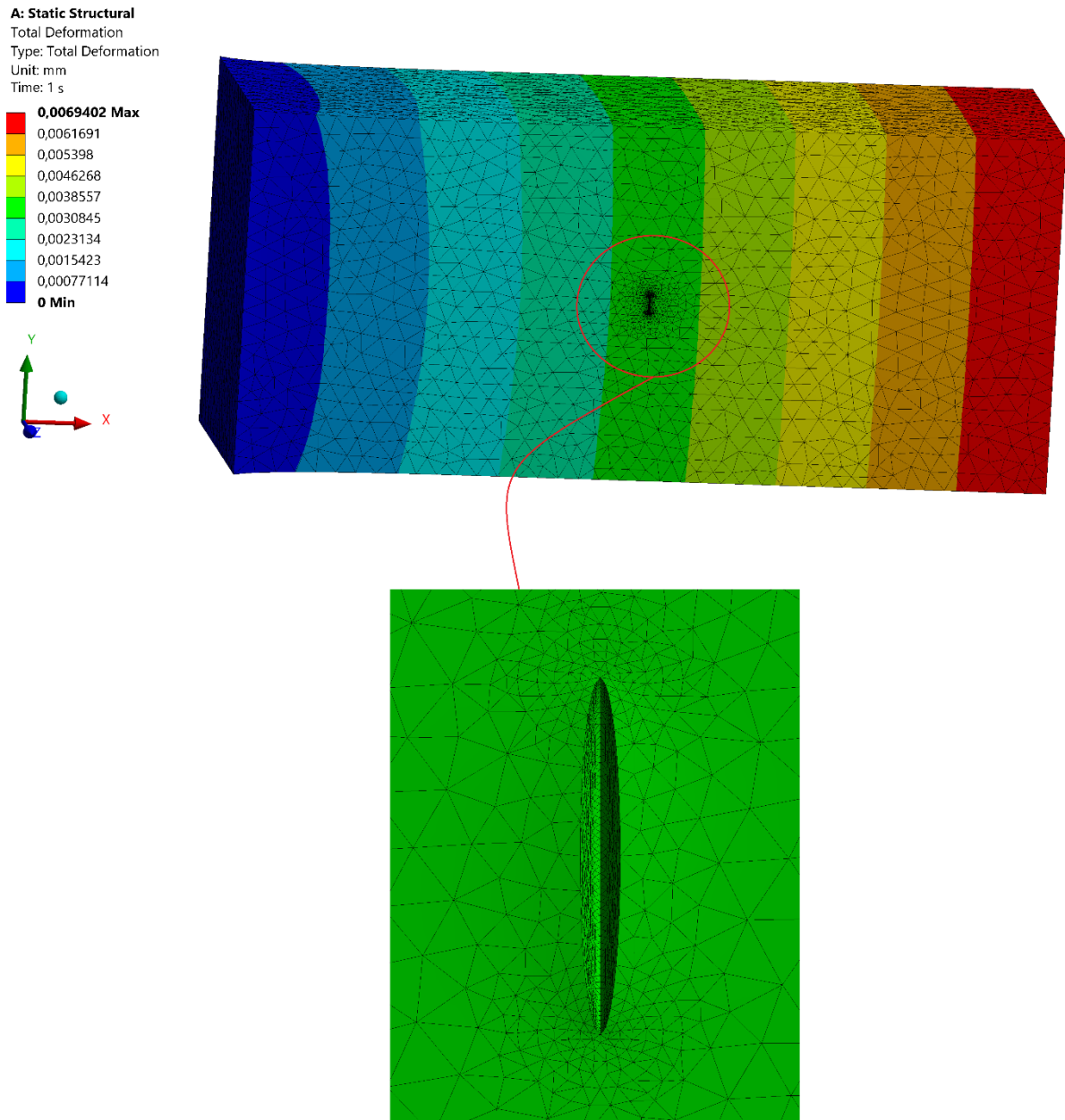
Figure IV.14. The total deformation for the workpiece with the semi elliptical crack after the pressure loading is applied.

Figure IV.15 show the equivalent elastic strain for the workpiece with the semi elliptical crack before the pressure loading is applied.

Figure IV.16 show the equivalent elastic strain for the workpiece without the semi elliptical crack after the pressure loading is applied.

A: Static Structural
Equivalent Elastic Strain
Type: Equivalent Elastic Strain
Unit: 0 s
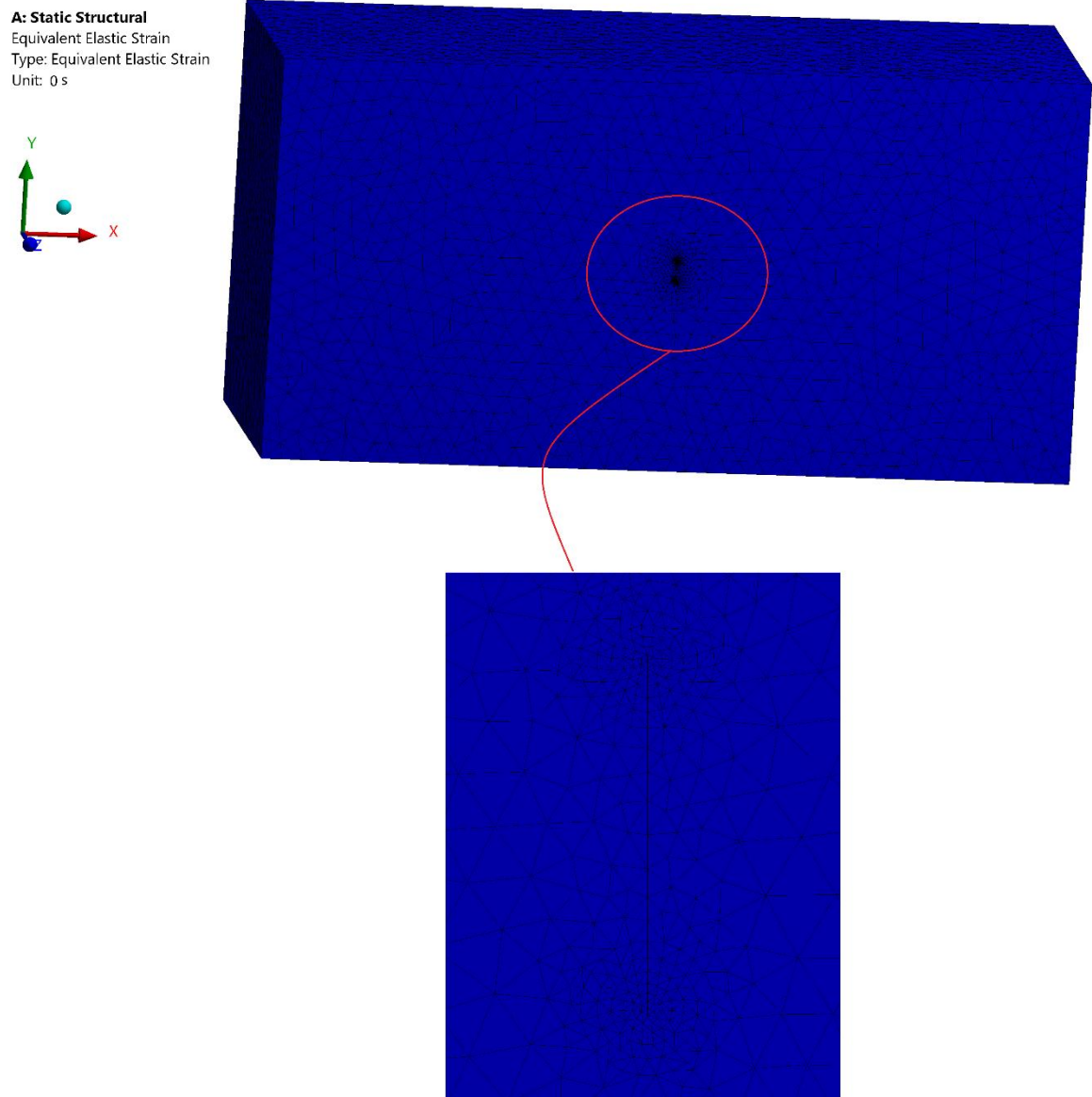
Figure IV.15. The equivalent elastic strain for the workpiece with the semi elliptical crack before the pressure loading is applied.

Figure IV.17 show the equivalent (von-Mises) stress for the workpiece with the semi elliptical crack before the pressure loading is applied.

Figure IV.18 show the equivalent (von-Mises) stress for the workpiece with the semi elliptical crack after the pressure loading is applied.

IV.7.3. Comparison between the workpiece without and with the semi elliptical crack

a) The total deformation

Table IV.4 show the comparison of the total deformation between the workpiece without the semi elliptical crack and the workpiece with the semi elliptical crack.

A: Static Structural
Equivalent Elastic Strain
Type: Equivalent Elastic Strain
Unit: mm/mm
Time: 1 s

0,00085959 Max
0,0007676
0,00067561
0,00058362
0,00049163
0,00039964
0,00030766
0,00021567
0,00012368
3,1689e-5 Min
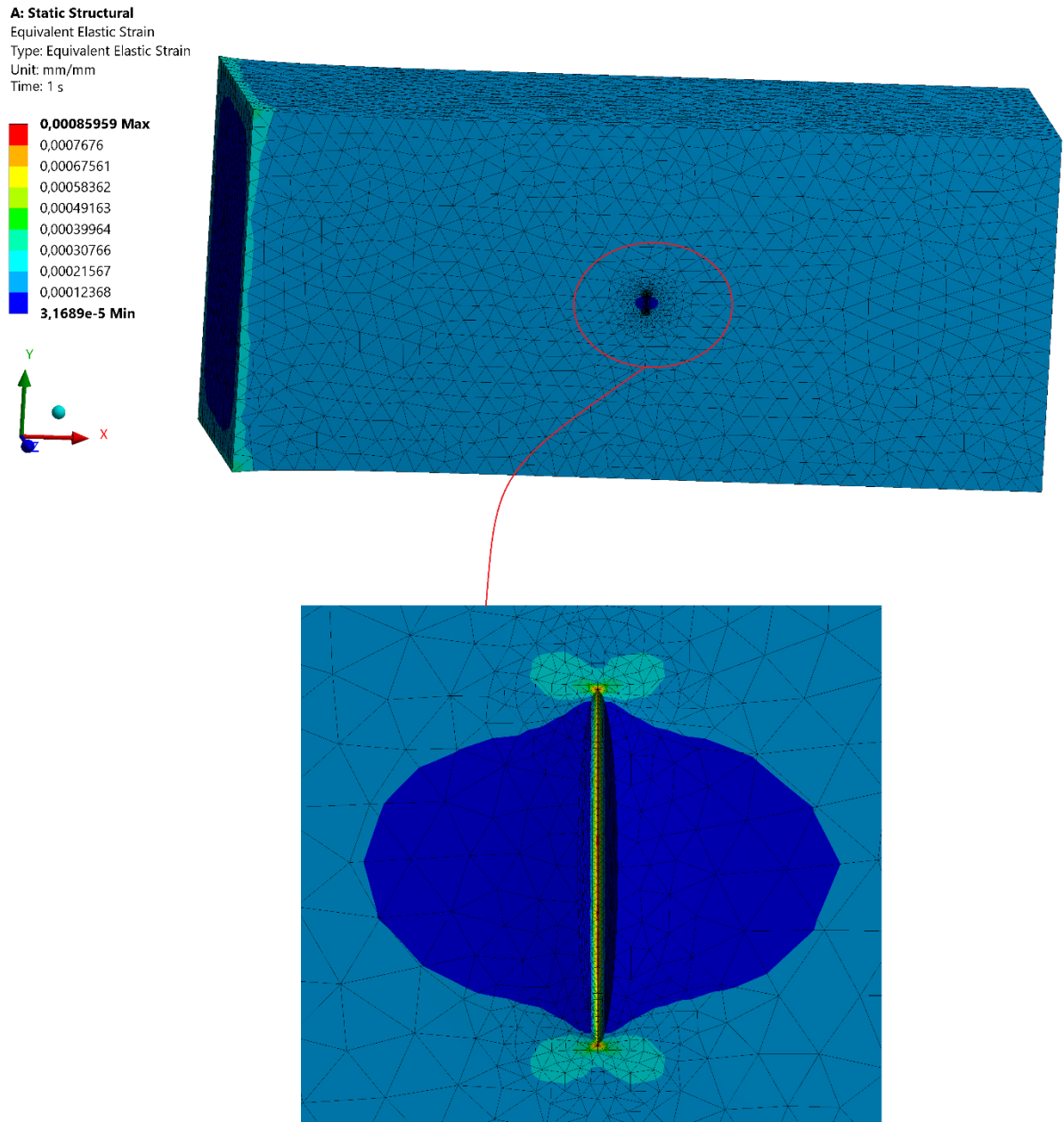
Figure IV.16. *The equivalent elastic strain for the workpiece with the semi elliptical crack after the pressure loading is applied.*

According to Table IV.4, the maximum total deformation observed in the workpiece without the semi-elliptical crack at the final time (1s) is 6.9399e-3 *mm*, whereas the workpiece with the semi-elliptical crack exhibits a slightly greater maximum total deformation of 6.9402e-3 *mm* at the final time (1s). The difference in deformation between the two conditions is minimal, at 0.0003e-3 *mm*, indicating that the presence of the crack has a marginal but discernible impact on the workpiece's total deformation. Although the effect in this case is slight, the accumulation of multiple cracks on the machined surface during the milling process could lead to more substantial differences in deformation.

A: Static Structural
Equivalent Stress
Type: Equivalent (von-Mises) Stress
Unit: 0 s
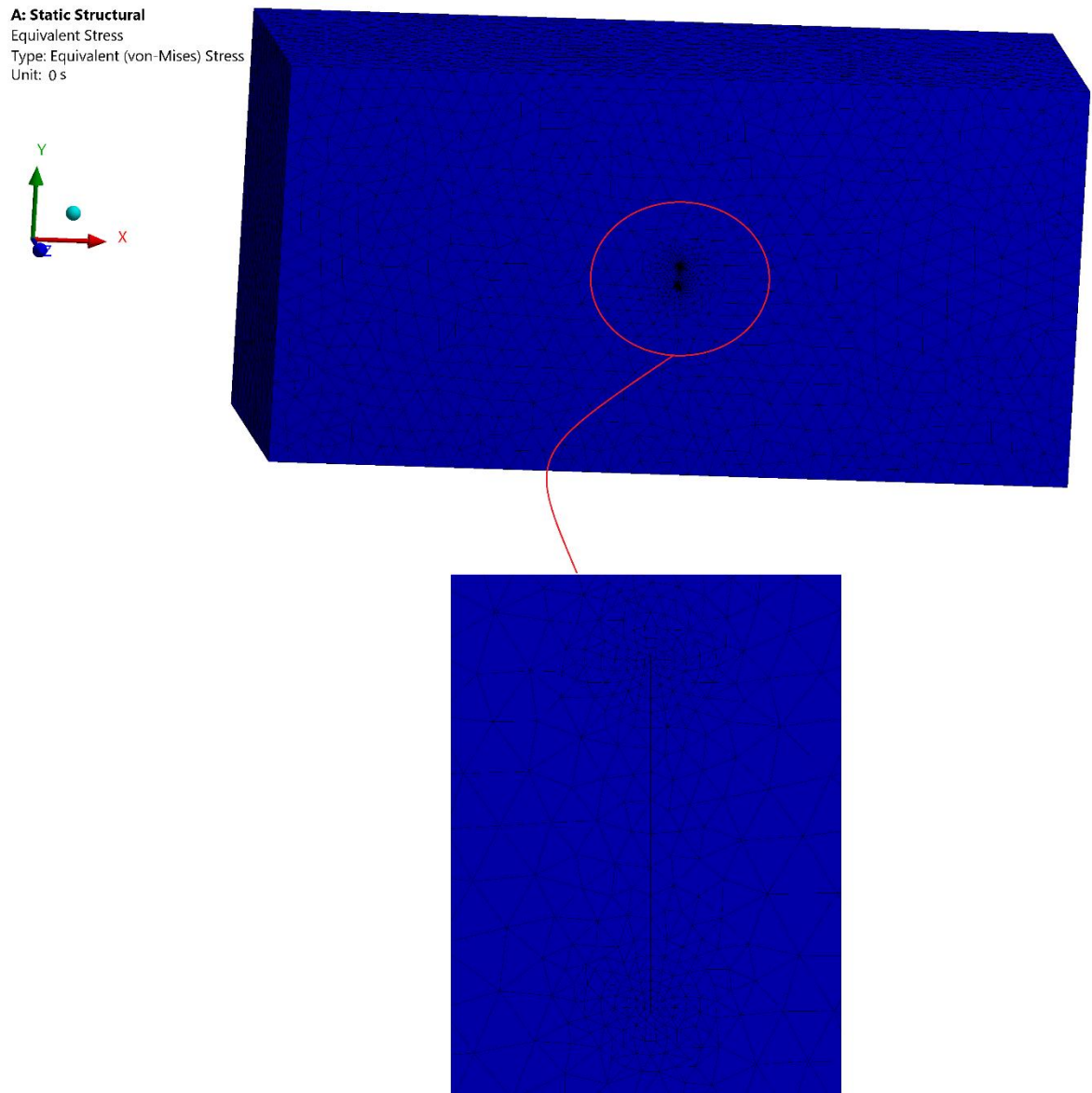
Figure IV.17. *The equivalent (von-Mises) stress for the workpiece with the semi elliptical crack before the pressure loading is applied.*

Table IV.4 Comparison of the total deformation.

Time (s)	The Total Deformation (*mm*)					
	without the semi elliptical crack			with the semi elliptical crack		
	Minimum	Maximum	Average	Minimum	Maximum	Average
0.2	0	1.388e-3	6.8871e-4	0	1.388e-3	6.8764e-4
0.4	0	2.776e-3	1.3774e-3	0	2.7761e-3	1.3753e-3
0.6	0	4.164e-3	2.0661e-3	0	4.1641e-3	2.0629e-3
0.8	0	5.5519e-3	2.7548e-3	0	5.5522e-3	2.7506e-3
1	0	6.9399e-3	3.4435e-3	0	6.9402e-3	3.4382e-3

A: Static Structural
Equivalent Stress
Type: Equivalent (von-Mises) Stress
Unit: MPa
Time: 1 s

125,76 Max
112,43
99,103
85,774
72,446
59,118
45,789
32,461
19,133
5,8043 Min
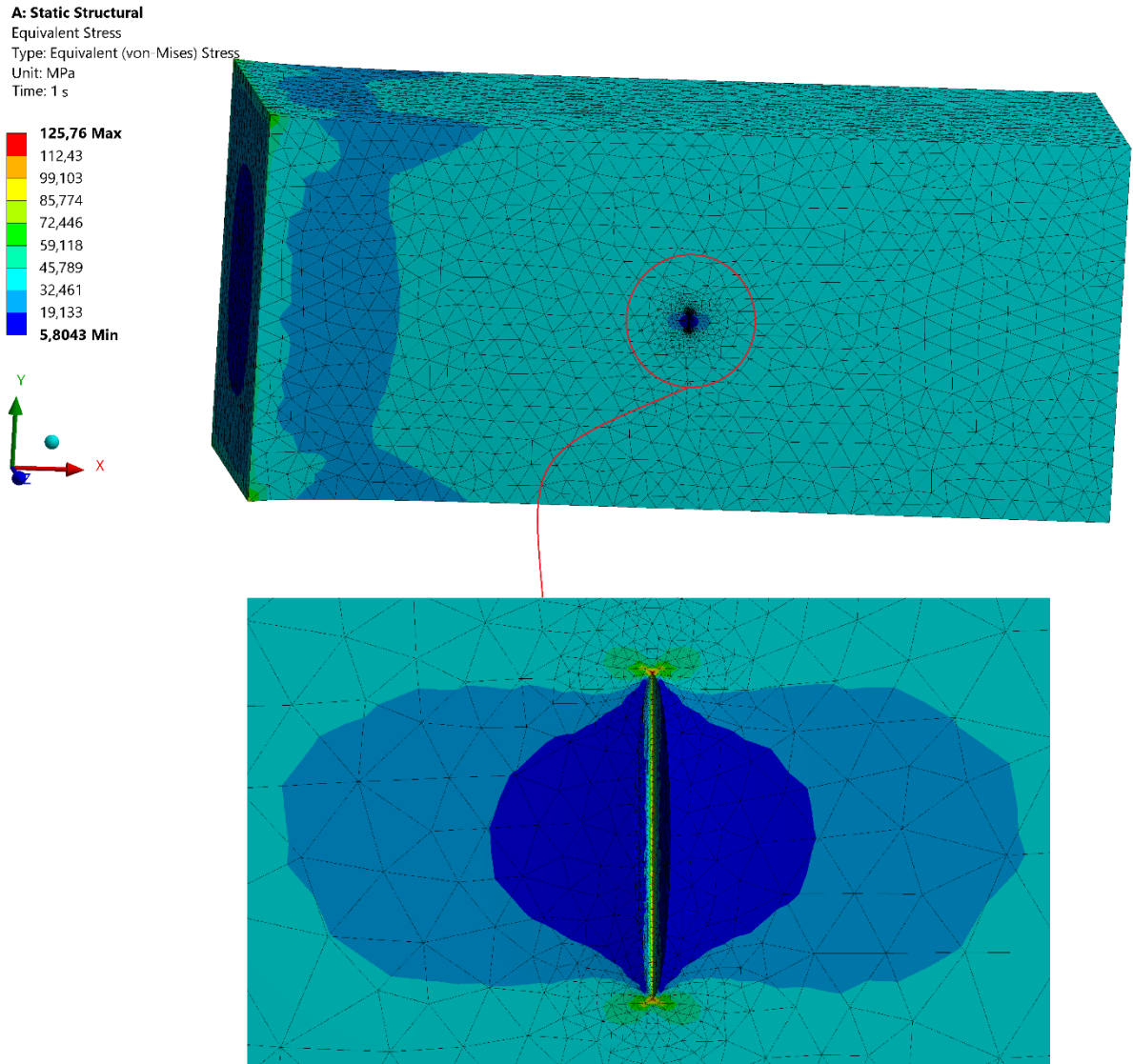
Figure IV.18. *The equivalent (von-Mises) stress for the workpiece with the semi elliptical crack after the pressure loading is applied.*

b) The equivalent elastic strain

Table IV.5 show the comparison of the equivalent elastic strain between the workpiece without the semi elliptical crack and the workpiece with the semi elliptical crack.

Table IV.5 Comparison of the equivalent elastic strain.

| Time (s) | The Equivalent Elastic Strain (*mm/mm*) | | | | | |
| | without the semi elliptical crack | | | with the semi elliptical crack | | |
	Minimum	Maximum	Average	Minimum	Maximum	Average
0.2	1.7369e-5	8.0225e-5	3.4361e-5	6.3378e-6	1.7192e-4	3.5727e-5
0.4	3.4738e-5	1.6045e-4	6.8721e-5	1.2676e-5	3.4384e-4	7.1454e-5
0.6	5.2106e-5	2.4067e-4	1.0308e-4	1.9013e-5	5.1575e-4	1.0718e-4
0.8	6.9475e-5	3.209e-4	1.3744e-4	2.5351e-5	6.8767e-4	1.4291e-4
1	8.6844e-5	4.0112e-4	1.718e-4	3.1689e-5	8.5959e-4	1.7863e-4

According to the data presented in Table IV.5, the minimum equivalent elastic strain (EES) for the workpiece devoid of a semi-elliptical crack at the final time (1s) is measured at 8.6844e-5 *mm/mm*. In contrast, the workpiece featuring a semi-elliptical crack exhibits a lower minimum EES of 3.1689e-5 *mm/mm* at the same final time. The resultant difference, quantified as 5.5155e-5 *mm/mm*, underscores the pronounced impact of the crack on the EES distribution within the material. Furthermore, the analysis of maximum EES values reveals a similar trend but with an inverted relationship. For the intact workpiece, the maximum EES reaches 4.0112e-4 *mm/mm*, while the cracked workpiece presents a significantly higher maximum EES of 8.5959e-4 *mm/mm*. This disparity, amounting to 4.5847e-4 *mm/mm*, further accentuates the critical influence of structural anomalies, such as semi-elliptical cracks, on the elastic strain behavior under load.

The presence of a semi-elliptical crack not only alters the local stress-strain fields but also introduces strain concentrations at the crack tip as show in figure IV.16, which are known to exacerbate the deformation in the surrounding material. This localized increase in strain can significantly accelerate fatigue crack initiation and propagation, thereby reducing the overall fatigue life of the workpiece. The higher maximum EES observed in the cracked workpiece reflects this phenomenon, indicating areas of increased strain concentration that are susceptible to earlier fatigue failure.

c) The equivalent (von-Mises) Stress

Table IV.6 show the comparison of equivalent (von-Mises) stress between the workpiece without the semi elliptical crack and the workpiece with the semi elliptical crack.

Table IV.6 Comparison of the equivalent (von-Mises) stress.

Time (*s*)	The Equivalent (von-Mises) Stress (*MPa*)					
	without the semi elliptical crack			with the semi elliptical crack		
	Minimum	Maximum	Average	Minimum	Maximum	Average
0.2	3.4708	15.754	6.8699	1.1609	25.152	7.0669
0.4	6.9415	31.507	13.74	2.3217	50.304	14.134
0.6	10.412	47.261	20.61	3.4826	75.456	21.201
0.8	13.883	63.015	27.479	4.6434	100.61	28.268
1	17.354	78.768	34.349	5.8043	125.76	35.335

According to the data presented in Table IV.6, the analysis of the equivalent (von-Mises) stress reveals notable differences between the workpiece without a semi-elliptical crack and the one with such a defect, particularly at the final time of 1 *s*. The minimum equivalent (von-Mises) stress for the intact workpiece is recorded at 17.354 *MPa*, indicating a baseline level of

stress under the applied loading conditions. In stark contrast, the presence of a semi-elliptical crack significantly reduces the minimum stress to 5.8043 MPa, with a substantial difference of 11.5497 MPa. This reduction in stress can be attributed to the redistribution of stress around the crack tip as shown in Figure IV.18, which often results in decreased stress levels in certain regions due to the stress concentration effect at the crack tip.

On the other hand, the maximum equivalent (von-Mises) stress tells a different story. For the workpiece devoid of a crack, this value peaks at 78.768 MPa, which serves as a measure of the maximum stress the material can withstand without yielding. However, the introduction of a semi-elliptical crack elevates the maximum equivalent (von-Mises) stress to 125.76 MPa, an increase of 46.992 MPa. This heightened stress level near the crack vicinity underscores the severe stress concentration induced by the crack, potentially pushing the material closer to its yield point or even causing localized plastic deformation.

The implications of these findings extend beyond mere stress analysis. The elevated maximum stress in the presence of a crack can significantly accelerate the initiation and propagation of fatigue cracks, thereby compromising the workpiece's fatigue life. The stress concentration factor, which quantifies the increase in stress due to the presence of a crack, plays a pivotal role in determining the rate of crack growth under cyclic loading. As such, the increased maximum equivalent (von-Mises) stress observed in the cracked workpiece signals a heightened risk of premature failure due to fatigue.

Moreover, the reduction in minimum stress in the cracked workpiece may not necessarily imply a safer condition. The fluctuation between the reduced minimum and elevated maximum stresses can lead to a more pronounced stress range during cyclic loading, further exacerbating the material's fatigue response. This increased stress range can induce more significant cyclic plastic deformation, accelerating the fatigue crack growth and ultimately leading to a reduced service life of the component.

Finally, the analysis of equivalent (von-Mises) stress in workpieces with and without semi-elliptical cracks provides critical insights into the detrimental effects of such defects on material performance. The significant differences in both minimum and maximum stress levels highlight the profound impact of crack-induced stress concentrations on the structural integrity and fatigue resistance of materials. These findings emphasize the importance of rigorous material inspection and defect management strategies in the design and maintenance of structural components, particularly those subjected to cyclic loading conditions, to ensure their reliability and longevity in service.

IV.8. Conclusion

In this chapter, ANSYS was utilized to compare the total deformation, equivalent elastic strain, and equivalent (von-Mises) stress between a presumed milled workpiece without a crack and with a crack present on its surface. This analysis aimed to elucidate the influence of surface integrity on fatigue life. The findings revealed that the presence of a crack significantly affected the performance of the workpiece under pressure loading.

Moreover, the implications of these findings extend beyond a singular crack's influence. In scenarios where multiple cracks are present on the surface of the workpiece, one can anticipate a compounded effect, leading to a more pronounced reduction in fatigue life. Each additional crack introduces new stress concentration points, further distorting the stress-strain distribution and potentially leading to a network of interacting cracks. This interaction can result in a complex crack propagation pattern, further diminishing the structural integrity and fatigue resistance of the material.

General Conclusion

In this work, an experimental study was carried out to investigate the influence of cutting parameters on three aspects of machining performance, namely, cutting temperature, surface roughness, and microhardness of the milled AISI 1060. Response Surface Methodology (RSM) was used for evaluating and predicting the impact of those cutting parameters on the surface integrity, and the most influencing parameters have been identified, then a multi-objective optimization using the genetic algorithm (GA) was done to get the optimal combinations of cutting parameters to minimize the production time and also the production cost per unit. Finally, the advanced simulation capabilities of ANSYS were used to compare the total deformation, equivalent elastic strain, and equivalent (von-Mises) stress between a presumed milled workpiece without a crack and with a crack present on its surface. This analysis aimed to elucidate the influence of surface integrity on fatigue life.

The key results of this study are outlined below:

- Three robust empirical models were developed, delineating the intricate relationship between cutting parameters and the resulting cutting temperature, roughness, and microhardness. These models demonstrated high predictive accuracy, with average error rates of 3.19 %, 5.32 %, and 1.63 % for cutting temperature, roughness, and microhardness respectively.

- ANOVA revealed significant factors influencing each response, shedding light on key contributors to the observed variations in cutting temperature, roughness, and microhardness.

- According to the ANOVA results, f_z and a_p were the most significant factors on cutting temperature with a contribution of 20.62 % and 9 % respectively. In addition, the most significant interaction factors were $f_z \times a_p \times a_p$ followed by $V_c \times f_z \times a_p$ with a contribution of 8.7 % and 4.5 % respectively.

- The factor that has the highest significance on surface roughness is V_c with a contribution of 13.77 %. Moreover, the interaction factor that has the highest significance is $V_c \times a_p \times a_p$ with a contributing of 18.56 %.

- The factor that has the highest significance on surface microhardness is a_p with a contribution of 12.53 %. In addition, the most significant interaction factors are

$V_c \times V_c \times f_z$ followed by $f_z \times f_z \times a_p$ with a contribution of 14.42 % and 10.16 % respectively.

- Employing 3D response surface plots enhanced the visual comprehension of the complex interplay between cutting parameters and the resulting cutting temperature, roughness, and microhardness.

- The application of multi-objective optimization using genetic algorithms yielded optimal solutions that minimized production cycle time and cost per unit. Despite subtle numerical differences, achieving a minimum production cycle time per unit of 1.7217 *min* and a minimum cost per unit of 1.1858 *Euro* underscored the delicate balance between time efficiency and cost-effectiveness in machining operations.

- The integration of RSM and genetic algorithms in this research marks a departure from generic empirical models, offering a refined and precise approach to controlling surface roughness and microhardness in specific machining contexts. Beyond its immediate application in AISI 1060 milling, this methodology presents promising potential for broader implementation across diverse machining domains.

- In essence, this study not only enriches our understanding of optimizing AISI 1060 machining but also introduces a methodological paradigm with substantial implications for advancing precision and control in machining processes.

- The results of the simulation using ANYSY revealed that the presence of a crack significantly affected the performance of the workpiece under pressure loading.

- The presence of a crack on the surface of the workpiece has a marginal but discernible impact on its total deformation. Although the effect in this case is slight, the accumulation of multiple cracks on its surface could lead to more substantial differences in deformation.

- The equivalent elastic strain and equivalent (von-Mises) stress of the workpiece are greatly affected by the presence of the crack on its surface.

- The presence of a crack not only alters the local stress-strain fields but also introduces stress-strain concentrations at the crack tip.

- This localized increase in stress-strain can significantly accelerate fatigue crack initiation and propagation, thereby reducing the overall fatigue life of the workpiece.

- the implications of these findings extend beyond a singular crack's influence. In scenarios where multiple cracks are present on the surface of the workpiece, one can anticipate a compounded effect, leading to a more pronounced reduction in fatigue life. Each additional crack introduces new stress concentration points, further distorting the stress-strain distribution and potentially leading to a network of interacting cracks. This interaction can result in a complex crack propagation pattern, further diminishing the structural integrity and fatigue resistance of the material.

References

1. Groover MP (2013) Fundamentals of Modern Manufacturing Material, Processes, and Systems, 5th Edition

2. Kohser RA (1998) Materials and processes in manufacturing

3. Société SANDVIK-COROMANT (2001) Fraisage - Principes. Trav des matériaux - Assem 33:0–22. https://doi.org/10.51257/a-v1-bm7082

4. Singh R, Bajpai V (2013) Handbook of Manufacturing Engineering and Technology

5. Leonidas E, Ayvar-Soberanis S, Laalej H, et al (2022) A Comparative Review of Thermocouple and Infrared Radiation Temperature Measurement Methods during the Machining of Metals. Sensors 22:1–23. https://doi.org/10.3390/s22134693

6. Elmaraghy H, Deif AM, Systems IM, Program SE (2014) CIRP Encyclopedia of Production Engineering

7. Marakini V, Pai SP, Bhat UK, et al (2022) High-speed face milling of AZ91 Mg alloy: Surface integrity investigations. Int J Light Mater Manuf 5:528–542. https://doi.org/10.1016/j.ijlmm.2022.06.006

8. Altas E, Altin Karatas M, Gokkaya H, Akinay Y (2021) Surface Integrity of NiTi Shape Memory Alloy in Milling with Cryogenic Heat Treated Cutting Tools under Different Cutting Conditions. J Mater Eng Perform 30:9426–9439. https://doi.org/10.1007/s11665-021-06095-3

9. Zhao W, Ren F, Iqbal A, et al (2020) Effect of liquid nitrogen cooling on surface integrity in cryogenic milling of Ti-6Al-4 V titanium alloy. Int J Adv Manuf Technol 106:1497–1508. https://doi.org/10.1007/s00170-019-04721-y

10. Molaiekiya F, Aliakbari Khoei A, Aramesh M, Veldhuis SC (2021) Machined surface integrity of inconel 718 in high-speed dry milling using SiAlON ceramic tools. Int J Adv Manuf Technol 112:1941–1950. https://doi.org/10.1007/s00170-020-06471-8

11. Zheng G, Cheng X, Dong Y, et al (2020) Surface integrity evaluation of high-strength steel with a TiCN-NbC composite coated tool by dry milling. Meas J Int Meas Confed 166:108204. https://doi.org/10.1016/j.measurement.2020.108204

12. Race A, Zwierzak I, Secker J, et al (2021) Environmentally sustainable cooling strategies in milling of SA516: Effects on surface integrity of dry, flood and MQL machining. J Clean Prod 288:125580. https://doi.org/10.1016/j.jclepro.2020.125580

13. Holmberg J, Wretland A, Berglund J, Beno T (2020) Selection of milling strategy based on surface integrity investigations of highly deformed Alloy 718 after ceramic and cemented carbide milling. J Manuf Process 58:193–207.

https://doi.org/10.1016/j.jmapro.2020.08.010

14. Saleem MQ, Mumtaz S (2020) Face milling of Inconel 625 via wiper inserts: Evaluation of tool life and workpiece surface integrity. J Manuf Process 56:322–336. https://doi.org/10.1016/j.jmapro.2020.04.011

15. Gong L, Zhao W, Ren F, et al (2019) Experimental study on surface integrity in cryogenic milling of 35CrMnSiA high-strength steel. Int J Adv Manuf Technol 103:605–615. https://doi.org/10.1007/s00170-019-03577-6

16. Davis R, Singh A (2020) Tailoring Surface Integrity of Biomedical Mg Alloy AZ31B Using Distinct End Mill Treatment Conditions and Machining Environments. J Mater Eng Perform 29:7617–7635. https://doi.org/10.1007/s11665-020-05203-z

17. Hassanpour H, Sadeghi MH, Rasti A, Shajari S (2016) Investigation of surface roughness, microhardness and white layer thickness in hard milling of AISI 4340 using minimum quantity lubrication. J Clean Prod 120:124–134. https://doi.org/10.1016/j.jclepro.2015.12.091

18. Yi J, Jiao L, Wang X, et al (2015) Surface roughness models and their experimental validation in micro milling of 6061-T6 al alloy by response surface methodology. Math Probl Eng 2015:. https://doi.org/10.1155/2015/702186

19. Santhakumar J, Mohammed Iqbal U (2019) Parametric optimization of trochoidal step on surface roughness and dish angle in end milling of AISID3 steel using precise measurements. Materials (Basel) 12:. https://doi.org/10.3390/ma12081335

20. Karkalos NE, Galanis NI, Markopoulos AP (2016) Surface roughness prediction for the milling of Ti-6Al-4V ELI alloy with the use of statistical and soft computing techniques. Meas J Int Meas Confed 90:25–35. https://doi.org/10.1016/j.measurement.2016.04.039

21. Kasim MS, Hafiz MSA, Ghani JA, et al (2019) Investigation of surface topology in ball nose end milling process of Inconel 718. Wear 426–427:1318–1326. https://doi.org/10.1016/j.wear.2018.12.076

22. Bhopale NN, Joshi SS, Pawade RS (2015) Experimental Investigation into the Effect of Ball End Milling Parameters on Surface Integrity of Inconel 718. J Mater Eng Perform 24:986–998. https://doi.org/10.1007/s11665-014-1323-y

23. Akhtar W, Sun J, Chen W (2016) Effect of Machining Parameters on Surface Integrity in High Speed Milling of Super Alloy GH4169/Inconel 718. Mater Manuf Process 31:620–627. https://doi.org/10.1080/10426914.2014.994769

24. Najiha MS, Rahman MM (2015) Experimental study on minimum quantity lubrication in end milling of AA6061-t6 using TiAlN coated carbide tools. Int J Automot Mech Eng 11:2771–2785. https://doi.org/10.15282/ijame.11.2015.52.0233

25. Mantle AL, Aspinwall DK (2001) Surface integrity of a high speed milled gamma titanium aluminide. J Mater Process Technol 118:143–150. https://doi.org/10.1016/S0924-0136(01)00914-1

References

26. Bouzid Saï W, Ben Salah N, Lebrun JL (2001) Influence of machining by finishing milling on surface characteristics. Int J Mach Tools Manuf 41:443–450. https://doi.org/10.1016/S0890-6955(00)00069-9

27. Wang X (2008) Intelligent prediction of surface micro-hardness after milling based on smooth support vector regression. Proc - 2008 Int Symp Knowl Acquis Model KAM 2008 728–731. https://doi.org/10.1109/KAM.2008.142

28. Ginting A, Nouari M (2009) Surface integrity of dry machined titanium alloys. Int J Mach Tools Manuf 49:325–332. https://doi.org/10.1016/j.ijmachtools.2008.10.011

29. Jin D, Liu Z (2013) Damage of the machined surface and subsurface in orthogonal milling of FGH95 superalloy. Int J Adv Manuf Technol 68:1573–1581. https://doi.org/10.1007/s00170-013-4944-7

30. Wang F, Zhao J, Li A, Zhang H (2014) Effects of cutting conditions on microhardness and microstructure in high-speed milling of h13 tool steel. Int J Adv Manuf Technol 73:137–146. https://doi.org/10.1007/s00170-014-5812-9

31. Muñoz-Escalona P, Shokrani A, Newman ST (2015) Influence of cutting environments on surface integrity and power consumption of austenitic stainless steel. Robot Comput Integr Manuf 36:60–69. https://doi.org/10.1016/j.rcim.2014.12.013

32. Houchuan Y, Zhitong C, ZiTong Z (2015) Influence of cutting speed and tool wear on the surface integrity of the titanium alloy Ti-1023 during milling. Int J Adv Manuf Technol 78:1113–1126. https://doi.org/10.1007/s00170-014-6593-x

33. Mathoho I, Titilayo Akinlabi E, Patrick Mubiayi M, Mbohwa C (2018) Effect of milling parameters on microhardness and microstructure during dry and flood milling of Ti-6Al-4V. IOP Conf Ser Mater Sci Eng 423:. https://doi.org/10.1088/1757-899X/423/1/012161

34. AISI 1060 Carbon Steel (UNS G10600). https://www.azom.com/article.aspx?ArticleID=6542. Accessed 14 Mar 2022

35. Sandvik Coromant - manufacturing tools & machining solutions. https://www.sandvik.coromant.com/en-us. Accessed 9 Nov 2021

36. Zahoor S, Saleem MQ, Abdul-Kader W, et al (2019) Improving surface integrity aspects of AISI 316L in the context of bioimplant applications. Int J Adv Manuf Technol 105:2857–2867. https://doi.org/10.1007/s00170-019-04444-0

37. Wang X, Huang C, Zou B, et al (2018) Experimental study of surface integrity and fatigue life in the face milling of inconel 718. Front Mech Eng 13:243–250. https://doi.org/10.1007/s11465-018-0479-9

38. Lu X, Jia Z, Wang H, et al (2019) The effect of cutting parameters on micro-hardness and the prediction of Vickers hardness based on a response surface methodology for micro-milling Inconel 718. Meas J Int Meas Confed 140:56–62. https://doi.org/10.1016/j.measurement.2019.03.037

39. Abbas AT, Helmy MO, Al-Abduljabbar AA, et al (2023) Precision Face Milling of

Maraging Steel 350: An Experimental Investigation and Optimization Using Different Machine Learning Techniques. Machines 11:1001. https://doi.org/10.3390/machines11111001

40. Ping Z, Xiujie Y, Penghao W, Xiao Y (2021) Surface integrity and tool wear mechanism of 7050-T7451 aluminum alloy under dry cutting. Vacuum 184:109886. https://doi.org/10.1016/j.vacuum.2020.109886

41. Wang Z, Liu Y (2020) Study of surface integrity of milled gamma titanium aluminide. J Manuf Process 56:806–819. https://doi.org/10.1016/j.jmapro.2020.05.021

42. Bembenek M, Dzienniak D, Dzindziora A, et al (2023) Investigation of the Impact of Selected Face Milling Parameters on the Roughness of the Machined Surface for 1.4301 Steel. Adv Sci Technol Res J 17:299–312. https://doi.org/10.12913/22998624/170422

43. Leo Kumar SP (2018) Experimental investigations and empirical modeling for optimization of surface roughness and machining time parameters in micro end milling using Genetic Algorithm. Meas J Int Meas Confed 124:386–394. https://doi.org/10.1016/j.measurement.2018.04.056

44. Yang Y (2018) Machining parameters optimization of multi-pass face milling using a chaotic imperialist competitive algorithm with an efficient constraint-handling mechanism. C - Comput Model Eng Sci 116:365–389. https://doi.org/10.31614/cmes.2018.03847

45. Fang Y, Zhao L, Lou P, Yan J (2021) Cutting parameter optimization method in multi-pass milling based on improved adaptive PSO and SA. J Phys Conf Ser 1848:. https://doi.org/10.1088/1742-6596/1848/1/012116

46. Li B, Tian X, Zhang M (2020) Modeling and multi-objective optimization of cutting parameters in the high-speed milling using RSM and improved TLBO algorithm. Int J Adv Manuf Technol 111:2323–2335. https://doi.org/10.1007/s00170-020-06284-9

47. Su Y, Zhao G, Zhao Y, et al (2020) Multi-objective optimization of cutting parameters in turning AISI 304 austenitic stainless steel. Metals (Basel) 10:. https://doi.org/10.3390/met10020217

48. Rana M, Singh T, Sharma VK, et al (2021) Optimization of surface integrity in face milling of AISI 52,100 alloy steel using Taguchi based grey relational analysis. Mater Today Proc 50:2105–2110. https://doi.org/10.1016/j.matpr.2021.09.430

49. Zhao J, Li L, Nie H, et al (2021) Multi-objective integrated optimization of tool geometry angles and cutting parameters for machining time and energy consumption in NC milling. Int J Adv Manuf Technol 117:1427–1444. https://doi.org/10.1007/s00170-021-07772-2

50. Pham V-H, Thuy DN (2023) Investigation and optimization of parameters in face milling of s50c steel under mql system. J Appl Eng Sci 21:

51. Zhou L, Li J, Li F, et al (2018) Optimization Parameters for Energy Efficiency in End milling. Procedia CIRP 69:312–317. https://doi.org/10.1016/j.procir.2017.12.005

52. Rajeswari B, Amirthagadeswaran KS (2018) Study of machinability and parametric optimization of end milling on aluminium hybrid composites using multi-objective genetic algorithm. J Brazilian Soc Mech Sci Eng 40:1–15. https://doi.org/10.1007/s40430-018-1293-3

53. Xu J, Yan F, Li Y, et al (2020) Multiobjective Optimization of Milling Parameters for Ultrahigh-Strength Steel AF1410 Based on the NSGA-II Method. Adv Mater Sci Eng 2020:. https://doi.org/10.1155/2020/8796738

54. Cheng DJ, Xu F, Xu SH, et al (2020) Minimization of Surface Roughness and Machining Deformation in Milling of Al Alloy Thin-Walled Parts. Int J Precis Eng Manuf 21:1597–1613. https://doi.org/10.1007/s12541-020-00366-0

55. Wang P, Bai Q, Cheng K, et al (2023) Multi-Objective Optimization of Micro-Milling Parameters—The Trade-Offs between Machining Quality, Efficiency, and Sustainability in the Fabrication of Thin-Walled Microstructures. Appl Sci 13:. https://doi.org/10.3390/app13169392

56. Tran CC, Luu VT, Nguyen VT, et al (2023) Multi-objective Optimization of CNC Milling Parameters of 7075 Aluminium Alloy Using Response Surface Methodology. Jordan J Mech Ind Eng 17:393–402. https://doi.org/10.59038/jjmie/170308

57. Huang W, Wan C, Wang G, Zhang G (2023) Surface integrity optimization for ball-end hard milling of AISI D2 steel based on response surface methodology. PLoS One 18:1–23. https://doi.org/10.1371/journal.pone.0290760

58. Muhammad A, Gupta MK, Mikołajczyk T, et al (2021) Effect of tool coating and cutting parameters on surface roughness and burr formation during micromilling of inconel 718. Metals (Basel) 11:1–18. https://doi.org/10.3390/met11010167

59. Hernández-González LW, Pérez-Rodríguez R, Quesada-Estrada AM, Dumitrescu L (2018) Effects of cutting parameters on surface roughness and hardness in milling of AISI 304 steel. DYNA 85:57–63. https://doi.org/10.15446/dyna.v85n205.64798

60. Nguyen T, Pham V-H (2023) The INVESTIGATION AND OPTIMIZATION OF PARAMETERS IN FACE MILLING OF S50C STEEL UNDER MQL SYSTEM. J Appl Eng Sci 1–14. https://doi.org/10.5937/jaes0-38857

61. Oosthuizen GA, Nunco K, Conradie PJT, Dimitrov DM (2016) The effect of cutting parameters on surface integrity in milling TI6AL4V. South African J Ind Eng 27:115–123. https://doi.org/10.7166/27-4-1199

62. Yang X, Ren C, Wang Y, Chen G (2012) Experimental study on surface integrity of ti-6al-4v in high speed side milling. Trans Tianjin Univ 18:206–212. https://doi.org/10.1007/s12209-012-1784-8

63. Nefedov N (1987) Typical examples and problems in metal cutting and tool design.

Abstract

In this work an experimental study was carried out to investigate the influence of the cutting parameters namely cutting speed (V_c), feed per tooth (f_z) and depth of cut (a_p) on three machining performance aspects, including cutting temperature (Q_c), surface roughness (R_a) and microhardness (H) when milling of AISI 1060 steel. Response surface methodology (RSM) was used for evaluating and predicting the impact of the considered cutting parameters on the selected machining characteristic indices. The results reveled that the error rates of the developed models' values compared to experimental ones were found to be as follows: 3.19 % for Q_c, 5.32 % for R_a, 1.63 % for H, these error rates underscore the robustness and reliability of the developed models in accurately predicting the respective machining characteristics. Moreover, our study stands out in its approach by leveraging the experimentally developed RSM models as constraints within the optimization framework, providing a more precise and tailored approach compared to relying on generalized empirical models commonly found in industry handbooks. This is why a multi-objective optimization using genetic algorithm (GA) was performed to minimize both the production time and the production cost per unit by defining the problem with three key cutting parameters and utilizing the experimentally derived Response Surface Methodology (RSM) models as constraints. For instance, the R_a and H-based RSM models served as constraints ensuring a surface roughness and microhardness values below a specified threshold while satisfying other machining constraints (tool life, cutting force and cutting power). As a result, a set of optimal solutions of combinations of cutting parameters is achieved for simultaneously minimum production time and production cost per unit. Finally, the advanced simulation capabilities of ANSYS were used to compare the total deformation, equivalent elastic strain, and equivalent (von-Mises) stress between a presumed milled workpiece without a crack and with a crack present on its surface. This analysis aimed to elucidate the influence of surface integrity on fatigue life of the machined workpieces. The findings revealed that the presence of a crack significantly affected the performance of the machined workpiece under pressure loading.

Keywords: milling, surface integrity, cutting parameters, cutting temperature, roughness, microhardness, crack, fatigue.

Résumé

Dans ce travail, une étude expérimentale a été réalisée pour enquêter sur l'influence des paramètres de coupe, à savoir la vitesse de coupe (V_c), l'avance par dent (f_z) et la profondeur de passe (a_p), sur trois aspects de la performance d'usinage, incluant la température de coupe (Q_c), la rugosité de surface (R_a) et la microdureté (H) lors du fraisage de l'acier AISI 1060. La méthodologie de surface de réponse (RSM) a été utilisée pour évaluer et prédire l'impact des paramètres de coupe considérés sur les indices caractéristiques de l'usinage sélectionnés. Les résultats ont révélé que les taux d'erreur des modèles développés par rapport aux valeurs expérimentales étaient comme suit : 3.19 % pour Q_c, 5.32 % pour R_a et 1.63 % pour H. Ces taux d'erreur soulignent la robustesse et la fiabilité des modèles développés dans la prédiction précise des caractéristiques d'usinage respectives. De plus, notre étude se distingue par son approche en tirant parti des modèles RSM développés expérimentalement comme contraintes au sein du cadre d'optimisation, offrant une approche plus précise et sur mesure par rapport à celle qui repose sur des modèles empiriques généralisés couramment trouvés dans les manuels industriels. C'est pourquoi une optimisation multi-objectifs utilisant l'algorithme génétique (GA) a été effectuée pour minimiser à la fois le temps de production et le coût de production par unité en définissant le problème avec trois paramètres de coupe clés et en utilisant les modèles RSM dérivés expérimentalement comme contraintes. Par exemple, le modèle RSM basé sur R_a et H a servi de contraintes garantissant des valeurs de rugosité de surface et de microdureté inférieures à un seuil spécifié tout en satisfaisant d'autres contraintes d'usinage (durée de vie de l'outil, force de coupe, puissance de coupe). En conséquence, un ensemble de solutions optimales de combinaisons de paramètres de coupe est obtenu pour minimiser simultanément le temps de production et le coût par unité. Finalement, les capacités avancées de simulation d'ANSYS ont été utilisées pour comparer la déformation totale, la contrainte élastique équivalente et la contrainte équivalente (de von Mises) entre une pièce supposée usinée sans fissure et avec une fissure présente à sa surface. Cette analyse visait à élucider l'influence de l'intégrité de surface sur la durée de vie en fatigue des pièces usinées. Les résultats ont révélé que la présence d'une fissure affectait significativement les performances de la pièce usinée sous l'effet d'une pression appliquée.

Mots-clés : fraisage, intégrité de surface, paramètres de coupe, température de coupe, rugosité, microdureté, fissure, fatigue.

الملخص

في هذا العمل، تم إجراء دراسة تجريبية للتحقيق في تأثير شروط القطع والتي تشمل سرعة القطع (V_c)، التغذية لكل سن (f_z)، وعمق القطع (a_p) على ثلاث جوانب من خصائص التصنيع عن طريق نزع المادة، تتضمن درجة حرارة القطع (Q_c)، خشونة السطح (R_a)، والصلادة الدقيقة (H) عند تفريز فولاذ من نوع AISI 1060. وتم استخدام منهجية سطح الاستجابة (RSM) لتقييم والتنبؤ بتأثير شروط القطع المعتبرة على مؤشرات خصائص التصنيع المحددة. وأظهرت النتائج أن معدلات الخطأ لقيم النماذج المطورة مقارنة بالقيم التجريبية وكانت على النحو التالي: 3.19 % لدرجة حرارة القطع، 5.32 % لخشونة السطح، 1.63 % للصلادة الدقيقة. معدلات الخطأ هذه تؤكد على اعتمادية وموثوقية النماذج المطورة في التنبؤ بدقة بخصائص التصنيع المعنية. علاوة على ذلك، يبرز بحثنا في نهجه من خلال استغلال النماذج المطورة تجريبيًا كقيود ضمن إطار الاستمثال، مما يوفر نهجًا أكثر دقة وتخصيصًا مقارنةً بالاعتماد على النماذج التجريبية العامة الموجودة عادة في كتيبات التصنيع .لهذا السبب، تم إجراء استمثال متعدد الأهداف باستخدام خوارزمية الجينات لتقليل كل من وقت الإنتاج وتكلفة الإنتاج لكل وحدة عن طريق تعريف المشكلة بثلاث شروط قطع رئيسية واستخدام نماذج منهجية سطح الاستجابة المشتقة تجريبيًا كقيود. على سبيل المثال، خدمت نماذج منهجية سطح الاستجابة المبنية على الخشونة والصلادة الدقيقة كقيود لضمان قيم خشونة السطح و الصلادة الدقيقة أقل من عتبة محددة مع تلبية قيود تصنيع أخرى (عمر الأداة، قوة القطع، استهلاك الطاقة) .و نتيجة لذلك، تم تحقيق مجموعة من الحلول المثالية لمجموعات من شروط القطع لتقليل وقت الإنتاج و تكلفة الإنتاج في آن واحد. أخيرًا تم استخدام إمكانات المحاكاة المتقدمة لبرنامج ANSYS لمقارنة التشوه الكلي الإجهاد المرن المكافئ، والإجهاد المكافئ (Von-Mises) لقطعة عمل مفترض انها مصنعة عن طريق التفريز بدون شق ومع وجود شق على سطحها. هدفت هذه التحليلات إلى توضيح تأثير سلامة السطح على عمر التعب للقطع المصنعة. وكشفت النتائج أن وجود شق أثر بشكل كبير على أداء قطعة العمل تحت ضغط.

الكلمات المفتاحية: التفريز ، سلامة السطح، شروط القطع، درجة حرارة القطع، خشونة السطح، الصلادة الدقيقة، شق، التعب الميكانيكي.